HOKKAIDO UNIVERSITY

Title	Changes in the ice sheet of the Wilkes subglacial basin and the high-latitude Southern Ocean during the Last Interglacial
Author(s)	飯塚, 睦
Degree Grantor	北海道大学
Degree Name	博士(環境科学)
Dissertation Number	甲第15594号
Issue Date	2023-09-25
DOI	https://doi.org/10.14943/doctoral.k15594
Doc URL	https://hdl.handle.net/2115/93933
Type	doctoral thesis
File Information	Mutsumi_Iizuka.pdf

Hokkaido University Collection of Scholarly and Academic Papers : HUSCAP

Changes in the ice sheet of the Wilkes subglacial basin and the high-latitude Southern Ocean during the Last Interglacial

最終間氷期におけるウィルクス海盆の氷床と南大洋高緯度の変動に関する研究

Mutsumi IIZUKA

Ph. D. Dissertation

Graduate School of Environmental Science

Hokkaido University

September 2023

Abstract

In recent decades, the Antarctic ice sheet has experienced rapid melting. This raises concerns about significant sea level rise in future warming scenarios, but projections regarding ice sheet shrinkage have remained uncertain. To improve the accuracy of predicting future sea level rise, it is crucial to understand the long-term behavior of the Antarctic ice sheet under warm climate conditions. Of particular importance is investigating areas where the bedrock lies below sea level, as ice sheets in such areas are vulnerable to ocean warming, such as the intrusion of relatively warm Circumpolar Deep Water (CDW) beneath marine-based ice shelves. This phenomenon can lead to an increase in grounded ice discharge, contributing to sea-level rise. Therefore, a better understanding of the sensitivity of the ice sheet in these regions in response to climate warming is crucial for accurately estimating the potential sea level rise in future warming scenarios.

The Last Interglacial period (LIG: 130,000–115,000 years ago), characterized by approximately 1ºC higher temperatures compared to the preindustrial level, provides valuable insights into the response of marine-based ice sheets under warm conditions. During the LIG, it is thought that sea levels were more than several meters higher than present levels, indicating a significant loss of polar Antarctic ice-sheet mass. However, due to the lack of detailed records of ocean and ice sheet variability during the LIG, the link between the two climate subcomponents has remained uncertain. In this study, I reconstructed detailed variability of the marine-based ice sheet in the Wilkes Subglacial Basin (WSB) of the East Antarctica and the high-latitude Southern Ocean (strength of the CDW inflow) in order to investigate their relationship.

In Chapter 1, the ice sheet variability during the LIG was investigated by analyzing multiple proxy records (neodymium isotope ratios, beryllium isotope ratios, grain size) in marine sediment cores (GC1407: 63.75°S, 130.52°E, 3687 m water depth) drilled in the continental rise offshore of the WSB, and by analyzing the oxygen isotope ratios in ice cores. The reconstruction of ice

sheet changes in the WSB at 300-year intervals revealed significant ice-sheet attrition during the early LIG period (129–126 ka) and the late LIG (122–120 ka). Particularly, the ice sheet attrition during the late LIG was suggested to be more extensive than during the early LIG. Combining these findings with previously reported sea level records suggest that the ice-sheet attrition from the WSB contributed to a sea level rise of ~0.8 meters.

Next, I attempted to reconstruct the strength of the CDW inflow that could potentially impact the marine-based ice sheet based on radiolarian assemblage analysis. Radiolarian assemblages strongly depend on the water mass property, such as sea temperature and salinity. By analyzing radiolarian fossils in marine sediment cores the strength of the CDW inflow can be reconstructed. However, the relationship between water masses and radiolarian assemblages in the high-latitude Southern Ocean has remained uncertain, hampering the application of the approach to the region. In Chapter 2, analyses of radiolarians in surface sediments and plankton net samples in the high-latitude Southern Ocean revealed distinct differences in assemblages among the water masses.

In Chapter 3, a new index (the radiolarian CDW index), which indicates the strength of southward CDW inflow was developed based on the radiolarian assemblages analyzed in Chapter 2, and then applied this index to the marine sediment core GC1407 to reconstruct the strength of CDW inflow at the GC1407 site during the LIG. The result indicates that CDW inflow was enhanced during both the early and late periods of the LIG. The enhanced CDW inflow coincided with the timing of the two episodic ice-sheet attritions during the LIG. These findings suggest that during the LIG, the enhanced CDW inflow contributed to the two episodic ice-sheet attritions, leading to sea level rise.

Chapter 1 | Reconstruction of ice-sheet behavior in the Wilkes Subglacial Basin during the Last Interglacial

Abstract 6

1. Introduction 7

2. Material and Method 10

3. Result and Discussion 18

Chapter 2 | Radiolarian assemblages related to each water mass in the high latitude of the Southern Ocean

Abstract 31

1. Introduction 32

2. Regional Setting 35

3. Material and Method 39

4. Result 42

5. Discussion 54

6. Conclusion 59

Chapter 3 | Developing an index for assessing circumpolar deep water strength and reconstructing circumpolar deep water inflow during the Last interglacial in the high-latitude Southern Ocean

Abstract 63

1. Introduction 64

2. Material and Method 66

3. Result and Discussion 70

4. Conclusion

Supplementary data for Chapter 1 77

Supplementary data for Chapter 2 103

Supplementary data for Chapter 3 111

Reference 114

Acknowledgement 128

Chapter 1

Reconstruction of ice-sheet behavior in the Wilkes Subglacial Basin during the Last Interglacial

Abstract

The Last Interglacial (LIG: 130,000–115,000 years ago) was a period of warmer global mean temperatures and higher and more variable sea levels than the Holocene (11,700–0 years ago). Therefore, a better understanding of Antarctic ice-sheet dynamics during this interval would provide valuable insights for projecting sea-level change in future warming scenarios. Here I present a high-resolution record constraining ice-sheet changes in the Wilkes Subglacial Basin (WSB) of East Antarctica during the LIG, based on analysis of sediment provenance and an ice melt proxy in a marine sediment core retrieved from the Wilkes Land margin. my sedimentary records, together with existing ice-core records, reveal dynamic fluctuations of the ice sheet in the WSB, with thinning, melting, and potentially retreat leading to ice loss during both early and late stages of the LIG. I suggest that such changes along the East Antarctic Ice Sheet margin may have contributed to fluctuating global sea levels during the LIG.

1. Introduction

Global mean sea levels during the Last Interglacial (LIG) are thought to have reached ~6–9 meters higher than present, with some records suggesting several peaks within that interval (Blanchon et al., 2009; Kopp et al., 2009; Thompson et al., 2011; O'Leary et al., 2013; Dutton et al., 2015a; Dutton et al., 2015b; Barlow et al., 2018; Polyak et al., 2018; Rohling et al., 2019). These elevated sea levels are attributed to a combination of ocean thermal expansion, melting of mountain glaciers, and mass loss from the Greenland and Antarctic ice sheets, with at least some contribution from Antarctica probably being required (Dutton et al., 2015a; McKay et al., 2011; NEEM community members, 2013; Shackleton et al., 2020). Furthermore, in order to explain the multiple sea-level peaks during the LIG, multiple events of ice-sheet mass loss must have occurred. However, detailed records of ice-sheet behavior during the LIG are lacking, limiting my ability to independently test the proposed global mean sea-level fluctuations or to resolve their geographic origin. The East Antarctic Ice Sheet stores freshwater with a sea-level equivalent of ~53 m, of which ~19 m resides in marine-based subglacial basins, including the Wilkes, Aurora, and Recovery basins (Fretwell et al., 2013). Because those marine-based sectors are considered to be vulnerable to ocean warming (DeConto et al., 2016), even small oceanographic changes in those regions could have contributed substantially to past fluctuations in global sea level. Whether ice in the marine-based subglacial basins of East Antarctica partially melted during the LIG is critical for understanding future sea-level changes (DeConto et al., 2014), but is not currently resolved by global sea-level records or by local sea-level fingerprints from this interval (Dutton et al., 2015a; Hay et al., 2014). For this reason, a focus on sedimentary records from the East Antarctic margin is needed.

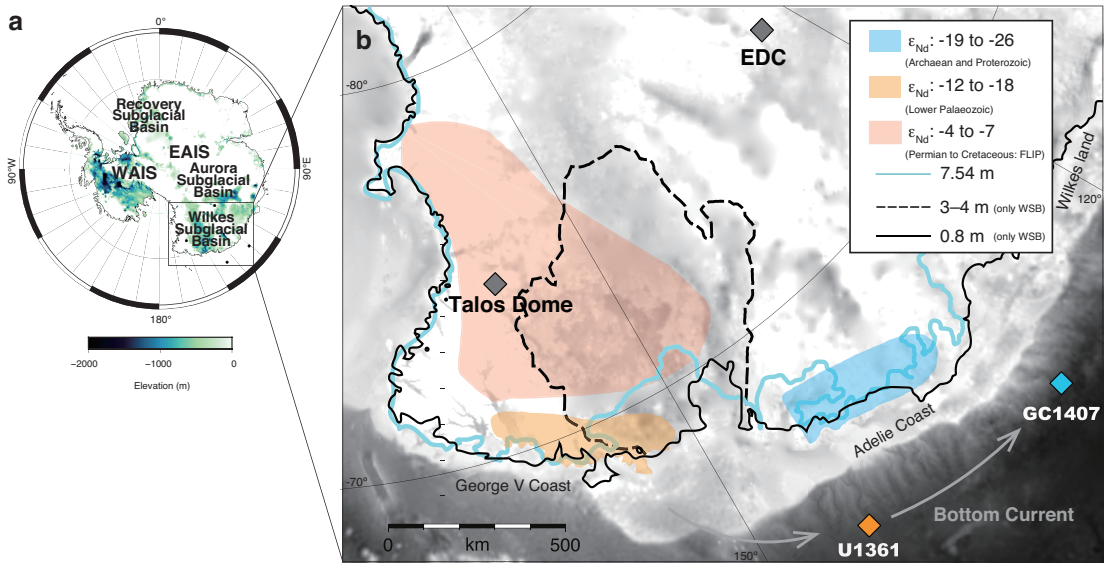


Figure 1 | Regional setting of the Wilkes Subglacial Basin. a, Map of Antarctica showing subglacial bedrock elevation below sea level (Frewell et al., 2013) and locations of marine sediment cores and ice cores relevant to this study. Areas in white are above modern sea level and shaded areas are below modern sea level. EAIS, East Antarctic Ice Sheet. WAIS, West Antarctic Ice Sheet. **b,** Detailed map of the Wilkes Subglacial Basin (WSB), with grey shading indicating bedrock elevation (as in panel a) and colored shading representing the simplified geographical extent of three geological terranes differentiated according to their neodymium isotope (ε_{Nd}) characteristics (map redrawn from Pierce et al. (2018)). Also shown are the locations of relevant marine sediment cores (GC1407 and U1361A) and ice cores (Talos Dome; EDC, EPICA Dome C). Lines illustrate positions of the ice-sheet margin in different ice-sheet model simulations and scenarios: black dashed line, fully retreated state of Mengel and Levermann et al. (2014); black solid line, simulated ice margin (8-km resolution and 300-year perturbation) in Sutter et al. (2020); light blue line, maximum simulated the Last Interglacial (LIG) retreat in DeConto and Pollard (2016). Sea-level contributions from the retreated states are given in the key. Grey arrow indicates modern flow direction of the bottom currents along the margin. Map created using the Quantarctica GIS package (Matsuoka et al., 2021) developed by the Norwegian Polar Institute and published under the Creative Commons Attribution 4.0 International License.

The ice sheet in the Wilkes Subglacial Basin (WSB) (Figure 1) has received particular attention because its complete loss would raise global sea levels by ~3–4 m (Fretwell et al., 2013; Mengel and Levermann, 2014). However, when and to what extent the ice-sheet margin in the WSB retreated during the LIG compared to its present position remains a matter of debate. A recent study using sediment provenance tracing in marine sediment core U1361A (64.40°S 143.88°E, 3465 m water depth, Figure 1b) suggested a significant retreat of the ice-sheet margin in the WSB during several late Pleistocene interglacials, including the LIG (Wilson et al., 2018). Subsequent studies have argued for a more limited retreat in the WSB during the LIG (Blackburn et al., 2020; Sutter et al., 2020; Golledge et al., 2021; Goursaud et al., 2020; Crotti et al., 2022), but also suggest a major ice-sheet collapse during Marine Isotope Stage 11 at ~400 thousand years ago (ka) (Blackburn et al., 2020). However, due to limitations in the chronologies and temporal resolution of existing records (Wilson et al., 2018; Blackburn et al., 2020), the timing and magnitude of ice-sheet change in the WSB during the LIG remain uncertain.

To better constrain the ice-sheet behaviour in the WSB during the LIG, I generated high-resolution records (300-year resolution) of detrital neodymium (Nd) isotopes and iceberg rafted debris (IBRD), supported by authigenic beryllium (Be) isotopes, in marine sediment core GC1407 (63.75°S, 130.52°E, 3687 m water depth, Figure 1b). This core was retrieved during a survey of the Antarctic Geological and Geophysical Research Project by the Japan National Oil Corporation in 1993. Neodymium isotope ratios are expressed as ε_{Nd} values, the deviation of $^{143}Nd/^{144}Nd$ ratios from the Chondritic Uniform Reservoir value in parts per 10,000, and provide evidence on the locus of subglacial erosion (Fretwell et al., 2013) (see Methods). Authigenic Be isotope ratios are reported as $^{10}Be/^{9}Be$ ratios and are considered to be an indicator of meltwater inputs (Valletta et al., 2018; Behrens et al., 2019; White et al., 2019) (see Methods). In addition, to evaluate the extent of ice-sheet margin retreat in the WSB, I estimated changes in elevation at Talos Dome

during the LIG based on the reported oxygen isotope ($\delta^{18}O$) records in Antarctic ice cores (Crotti et al., 2022). The chronologies for marine sediment cores GC1407 and U1361A are tuned to the Antarctic Ice Core Chronology 2012 (AICC2012) (Bazin et al., 2013; Veres et al., 2013), based on the onset and end of the LIG (see Methods).

2. Materials and Methods

Gravity core GC1407 was collected from the continental rise offshore of Wilkes Land (63.75ºS, 130.52ºE, 3687 m water depth) (Figure 1) during a survey of the Antarctic Geological and Geophysical Research Project (FY1993) by the Japan National Oil Corporation. The total length of core GC1407 is 5.35 m. Glacial-interglacial cycles are well resolved in the core, with glacial intervals indicated by silty-clay with occasional laminations, and interglacial intervals marked by siliceous silty-clay with high SiO_2 content.

2.1 Detrital neodymium isotope measurements

To measure detrital Nd isotopes in core GC1407, ~200 mg of the bulk fine-grained (< 63 μm) sediment fraction was first leached by sequential leaching methods (Bayon et al., 2002). The Fe-Mn oxide fraction was leached using 0.05 M hydroxylamine hydrochloride (HH) in 25% acetic acid (Ultrapure from Kanto Chemical Co., INC., Tokyo, Japan) in a water bath at 85ºC for four hours. Opal was then leached using 1M NaOH in a water bath at 80ºC for 30 min. After those procedures, the leached samples were rinsed in ultrapure water three times and dried in an oven (50ºC) for ~24 hours. Then, ~60 mg samples were completely digested with HNO_3-HF-$HClO_4$ at 130ºC for at least one day.

Chemical separation of Nd was carried out as follows: (i) major elements were removed from the sample solution using a cation exchange resin column (MCI GEL CK08P, Mitsubishi Chemical Corporation) with 1.8 M HCl; (ii) the REE fraction was extracted using 4.5 M HCl eluent; and (iii) the Nd fraction was isolated using a Ln-spec resin column (50–100 μm, Eichrom

Technologies) with 0.25 M HCl eluent. All reagents were trace metal grade reagents (TAMAPURE-AA-100 from Tama Chemicals, Ltd., Tokyo, Japan) and all procedures were conducted in a clean laboratory at the University of Toyama.

Samples were then dissolved in 0.16 M or 0.1 M HNO_3 and ultrasonicated for 1 hour prior to analysis using either a first generation (Nu Plasma) or second generation (Nu Plasma II) Nu Instruments HR MC-ICP-MS in the MAGIC laboratories at Imperial College London. The sample introduction system consisted of a Glass Expansion MicroMist 11ormalize (typical uptake rate ~100 μL/min) connected to a DSN-100 desolvation 11ormalize system. Measurements consisted of 50 cycles. All Nd isotope ratios were corrected for instrumental mass bias using the exponential law and a $^{146}Nd/^{144}Nd$ ratio of 0.7219. The reported $^{143}Nd/^{144}Nd$ ratios were corrected to a Jndi-1 $^{143}Nd/^{144}Nd$ ratio of 0.512115 (Tanaka et al., 2000) using bracketing standards. A correction for ^{144}Sm interference was applied, but all samples fell significantly below the threshold for accurate correction of ^{144}Sm on the ^{144}Nd signal (i.e. < 1000 ppm). The external reproducibility of sample data was estimated from the within-session standard deviation (2 s.d.) of the Jndi-1 standards, while its accuracy is demonstrated by repeat analyses of rock standard BCR-2, which yielded $^{143}Nd/^{144}Nd = 0.512641 \pm 0.000015$ (n=16), in excellent agreement with the literature value (Weis et al., 2006).

2.2 Sortable silt measurements

In preparation for grain-size analysis (McCave et al., 2006), carbonate and biogenic silica were removed from sediment samples by reacting with 1 M acetic acid for 24 h, followed by heating to 85ºC in 2 M sodium carbonate for 5 h, with samples being agitated several times during each step. Samples were then suspended in 0.2% sodium diphosphate decahydrate solution and placed on a rotating wheel before analysis using a laser diffraction-scattering particle size analyzer

(Horiba LA-920). Repeated analysis was performed on a subset of samples in an arbitrary order over several days and the mean standard deviation of replicate analyses was ± 0.1 μm.

2.3 Neodymium isotope records in core GC1407 as a provenance tracer

The detrital Nd isotope record in core GC1407 (< 63 μm fraction) shows large variations in ε_{Nd} values from −17 to −13 during the last glacial-interglacial cycle (Supplementary Figure 1b). In general, relatively low values were recorded during interglacial periods, with higher values during glacial periods. Fine-grained sediment (< 63 μm) at Antarctic continental rise sites such as GC1407 is predominantly composed of contourite and turbidite deposits (e.g., Wu et al., 2018). Therefore, the long-term glacial-interglacial trends in Nd isotopes probably reflect changes in the relative contribution of detrital sources among contourites and turbidites.

The contourites are supplied from the upstream region by the bottom water current. In core GC1407, the mean grain size of the sortable silt fraction (10–63 μm) ($\overline{SS}$), which is indicative of bottom water current intensity (McCave et al., 2006), shows large glacial-interglacial variations, with finer grain size during glacials and coarser grain size during interglacials (Supplementary Figure 1). This observation suggests that bottom current flow was intensified during the interglacial periods, which would have led to enhanced contourite supply from the upstream region. Furthermore, the absence of turbidite layers in core GC1407 during the LIG suggests that contourites were the predominant source throughout the LIG. Therefore, the fluctuations of detrital Nd isotope composition during the LIG should reflect changes in the sediment provenance upstream of the site.

2.4 Iceberg rafted debris (IBRD) measurements

Samples were processed for grain size analysis at Hokkaido University to provide evidence on the IBRD content. Dried samples were weighed and then wet-sieved to recover the coarse sand fraction (percent 250 μm–2 mm), which has previously been used to indicate IBRD in Antarctic

studies (Wilson et al., 2018). The 250 μm–2 mm fraction was weighed to obtain a weight percent of IBRD (percent 250 μm–2 mm) relative to the bulk sediment. For this study, I did not calculate IBRD mass accumulation rates, but they would scale almost directly with the weight percent IBRD (since my age model assumes constant sedimentation rates in the LIG and there are no large shifts or trends in dry bulk density in this interval).

2.5 *Cycladophora davisiana* relative abundance counts

Freeze-dried subsamples were weighed (approximately 1–2 g) and then treated with 15% H_2O_2 to remove the organic matter, followed by treatment with HCl solution to remove the calcium carbonate. The samples were then wet sieved (45 μm mesh size), after which two types of permanent slides were made from the residue to quantify the abundance (Q-slide) and for faunal analysis (F-slide) (Itaki et al., 2006). Briefly, to prepare the Q-slides, all residues were transferred to a 200 mL beaker containing 100 mL of distilled water. The solution was then well mixed, after which a 500 mL sample was taken from the suspension using a micropipette and dropped onto a glass slide. The sample was then dried and mounted with Norland optical adhesive. The F-slides were made from the remaining residues in the beaker and then mounted with Norland. On average, 100 individuals were counted on each slide, and the abundance of *C. davisiana* is reported in percent as the number per 100 individuals. Generally, a minimum sample of 100 individuals can effectively constrain the sampling error to be 10% or lower.

2.6 XRF core-scanning measurements

The SiO_2 content was analyzed by X-ray fluorescence (XRF) analysis of slab samples conducted at 1-cm intervals using the TATSCAN-F2 (Sakamoto et al., 2006) at Kochi University. Samples were wrapped in thin prolene film and scanned with a scanning diameter of 1 cm.

2.7 Authigenic beryllium isotope measurements

Samples for Be isotope analysis were prepared at the National Institute of Polar Research according to the chemical procedure established by Bourlès et al. (1989) and revised by Simon et al. (2016). Authigenic Be was extracted from 2 g dry samples by soaking them in 20 ml of leaching solution (0.04 M hydroxylamine hydrochloride and 25% acetic acid) at 95 ± 5ºC for 6 hrs. A 2 ml aliquot of the resulting leachate was sampled for measurement of the natural ^{9}Be concentration using inductively coupled plasma mass spectrometry (ICP-MS). The remaining solution was spiked with 300 µl of ^{9}Be carrier (9.833 × 10^{-4} g/g ^{9}Be) before Be purification by chromatography in order to determine accurate ^{10}Be concentrations using accelerator mass spectrometer (AMS) measurements of ^{10}Be/^{9}Be ratios at Micro Analysis Laboratory, Tandem accelerator, University of Tokyo (MALT) (Matsuzaki et al., 2004; Matsuzaki et al., 2015). Sample ^{10}Be concentrations were calculated from the ^{10}Be/^{9}Be ratios 14ormalized to the KN standard with a nominal ^{10}Be/^{9}Be ratio of 8.56 × 10^{-12} (Nishiizumi et al., 2007), and the reported authigenic ^{10}Be concentrations were decay-corrected using the ^{10}Be half-life of 1.387 ± 0.012 Ma (Chmeleff et al., 2010; Korschinek et al., 2010). Uncertainties on the authigenic ^{10}Be/^{9}Be ratios were calculated by propagating the uncertainties on the ICP-MS and AMS measurements.

2.8 Use of beryllium isotopes in core GC1407 as a meltwater proxy

Beryllium isotopes have been used as tracers in various fields of earth sciences, providing proxies for geomagnetic field strength (Simon et al., 2016), sea-ice extent, ice-shelf coverage (White et al., 2019; Yokoyama et al., 2016), and freshwater discharge from melting ice (Valletta et al., 2018; Simon et al., 2016). Cosmogenic ^{10}Be is produced in the upper atmosphere by the interaction of cosmic rays and is globally homogenized, with an atmospheric residence time of 1–2 years, before being deposited as meteoric ^{10}Be on the Earth surface (Willenbring and von Blanckenburg, 2010). Although cosmic rays also interact with surface rocks and produce *in-situ* ^{10}Be, the production rates for this process are orders of magnitude

lower than for meteoric ^{10}Be. In contrast, stable ^{9}Be occurs naturally as a trace component of crustal rocks and is transported by glacial erosion and weathering to the Antarctic coastal margin (White et al., 2019). Therefore, ^{10}Be/^{9}Be ratios can be applied in Antarctic margin sediments to constrain sedimentary processes and paleoenvironments, including freshwater supply during events of large-scale ice-sheet retreat. Since using the ^{10}Be/^{9}Be ratio corrects for variations related to particle size, retention behavior, and dilution, this ratio has been proposed as a more effective meltwater proxy than using ^{10}Be concentrations alone (Valletta et al., 2018; Behrens et al., 2019; White et al., 2019).

Authigenic ^{10}Be and ^{9}Be concentrations in core GC1407 show similar long-term changes, with higher values during interglacial periods (Holocene and LIG) and lower values during glacial periods (Marine Isotope Stages 2 and 6) (Supplementary Figure 2). Most notably, authigenic ^{10}Be concentrations during glacial periods decrease to ~10% of their value during interglacial periods, indicating a glacial-interglacial climate modulation of the records rather than a geomagnetic control (Valletta et al., 2018; Simon et al., 2016). Because the area of sea-ice cover changed significantly through glacial-interglacial cycles, the major decrease in ^{10}Be inputs during glacial periods likely reflects expanded and/or more permanent sea-ice coverage or the presence of ice shelves over the site. In contrast, variations in authigenic ^{10}Be inputs within interglacial periods cannot be attributed to sea-ice changes because the site of core GC1407 was not covered by sea ice (or ice shelves) during the LIG (Holloway et al., 2017). Hence, the ^{10}Be and ^{10}Be/^{9}Be variations in core GC1407 during the LIG likely reflect variations in the excess supply of ^{10}Be to this region via freshwater input from melting ice. Rapid scavenging by particles in the upper water column would transport the ^{10}Be to depth, enabling it to accumulate in the authigenic fraction of the marine sediments. Although other factors such as the scavenging of ^{10}Be by biogenic opal could potentially influence the deep-ocean sedimentary record of ^{10}Be, the SiO_2 content in core

GC1407 does not show significant fluctuations during the LIG (Supplementary Figure 3d), which suggests that any such effect is probably limited in core GC1407. Hence, similar to previous studies (e.g., Valletta et al., 2018; Simon et al., 2016), I use the authigenic $^{10}Be/^{9}Be$ record in core GC1407 as an indicator of regional freshwater inputs from melting ice.

2.9 Correlation between marine sediment cores

Benthic foraminiferal $\delta^{18}O$ records have been extensively applied to determine chronologies for marine sediment sequences, but benthic foraminifera is not continuously preserved in cores GC1407 or U1361A. Therefore, I have identified the interval of the LIG in cores GC1407 and U1361A based on records of *C. davisiana* and productivity that have previously been used to determine chronologies in the Southern Ocean (e.g., Brathauer et al., 2001; Wu et al., 2017).

First, I identified the interval of the LIG in core GC1407 based on the correlation of *C. davisiana* stratigraphy between cores GC1407 and RC11-120 (43.52ºS, 79.87ºE; 3135 m), since the chronology of RC11-120 has been well constrained using its planktonic foraminiferal (*Globigerina bulloides*) $\delta^{18}O$ record (Howard et al., 1992; Martinson et al., 1987) (Supplementary Figure 3, 4). RC11-120 was chosen because it is the marine sediment core closest to GC1407 where the variability of *C. davisiana* was recorded throughout the LIG. The relative abundance of *C. davisiana* fluctuates through glacial-interglacial cycles, with high contents during interglacials and low contents during glacials in most of the Southern Ocean (Brathauer et al., 2001; Hays et al., 1976). As shown in Supplementary Figure 3, temporal variations of *C. davisiana* in cores GC1407 and RC11-120 are similar over the last 140 kyr, which provides two tie points for core GC1407 near the start and end of the LIG (Supplementary Data).

Second, the LIG interval in core U1361A was constrained based on the correlation of the productivity records from cores U1361A (Wilson et al., 2018) and GC1407. In the Southern Ocean, the glacial-interglacial productivity pattern depends on latitude, with low and high

productivity during glacial and interglacial periods, respectively, in the high latitudes of the Indian sector of the Southern Ocean (Wu et al., 2017). Given the proximity of cores GC1407 and U1361A, their productivity patterns are expected to be similar through time. Indeed, the SiO_2 content in core GC1407 and Ba/Al ratios in core U1361A (proposed as a productivity proxy in the study area) (Wilson et al., 2018) show similar patterns on orbital to millennial timescales, including during the LIG interval (Supplementary Figure 3, 4). The chronology of core U1361A was therefore aligned with core GC1407 at two tie points based on their productivity records (Supplementary Figure 3, 4 and Supplementary Data).

2.10 Age control for marine sediment cores and ice cores

To compare the marine sediment core and ice core data, I transferred the Antarctic Ice Core Chronology 2012 (AICC2012) (Bazin et al., 2013; Veres et al., 2013) to the marine sediment core records. Recent studies have proposed that the correlation between sea surface temperature (SST) in the Southern Ocean and air temperature proxies (δD or $\delta^{18}O$) in the Antarctic ice cores can be used to tune the age scales of marine sediment cores, including during the LIG when there is a strong similarity between the marine and ice core records (Crosta et al., 2020; Hayes et al., 2014). However, SST records are not available for cores GC1407 or U1361A. Therefore, the planktonic foraminiferal $\delta^{18}O$ record in core RC11-120, which is taken as an indicator of SST, and the δD record from the Dome Fuji ice core (Uemura et al., 2012) were compared in order to transfer the age of core RC11-120 onto the AICC2012 age scale, using three tie points (Supplementary Figure 4, Supplementary Data). The Dome Fuji core was chosen because it is the Antarctic ice core site closest to RC11-120. The uncertainty of AICC2012 is ±2.6 ka on average during the past 100–720 kyr (Bazin et al., 2013).

Then, this chronology was transferred to core GC1407 based on the correlation of the *C. davisiana* records between cores RC11-120 and GC1407, as described above. Finally, this

chronology was transferred to core U1361A based on the correlation between the productivity records from cores GC1407 and U1361A, as also described above. With these age models, the 2.8–3.8 m depth interval in core GC1407 and the 1.4–2.1 m depth interval in core U1361A correspond approximately to the LIG (Supplementary Figure 3). The robustness of the chronology for core GC1407 is also supported by the last appearance of the diatom *Hemidiscus karstenii*, which is identified at 4 m depth in this core and is known to occur within late Marine Isotope Stage 6 (Crosta et al., 2020). Note that these age models imply significantly higher sedimentation rates during the LIG than during the glacial intervals (around 3.5 to 5 times higher) (Supplementary Figure 5), and that the age model for core U1361A is significantly different during the LIG from the original published version (which had limited constraints and assumed linear sedimentation rates throughout the late Pleistocene).

3. Results and Discussion

3.1 Two episodes of provenance change during the LIG

Detrital sediment Nd isotopes have been widely applied as an indicator of sediment provenance around Antarctica (Wilson et al., 2018; Cook et al., 2013; Roy et al., 2007; Pierce et al., 2018). The detrital record of fine-grained sediment (< 63 μm) in core GC1407 shows relatively low ε_{Nd} values (around −16 to −15) during the Holocene and relatively higher values with more variability (−17 to −13) during the LIG (Figure 2d, i). Two episodic increases in ε_{Nd} values (reaching −14 to −13) are recognized within the LIG (129–126 ka and 122–118 ka) (Figure 2i), suggesting dynamic changes in sediment provenance. Interestingly, the updated age model for core U1361A also reveals some evidence for two Nd isotope peaks during the LIG in core U1361A, although they are defined by only a small number of data points (Figure 2i). Given the good agreement in the timing of the two peaks between the two cores, my high-resolution record from core GC1407 appears to reinforce the presence of two peaks in core U1361A. Although there is a clear offset

of ~4 ε_{Nd} units between the two records (Figure 2d, i), the similarity in terms of the magnitude of changes and temporal patterns suggests that the two events of increasing ε_{Nd} values during the LIG likely reflect the same phenomenon of provenance change.

Sediment provenance variations indicated by the Nd isotope record in core U1361A are thought to reflect the waxing and waning of the ice-sheet margin in the WSB (Wilson et al., 2018).This interpretation is based upon the ultimate source of detrital sediment input to marine sequences on the Antarctic margin being from the erosion of proximal and/or upstream coastal bedrock (Licht et al., 2017), which can be expected to change with advance or retreat of the ice-sheet margin. Furthermore, the ε_{Nd} values of the bedrock vary by region (Wilson et al., 2018; Cook et al., 2013; Roy et al., 2007; Pierce et al., 2017) (Figure 1b). The coastal bedrock in the vicinity of core GC1407 (Adelie Coast; around 145–135ºE) has ε_{Nd} values of −19 to −26 (Archaean and Proterozoic age), while coastal bedrock proximal to core U1361A (George V Coast; around 150–160ºE) has ε_{Nd} values of −12 to −18 (Lower Palaeozoic age) (Pierce et al., 2017). In contrast, ε_{Nd} values in the WSB, inland of George V Coast, are inferred to be more radiogenic (−4 to −7), reflecting the Permian-Cretaceous rocks of the Ferrar Large Igneous Province (FLIP) and associated Beacon Supergroup (Pierce et al., 2017; Ferraccioli et al., 2009). At present, detrital sediments are dominantly transported from the coastal margin of the WSB to the location of core U1361A (Wilson et al., 2018). Since the LIG was also an interglacial climate state, it can be assumed that the sediment transport regime during the LIG was broadly similar to the modern day. Therefore, the high ε_{Nd} values in core U1361A during the LIG (Figure 2i) are interpreted to reflect the supply of detritus from inland bedrock to the continental rise due to WSB ice-sheet retreat (Wilson et al., 2018).

Since sediments are transported westwards by bottom currents (Antarctic Bottom Water) (Presti et al., 2011; Jimenez-Espejo et al., 2020) near Wilkes Land, the detrital Nd isotope record

in core GC1407 likely reflects the erosion of coastal bedrock upstream of the site (i.e., Adelie Coast and George V Coast) (Figure 1b), especially during interglacials when the bottom current intensified (Presti et al., 2011; Jimenez-Espejo et al., 2020) (see Methods). If retreat of the ice-sheet margin in the WSB enhanced the supply of sediments from inland FLIP sources, relatively high detrital ε_{Nd} values would also be expected in core GC1407, whereas the supply of detritus from the Adelie Coast would result in a lowering of ε_{Nd} values. As such, I suggest that the relatively low ε_{Nd} values in core GC1407 compared to core U1361A (~4 ε_{Nd} units offset) probably indicate continuous detrital input from the Adelie Coast through the Holocene and LIG (Figure 2d, i). On the other hand, I suggest that the two Nd isotope peaks observed in core GC1407 during the LIG, coincident with peaks in core U1361A, reflect ice-sheet margin retreat events in the WSB. Overall, my new high-resolution record, together with improved constraints on the chronology of core U1361A, reveals that ice-sheet margin retreat in the WSB occurred during both the early and late LIG. Although my record does not rule out the possibility of ice-sheet margin retreat in the Adelie Coast region, several independent ice-sheet modelling studies suggest that ice-sheet margin retreat in this region would have been limited during the LIG (DeConto and Pollard, 2016; Sutter et al., 2020) (Figure 1b), which is also consistent with observations over recent decades from the Adelie Coast (Rignot et al., 2019).

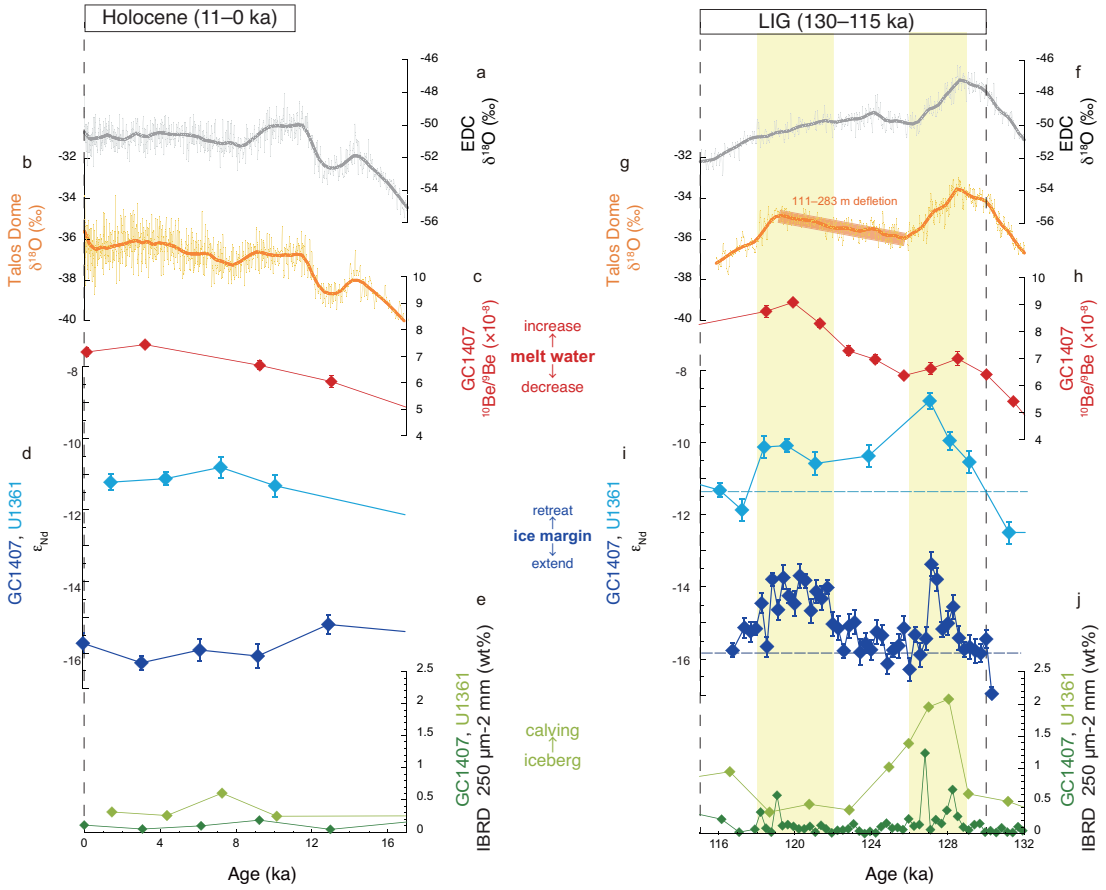


Figure 2 | Multi-proxy evidence for variability in the Wilkes Subglacial Basin during the Holocene and Last Interglacial. a–e, and **f–j,** Multi-proxy data for the Holocene and Last Interglacial (LIG), respectively. **a, f,** $\delta^{18}O$ records from EPICA Dome C (EDC) ice core (thin and bold black lines are the raw signals and weighted smoothing, respectively) (Masson-Delmotte et al., 2011). **b, g,** $\delta^{18}O$ records from Talos Dome ice core (thin and bold orange lines are the raw signals and weighted smoothing, respectively) (Masson-Delmotte et al., 2011). **c, h,** Authigenic $^{10}Be/^{9}Be$ ratios from core GC1407 (red squares, this study) (error bars are 1 s.d.). **d, i,** Detrital sediment Nd isotopes (ε_{Nd}) from core GC1407 (dark blue diamonds, this study) and core U1361A (light blue diamonds) (Wilson et al., 2018) (error bars are 2 s.d.). **e, j,** Iceberg rafted debris (IBRD, percent 250 µm–2 mm) from core GC1407 (dark green circles, this study) and core U1361A (light green circles) (Wilson et al., 2018). Yellow bars indicate two episodes of inferred the Wilkes Subglacial Basin ice mass loss during the early and late LIG.

3.2 Extent of ice-sheet melting in the WSB

To provide further evidence on the nature and magnitude of ice-sheet margin changes in the WSB that are implied by the two peaks in the detrital Nd isotope record, I measured authigenic Be isotopes in core GC1407. Changes in the $^{10}Be/^{9}Be$ ratio in marine sediments proximal to ice-sheet margins can be used to infer regional inputs from ice melt (Valletta et al., 2018; Behrens et al., 2019; White et al., 2019). The production of ^{10}Be in the atmosphere is followed by its deposition onto the ocean and ice sheets, such that the melting of ice sheets and icebergs releases the accumulated ^{10}Be into the ocean, where it is scavenged by particles and accumulates in the authigenic fraction of marine sediments (Valletta et al., 2018). In contrast, ^{9}Be is the stable naturally-occurring isotope found in bedrock and supplied via erosion and weathering. An increase in the $^{10}Be/^{9}Be$ ratio in marine sediments can therefore be interpreted as indicating a significant ice melting event (Valletta et al., 2018) (see Methods).

The $^{10}Be/^{9}Be$ record in core GC1407 provides strong support for ice mass loss from the WSB during the LIG. The $^{10}Be/^{9}Be$ ratios vary from 6.0×10^{-9} to 9.1×10^{-9} during the LIG, with a two-stepped increase leading to maximum values at ~120 ka (Figure 2h). This finding points to an increase in ice melting during the late LIG, and suggests that melting was more pronounced from 122–118 ka than from 129–126 ka. The two-stepped increase in $^{10}Be/^{9}Be$ ratios also coincides with the Nd isotope peaks (Figure 2h, i), supporting the interpretation of those provenance shifts as reflecting ice-sheet retreat rather than reflecting changes in other processes such as deep-current sediment transport.

The content of iceberg rafted debris (IBRD; weight percent of grains of 250 μm–2 mm diameter), which provides a qualitative indicator of iceberg discharge (Wilson et al., 2018), was also measured in core GC1407 to infer the causes of ice mass loss from the WSB. Peaks in IBRD in cores GC1407 and U1361 are observed during the early LIG and coincide in timing (Figure

2j), which suggests that iceberg calving was an important process for ice mass loss during the early LIG. On the other hand, the $^{10}Be/^{9}Be$ record reaches its maximum during the late LIG, indicating that ice-shelf basal melting (Valletta et al., 2018) may have played a relatively more important role than calving in ice mass loss from the WSB during the late LIG.

3.3 Assessment of ice mass loss in the WSB

To further evaluate the ice-sheet retreat in the WSB during the late LIG as indicated by my sedimentary records, I made a comparison to the $\delta^{18}O$ records from the Talos Dome and EPICA Dome C (EDC) ice cores (Masson-Delmotte et al., 2011). Differences in the $\delta^{18}O$ records between the Talos Dome and EDC ice cores have been proposed to provide an indicator for the advance and retreat of the ice-sheet margin in the WSB (Sutter et al., 2020; Crotti et al., 2022). Because the Talos Dome site is located in the headlands of the WSB outflow region, it is sensitive to changes of the ice-sheet margin in the WSB (Sutter et al., 2020; Crotti et al., 2022), unlike inland plateau sites such as EDC (Figure 1b). Therefore, the $\delta^{18}O$ record from the Talos Dome ice core has been used to estimate temperature increases that were associated with ice-sheet elevation drops, which can be linked to regional ice-sheet mass loss (Sutter et al., 2020; Goursaud et al., 2020; Crotti et al., 2022; Fogwill et al., 2017; Weber et al., 2021; Sutter et al., 2019).

During the early LIG (130–126 ka), the $\delta^{18}O$ records at the Talos Dome and EDC sites vary in parallel (Figure 2f and g). In contrast, the $\delta^{18}O$ record at the Talos Dome increases by 1.5‰ from 126 ka to 118 ka, whereas the EDC record shows the opposite trend with a decrease during this period (Figure 2f and g) (Masson-Delmotte et al., 2011). The increase in the v record at Talos Dome compared to that of EDC is interpreted as a site temperature increase caused by a decrease in site elevation (Crotti et al., 2022). Notably, the 1.5‰ increase in $\delta^{18}O$ values at Talos Dome during the late LIG coincides with the increases in ε_{Nd} values and $^{10}Be/^{9}Be$ ratios in cores GC1407 and U1361 (Figure 2). This temporal agreement allows us to link ice thinning at the Talos Dome

site to ice-sheet margin retreat and melting in the WSB, as inferred from the offshore records. The timing of these changes in the ice core record further supports the hypothesis that ice-sheet retreat and melting may have been more pronounced during the late LIG (122–118 ka) than during the early LIG (129–126 ka).

Following Crotti et al. (2022), I estimate the change in elevation at Talos Dome during the LIG by applying three different $\delta^{18}O$ -elevation relationships derived from climate simulations and observations (−0.53‰/100 m, –0.93‰/100 m, and −1.35‰/100 m) (Goursaud et al., 2020; Crotti et al., 2022; Frezzotti et al., 2004; Werner et al., 2018). Based on those three different relationships, the 1.5‰ increase in $\delta^{18}O$ values at Talos Dome is equivalent to a drop in local ice-sheet surface elevation of 111–283 m. Although their study focused on the early LIG, Sutter et al. (2020) presented a model in which the elevation drop of 100–200 m at Talos Dome could be related to an inland retreat of the ice margin in the WSB by several hundred km (their experiment with 8-km resolution, 300-year perturbation) (Sutter et al., 2020) (black line in Figure 1b). Another recent model presented by Crotti et al. (2022) also indicates ice margin retreat in the WSB of ~100 km during the 133–115 ka interval, and notably the greatest retreat occurred towards the end of the LIG, which is consistent with my interpretations. In summary, the above findings provide multiple lines of evidence from which I infer ice mass loss from the WSB during the late LIG from 122–118 ka.

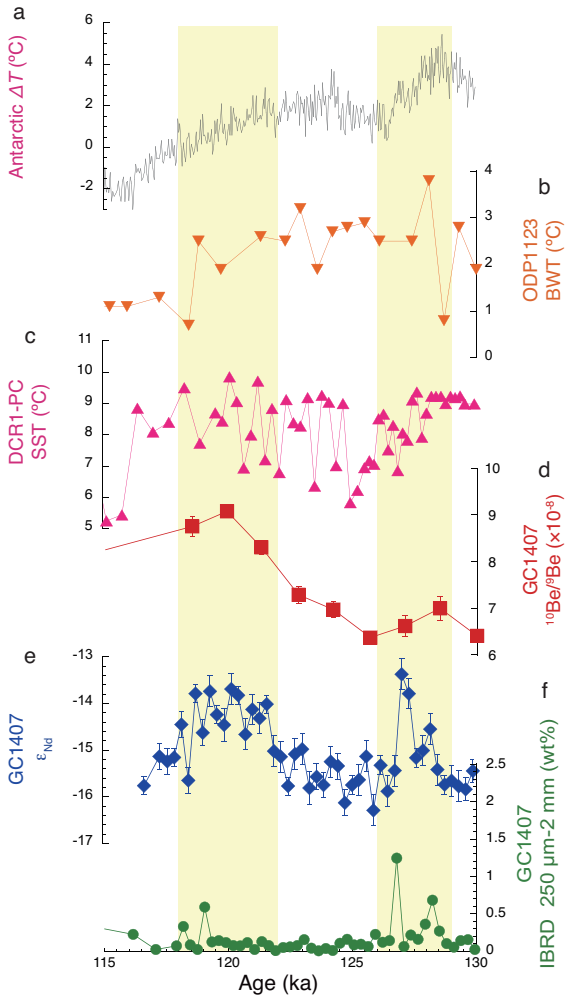


Figure 3 | Comparison of core GC1407 records to regional palaeoclimate records. a, Antarctic ice-core temperature difference (ΔT, difference from mean values of the last millennium) derived from deuterium isotopes at EPICA Dome C (EDC) (Masson-Delmotte et al., 2011) plotted on the AICC2012 age scale (grey line). **b**, Southern Ocean bottom water temperature (BWT) from benthic foraminiferal Mg/Ca ratios at Ocean Drilling Program (ODP) Site 1123 (orange triangles) (Elderfield et al., 2010). **c**, Southern Ocean sea surface temperature (SST) from diatom assemblages in core DCR1-PC (pink triangles) (Crosta et al., 2020). **d**, Authigenic $^{10}Be/^{9}Be$ ratios from core GC1407 (red squares, this study) (error bars are 1 s.d.). **e**, Detrital sediment Nd isotopes (ε_{Nd}) from core GC1407 (dark blue diamonds, this study) (error bars are 2 s.d.). **f**, Iceberg rafted debris (IBRD, percent 250 µm–2 mm) from core GC1407 (green circles, this study). Yellow bars indicate two episodes of inferred the Wilkes Subglacial Basin ice mass loss during the early and late last interglacial.

3.4 Drivers of ice mass loss in the WSB

Previous studies of Antarctic ice-sheet variations during the LIG have focused on the early LIG (~128 ka) when air temperature rise in Antarctica reached its peak (Sutter et al., 2020; Goursaud et al., 2021). However, my records reveal evidence for extensive ice mass loss from the WSB during the late LIG (~120 ka), when air temperatures were comparable to the present (Figure 3a). Hence, atmospheric forcing was unlikely to have been a trigger for ice mass loss during the late LIG. Instead, since the ice sheet in the WSB is marine-based (Fretwell et al., 2013), ocean forcing from changes in ocean circulation and/or ocean warming may have played critical roles in the ice-sheet mass loss during the late LIG.

In general, the LIG was characterized by sea surface temperatures (SST) in the Southern Ocean that were approximately 2ºC warmer than the pre-industrial Holocene (Capron et al., 2014) and by a southward-shifted Polar Front in the Indian Ocean (Chadwick et al., 2022). Both these conditions could have contributed to enhanced ocean forcing of ice-sheet mass loss, with the frontal shifts potentially helping to drive incursions of relatively warm Circumpolar Deep Water onto the continental shelves, which could lead to inland migration of grounding lines (Pritchard et al., 2012; Fogwill et al., 2014). Notably, deep-ocean temperatures in the Southern Ocean also remained at elevated values from the early to the late LIG (Elderfield et al., 2010) (Figure 3b), pointing to warmer than present conditions in the sub-surface Southern Ocean even during the late LIG. Furthermore, while the spatial coverage is sparse, two marked warming peaks can be resolved in some SST reconstructions from the Southern Ocean, with one during the early LIG and another during the late LIG (Crosta et al., 2020) (Figure 3c). Although the above records are from lower latitudes of the Southern Ocean than the Antarctic margin, recent diatom-based SST reconstructions from close to the margin also indicate warmer conditions throughout the LIG than today (Chadwick et al., 2012). Overall, these records are consistent with ocean forcing as the

primary driver of ice loss from the ice sheet in the WSB during the LIG, although the exact mechanisms responsible for the ocean warming remain to be fully explored.

3.5 Contribution of ice loss from the WSB to global sea-level rise

My data provide a unique opportunity to compare a well-resolved ice-proximal record of changes in the East Antarctic Ice Sheet to global sea-level records for this interglacial period (Figure 4) (Blanchon et al., 2009; Kopp et al., 2009; Thompson et al., 2011; O'Leary et al., 2013; Dutton et al., 2015a; Dutton et al., 2015b; Barlow et al., 2018; Polyak et al., 2018; Rohling et al., 2019). Sea-level variability during the LIG remains uncertain, but three broad scenarios have been proposed: (1) a high-stand during the early LIG (Polyak et al., 2018; Rohling et al., 2019); (2) a high-stand for the initial several thousand years followed by a secondary rise around 120 ka (Blanchon et al., 2009; Dutton et al., 2015b); and (3) bimodal sea-level peaks during the early and late LIG (Kopp et al., 2009; Thompson et al., 2011; O'Leary et al., 2013) (Figure 4 a–c). Recent studies have suggested that parts of the West Antarctic Ice Sheet were lost during the early LIG and could have made the main contribution to global sea-level rise at that time (Golledge et al., 2021; Turney et al., 2020). However, the causes of a possible sea-level rise during the late LIG for scenarios 2 and 3 remain unknown. My study provides evidence for ice mass loss from the WSB during the late LIG, thereby supporting an Antarctic origin for global sea-level rise at this time, which would be consistent with sea-level rise scenarios 2 and 3. Taken together with previous studies (NEEM community members, 2013; Turney et al., 2020), I suggest that ice sheets in different regions of Antarctica lost ice mass in a step-wise pattern during the LIG, which may have contributed to dynamic fluctuations of global sea level in any of the scenarios 1–3 during the LIG.

Ice-sheet model experiments (Sutter et al., 2020; Crotti et al., 2022) indicate that a 100–200 m drop in elevation at Talos Dome due to WSB ice-sheet margin retreat would translate to a sea-

level rise of ~0.4–0.8 m. Combining those model results with my study, I suggest that ice sheet mass loss in the WSB probably contributed to a similar magnitude of sea-level rise during the late LIG. Hence, such a change could only explain a small portion of the global sea-level rise of ~6–9 m estimated for the LIG (Dutton et al., 2015a). If the global sea-level rise was closer to the maximum estimates (~9 m) (Dutton et al., 2015a), then significant ice mass loss from other sectors of East Antarctica would still be required, after accounting for contributions from mass loss of the marine-based West Antarctic Ice Sheet (~3.3 m) and a portion of the Greenland Ice Sheet (likely up to ~2 m) (NEEM community members, 2013; Bamber et al., 2009; Colville et al., 2011; Ross et al., 2012). Within East Antarctica, the ice sheets in the Aurora and Recovery Subglacial Basins (Figure 1a) are also thought to be vulnerable to ocean warming (Golledge et al., 2017; Sun et al., 2020), and represent likely candidates for additional global sea-level rise during the LIG. Comparable high-resolution records from the different sectors of the East Antarctic Ice Sheet will therefore be required to better constrain the ice-sheet dynamics and the origin of sea-level variability during the LIG.

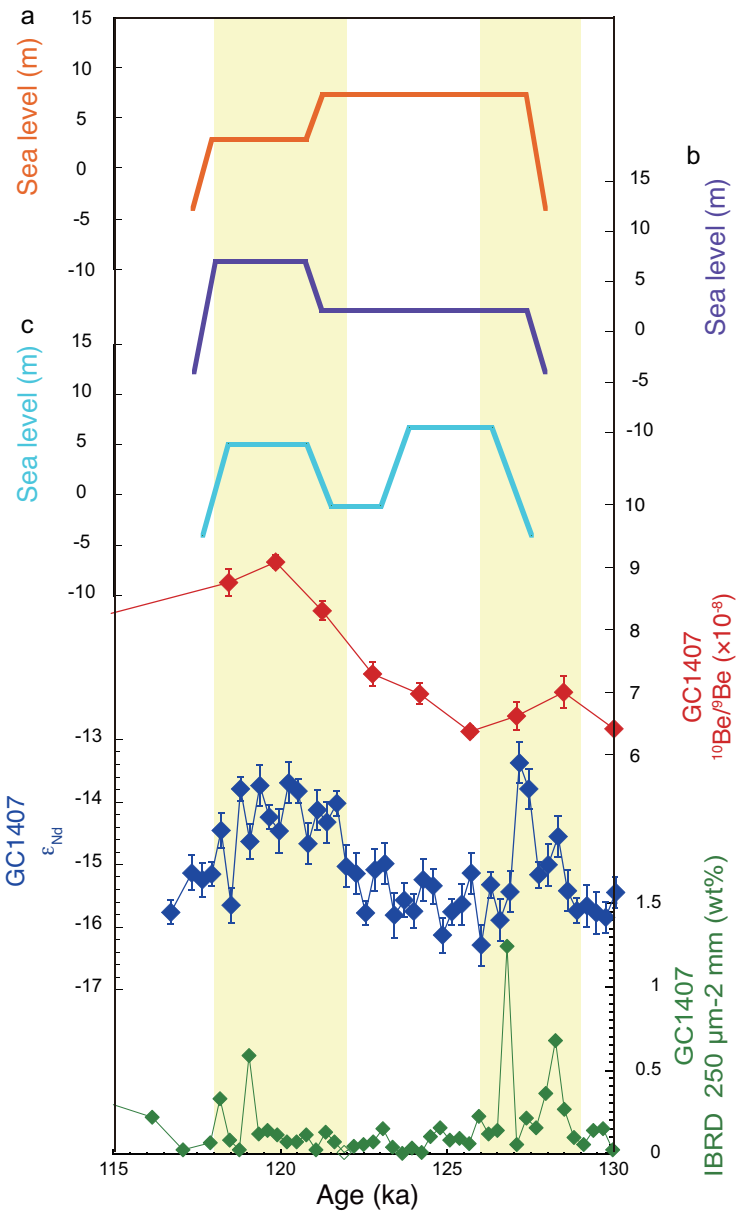


Figure 4 | Comparison of core GC1407 records to sea-level scenarios during the Last Interglacial. a–c, Simplified eustatic sea-level records from a range of global sites (Blanchon et al., 2009; Kopp et al., 2009; Thompson et al., 2011; O'Leary et al., 2013; Dutton et al., 2015b; Barlow et al., 2018; Polyak et al., 2018; Rohling et al., 2019). d, Authigenic $^{10}Be/^{9}Be$ ratios from core GC1407 (red squares, this study) (error bars are 1 s.d.). e, Detrital sediment Nd isotopes (ε_{Nd}) from core GC1407 (dark blue diamonds, this study) (error bars are 2 s.d.). f, Iceberg rafted debris (IBRD, percent 250 µm–2 mm) from GC1407 (green circles, this study). Yellow bars indicate two episodes of inferred the Wilkes Subglacial Basin ice mass loss during the early and late last interglacial.

Chapter 2

Radiolarian assemblages related to each water mass in the high latitude of the Southern Ocean

Abstract

It is believed that the Southern Ocean plays a central role in redistributing the physical and biogeochemical properties around the globe and significantly influences the global climate. Tracing the water masses in the Southern Ocean is vital to better understand the global climate system. Understanding the long-term changes in the water masses of the Southern Ocean in the geological past is essential to evaluate the role of the Southern Ocean in the climate system. Radiolarian fossils are a useful tool to reconstruct the water masses of the Southern Ocean. However, the radiolarian assemblages in the high latitudes of the Southern Ocean (south of the polar front (PF)) still remain unclear. This study reported the radiolarian assemblages in surface marine sediment and plankton tow samples collected from the high latitudes of the Southern Ocean (south of the PF). The four factors (termed F1–F4) of radiolarian assemblages in surface sediments were identified through the Q-mode factor analysis. F3 and F4 were identified as the radiolarian assemblages associated with water masses. F1 was suggested to be related to surface waters south of the southern boundary (SB) of the Antarctic Circumpolar Current (ACC) that is cooled by melting sea ice and ice sheets. F3 was associated with the modified circumpolar deep water (mCDW). F2 was associated with water masses north of the SB, and a comparison with the vertical distribution of radiolarian assemblages from plankton net samples identified radiolarian assemblages associated with the circumpolar deep water (CDW) and surface waters north of the SB. The radiolarian assemblage of F4 was not related to any water mass, but it was suggested that they dwell in ice shelf and/or sea ice edge environments. It is expected that these specific radiolarian assemblages associated with water masses and ice edge environments can be used to reconstruct the ocean environment south of the PF in the geologic past.

1. Introduction

The interaction between the Southern Ocean and the Antarctic ice sheet plays a crucial role in the global climate system. Recently, it has been revealed that the increase in warm seawater intrusion under the ice shelf causes a significant melting of the Antarctic ice sheet (Rignot et al., 2013), potentially leading to a significant global sea-level rise in the future (DeConto and Pollard, 2016). On the other hand, the melting of the ice sheet and sea ice triggered the reduction of the Antarctic bottom water (AABW), which is an important component of the global climate system (e.g., Hayes et al., 2014). Understanding the hydrographic dynamics through the interaction between the Southern Ocean and the Antarctic ice sheet provides insight into the global climate system. Furthermore, investigating the temporal change in the Antarctic ice sheet responses to the oceanic forcing is necessary to understand the long-term interactions between the Southern Ocean and the Antarctic ice sheet.

Foraminifera fossils in marine sediments have been used to reconstruct the past change in the volume of water masses distributed in the Southern Ocean (e.g., Hayes et al., 2014). Although calcareous microfossils, such as foraminifers, and their geochemical analyses are powerful tools for palaeoceanographic studies, their application is limited in the Southern Ocean due to the wide distribution of carbonate-free sediments south of the polar front (PF). On the other hand, it is well known that siliceous microfossils, such as radiolarians and diatoms, in the sediments are common south of the PF (Dutkiewicz et al., 2015). Polycystine radiolarians (hereafter, radiolarians) are one group of planktonic microorganisms (Protista) that are distributed in the world oceans, and their siliceous skeletons are preserved in deep-sea sediments as microfossils. Because radiolarian assemblages and their geographical and vertical distributions are closely related to the oceanic environments (e.g., Cortese and Abelmann, 2002; Abelmann and Gowing, 1997; Matsuzaki et al., 2016), it has been widely used as a palaeoceanographic proxy.

To apply this method to the high latitudes, information on the radiolarian assemblages related to hydrography in this area is needed. However, most previous studies focusing on radiolarian assemblages have been conducted north of the Southern Boundary (SB) of the Antarctic Circumpolar Current (ACC) (Lawer et al., 2021; Abelmann et al., 1999; Abelmann and Gowing; 1997; Morley and Stepien, 1985), and radiolarian assemblages south of the SB are limited. Although radiolarian assemblage datasets have been reported in the East Antarctic sector (Nishimura et al., 1997; Nishimura and Nakaseko, 2011), they are not sufficient to examine their relation to water masses.

This study aims to (1) provide information on the radiolarian assemblages from the continental shelf to the abyssal plain south of the PF and (2) clarify their relation to water masses. This study especially focuses on the water mass around the East Antarctic coastal areas, where radiolarian data is scarce.

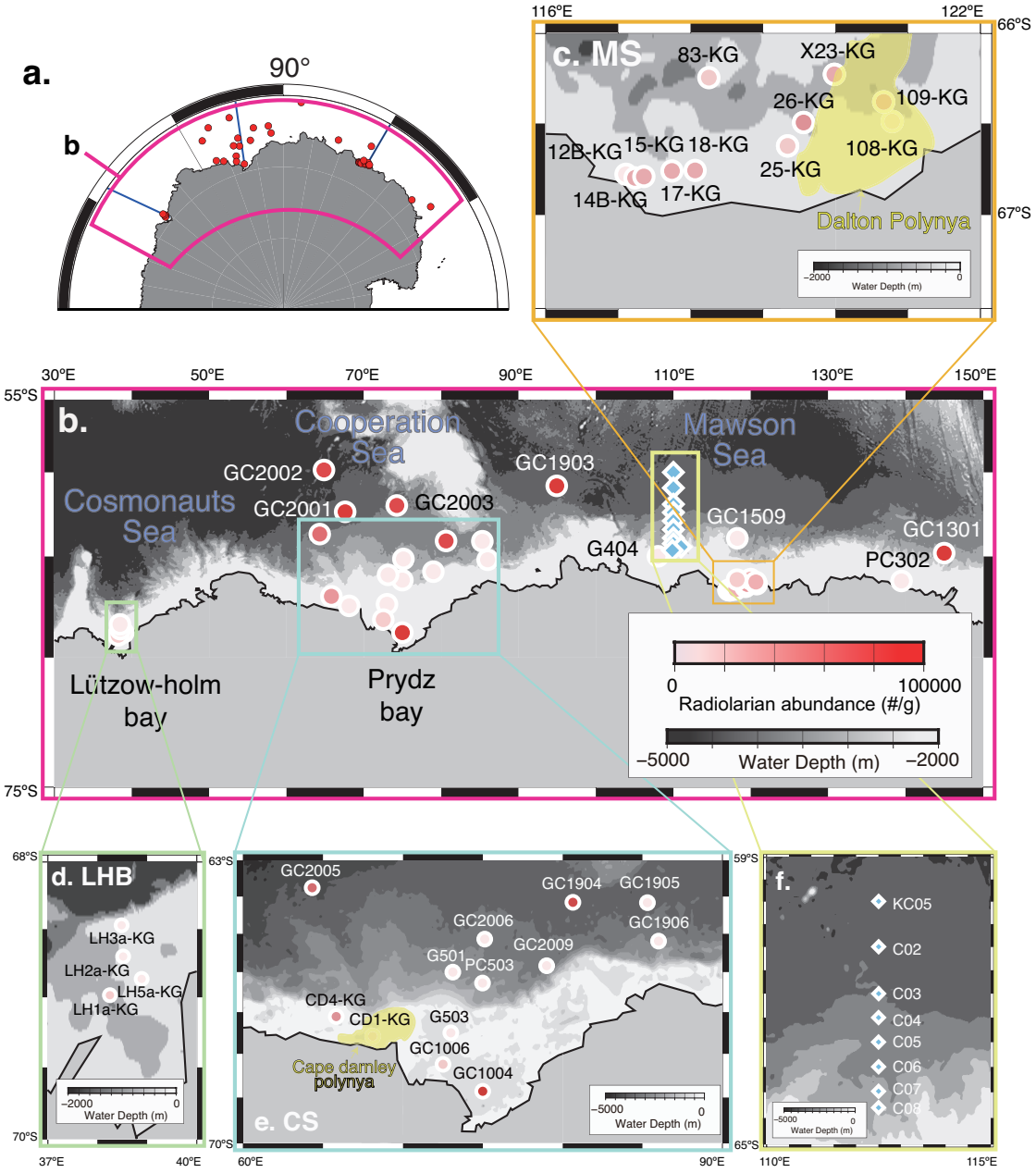


Figure 1 | Map of the Southern Ocean showing the sample location. a, Map of Antarctica, red dots are samples location used in this study. The blue line is the vertical section used in Figure 2. **b,** Distribution of radiolarian abundance in surface sediment samples, light blue diamonds are plankton tow sample location. **c, d, e,** Close-up of the map in Figure 1c in the Sabrina Coast (SC), Lützow-Holm Bay (LHB), and Cooperation Sea (CS), respectively. **f,** Close-up of the map in the plankton tow sample location. Five maps (b, c, d, e, f) showing previously published data overlain on the BEDMAP 2 subglacial topography (Fretwell et al., 2013).

2. Regional setting

2.1 Geographic setting

The study area covers the continental shelf to the abyssal plain in East Antarctica south of the PF (water depth ranging from 219 to 4642 m) (Figure 1, Table 1). In the surface sediment sampling coverage of this study, the study area is divided into three subareas, i.e., the Cosmonauts Sea, the Cooperation Sea, and the Mawson Sea (Figure 1b).

The Cosmonauts Sea which is located 30–50°E in the Southern Ocean (Figure 1b) has Lützow-Holm Bay (LHB). This bay is characterized by a deep glacial trough in the center that is ~15 km wide and more than 600 m deep and deepens southward to ~1200–1400 m (Hirano et al., 2020). The Cooperation Sea that is located east of the Cosmonauts Sea has Prydz Bay (PB), which is a large embayment, with an area of around 80,000 km^2. The continental shelf in the PB slopes landward, with water depths ranging from ~200 to 400 m at the continental shelf break to ~600 to 1000 m at the inner shelf (Fretwell et al., 2013). The Mawson Sea is located east of the Cooperation Sea, and the continental shelf in this area (Sabrina Coast (SC)) is generally more than 120 km wide (Close et al., 2007). The topography in the SC is typical, similar to that of PB and LHB, with the seabed deepening landwards from the outer shelf at depths ranging from 200 to 500 m to the inner shelf at depths exceeding 1400 m in this study area of SC (116–122°E).

Table 1 | Locations, water depth, and Lithology of surface sediments

Station		Longitude (ºE)	Latitude (ºS)	Water depth (m)	Location	Lithology
JARE 61	St. 12B-KG	117.11	66.78	419	continental shelf	Silty clay
JARE 61	St. 14B-KG	117.23	66.8	987	continental shelf (submarine basin)	Silty clay
JARE 61	St. 15-KG	117.36	66.79	691	continental shelf	Silty clay
JARE 61	St. 17-KG	117.74	66.76	608	continental shelf	Silty clay
JARE 61	St. 18-KG	118.06	66.76	523	continental shelf	Sandy mud
JARE 61	St. 25-KG	119.34	66.62	627	continental shelf	Sandy mud
JARE 61	St. 26-KG	119.56	66.5	693	continental shelf	Silty clay
JARE 61	St. X23-KG	119.99	66.23	487	continental shelf	Pebbly mud
JARE 61	St. 83-KG	118.25	66.25	842	continental shelf	Clay
JARE 61	St. 108-KG	120.78	66.49	309	continental shelf	Silty sand
JARE 61	St. 109-KG	120.67	66.38	431	continental shelf	Sandy silt
JARE 61	St. LH1a-KG	38.25	68.99	737	continental shelf (submarine basin)	Sandy silt
JARE 61	St. LH2a-KG	38.52	68.7	310	continental shelf	Silty sand
JARE 61	St. LH3a-KG	38.48	68.47	264	continental shelf	Silty sand
JARE 61	St. LH5a-KG	38.89	68.87	219	continental shelf	Silty sand
JARE 61	St. CD4-KG	65.81	67.11	644	continental shelf	diatom ooze
JARE 61	St. CD1-KG	68.1	67.58	544	continental shelf	diatom ooze
TH82	PC302	139.5	66.32	827	continental slope	diatom ooze
TH84	PC503	78.99	65.84	3119	continental rise	silicious clay
TH83	G404	108.00	65.01	555	continental shelf	silty sand
TH84	G501	74.98	66.28	2697	continental rise	pelagic clay
TH84	G503	73.00	67.5	590	continental slope	Silicious ooze
TH89	GC1004	75.00	68.86	721	continental shelf (submarine basin)	diatom mud
TH89	GC1006	72.5	68.25	805	continental shelf (submarine basin)	silty diatom mud
TH92	GC1301	145.02	64.83	3341	abyssal plain	silty clay
TH94	GC1509	118.29	64.00	3198	continental rise	diatom mud
TH98	GC1903	94.95	60.87	4281	abyssal plain	silty clay/diatom mud
TH98	GC1904	80.64	64.16	3638	abyssal plain	silty clay
TH98	GC1905	85.31	64.17	3655	abyssal plain	silty clay
TH98	GC1906	86	65.2	2981	bottom of the continental slope	mud
TH99	GC2001	67.59	62.46	4277	abyssal plain	diatom mud
TH99	GC2002	64.82	59.86	4642	abyssal plain	diatom mud/diatom silty clay
TH99	GC2003	74.25	62.08	3959	abyssal plain	diatom silty clay
TH99	GC2005	64.32	63.76	4124	abyssal plain (end of the submarine canyon)	diatom silty clay
TH99	GC2006	73.12	66.00	2565	middle of the continental slope	silty clay
TH99	GC2009	75.12	65.15	3122	bottom of the continental slope	silty clay

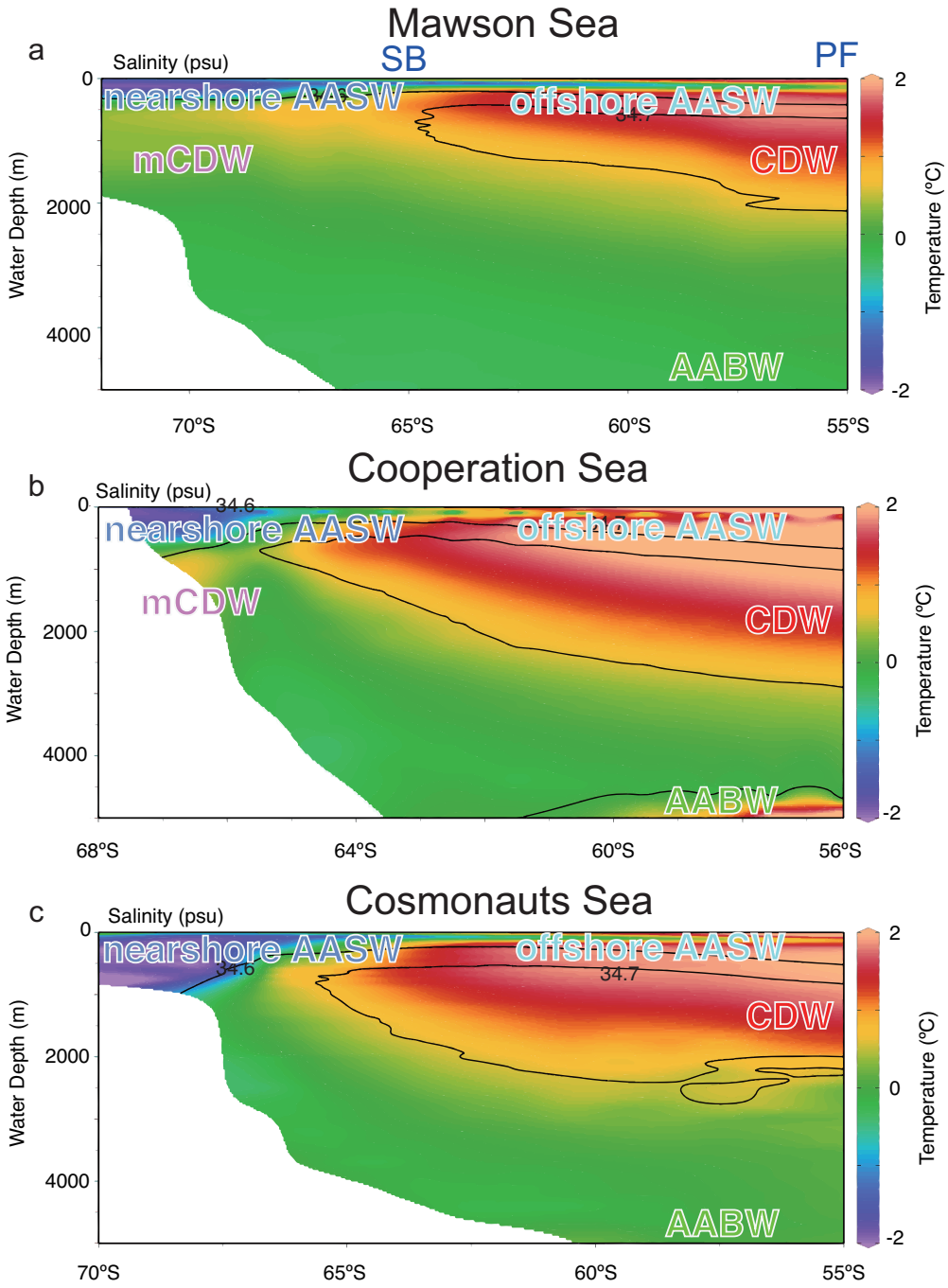


Figure 2 | Vertical section along the blue line in Figure 1 each sector in the South Ocean into hydrographic context. a, b, c, Color-mapped temperature, with salinity contours overlain, respectively, as drawn from the 2018 World Ocean Atlas. In this study area, the major fronts are the Polar Front (PF), and Southern Boundary of Antarctic circumpolar current (SB) and the major water masses are Antarctic Surface Water (AASW), Circumpolar Deep Water (CDW), and modified CDW (mCDW). Figure created with Ocean Data View (odv.awi.de).

2.2 Oceanographic setting

The Southern Ocean south of the PF is mainly occupied by three water masses, i.e., Antarctic Surface Water (AASW), circumpolar deep water (CDW), and AABW (Figure 2). AASW is a cold and freshwater mass that forms at the surface layer south of the PF (Figure 2). North of the SB, the surface water temperature reaches about 0°C due to summer solar radiation, and the subsurface cold layer (often called winter water) is thin and not very cold. South of the SB, the subsurface cold layer, which formed in winter at nearly −2°C of freezing temperature, is much thicker (Figure 2). CDW is characterized by a warm (1.5–3°C) and salty (salinity ~34.7) water mass located below a water depth of 2,000 m north of 40°S, which is ultimately derived from the North Atlantic Deep Water. South of 40°S, CDW shoals due to wind-driven upwelling (Greene et al., 2017; Marshall and Speer, 2012). As CDW moves poleward, it mixes with AASW and waters on the continental shelf, losing its core properties (Orsi and Wiederwohl, 2009), resulting in what is called modified circumpolar deep water (mCDW). AABW is a water mass occupying below 4000 m, with temperatures ranging from −0.8°C to 0°C and salinities ranging from 34.6 to 34.7. AABW is derived from mCDW and dense shelf water, which is characterized by −1.8°C and high salinity (>34.6) and formed in the Antarctic coastal polynya in several distinct areas, including the Adélie Coast (Mertz polynya) and PB (Cape Darnley polynya).

The water structure on the continental shelf region is affected by different processes, such as mCDW intrusion, sea ice formation in polynyas, and freshwater discharge from ice shelves. In this study area, polynyas (Dalton and Cape Darnley polynyas; Figure 1) is present in SC and PB (Tamura et al., 2008). In LHB, mCDW (>0°C) intrudes the continental shelf along the trough (Hirano et al., 2020). In SC, mCDW also intrudes the continental shelf along with the depression from east to west with the near-surface cold layer largely affected by Dalton polynya (Silvano et

al., 2018). On the other hand, the intrusion of mCDW is less prominent in the PB area due to prominent winter heat loss in this region (Herraiz-Borreguero et al., 2015; Guo et al., 2019).

3. Materials and methods

3.1 Surface sediment

A total of 36 surface sediment samples (0–2 cm depth) from the area of 38°E–145°E and 59–68°S (water depths ranging from 219 to 4642 m) were used in this study (Figure 1, Table 1). 17 samples were obtained from the continental shelf using a grab sampler during a cruise of I/B *Shirase* (2019–2020) of the 61st Japanese Antarctic Research Expedition (JARE-61). 19 samples were collected from the continental shelf, continental slope, and abyssal plane during the cruises of R/V *Hakurei maru* of the Antarctic Geological and Geophysical Research Project (1989–2000) conducted by the Japan National Oil Corporation using piston or gravity corers. Their core top samples were regarded as surface sediments.

Freeze-dried subsamples were weighed (approximately 1–2 g), treated with 15% H_2O_2 to remove the organic matter, and then treated with an HCl solution to remove the calcium carbonate. The samples were then wet sieved (45 μm mesh size), after which two types of permanent slides were made from the residue to quantify the abundance (Q-slide) and for faunal analysis (F-slide) using the method described by Itaki et al. (2018). Briefly, the Q-slides were prepared by transferring all residues to a 200 mL beaker containing 100 mL of distilled water. The solution was well mixed, and a 0.5 mL sample was taken from the suspension using a micropipette and dropped onto a glass slide. The sample was then dried and mounted with Norland Optical Adhesive. The F-slides were made from the remaining residues in the beaker and then mounted with Norland Optical Adhesive (NOA61).

Radiolarian skeletons were observed under an optical microscope at 100×, 200×, and 400× magnifications. The total number of radiolarians present in 1–2 g of dry sediment (radiolarian

concentration) was estimated using the following equation: RC (specimens/g) = total number of specimens in Q-slide × 200 / sample weight (g). The relative abundance (percent of total assemblage) of radiolarian taxa was estimated by counting and identifying more than 300 specimens on the F-slide; however, as many that can be identified were counted in the F-slide when radiolarian individuals were scarce.

3.2 Plankton tow sample

A plankton net of 60 μm mesh with a collecting and closing system (frame diameter of 1 m) was towed vertically at eight stations in the Mawson Sea of the Southern Ocean (Figure 1) during the cruise of TV *Umitaka maru* under the 16th Kaiyodai Antarctic Research Expedition (January 2013). In all stations, 3–4 vertical tows were carried out at a maximum speed of 0.5 m/s through intervals of 0–50, 50–100, 100–200, and 200–500 m (Table2). A calibrated flow meter (Rigosya, Japan) was used to calculate the filtered water volume.

The plankton samples were preserved in borate-buffered formalin–seawater solution (final conc. 5%) and were stained with rose bengal to distinguish living specimens from dead ones. Observation slides were prepared using the following process. Firstly, larger zooplankton was excluded from the original samples using a 100 μm mesh. Secondly, specimens smaller than 1 mm were split into aliquots using the plankton splitter between 1/16th and 1/128th of the original quantity. Thirdly, specimens were wet sieved using a 45 μm mesh. Finally, the sample was dried and mounted with Norland (NOA61). Polycystine radiolarian species were identified and counted under an optical microscope at 100× or 200× magnification. All plankton specimens on a slide were identified and counted, and their individual numbers were converted to a term of abundance (number per m^3).

Table 1 | Locations and water depth of surface sediments

Site	Depth (m)	Longitude (ºE)	Latitude (ºS)
KC5	50-100	110.01	60.00
KC5	100-200	110.01	60.00
KC5	200-500	110.01	60.00
C02	50-100	110.00	61.00
C02	100-200	110.00	61.00
C02	200-500	110.00	61.00
C03	0-50	110.01	62.00
C03	50-100	110.01	62.00
C03	100-200	110.01	62.00
C03	200-500	110.01	62.00
C04	0-50	110.00	62.50
C04	50-100	110.00	62.50
C04	100-200	110.00	62.50
C04	200-500	110.00	62.50
C05	0-50	110.00	63.00
C05	50-100	110.00	63.00
C05	100-200	110.00	63.00
C05	200-500	110.00	63.00
C06	0-50	110.00	63.50
C06	50-100	110.00	63.50
C06	100-200	110.00	63.50
C06	200-500	110.00	63.50
C07	0-50	110.00	63.98
C07	50-100	110.00	63.98
C07	100-200	110.00	63.98
C07	200-500	110.00	63.98
C08	50-100	110.00	64.30
C08	100-200	110.00	64.30
C08	200-500	110.00	64.30

3.3 Temperature and salinity profiles

In the JARE-61 cruise, vertical hydrographic data, such as temperature, salinity, and dissolved oxygen (DO), were observed by a conductivity–temperature–depth profiler (CTD) (Sea & Sun Technology 90M) installed with the grab sampler. Salinity and DO values were adjusted using calibration values from Niskin bottle bottom water and a sensor installed with a grab sampler.

The hydrographic dataset (temperature, salinity, and DO) provided by the World Ocean Atlas 2018 was also used to illustrate the distribution of water masses over a wide area. Although these hydrographic datasets provided annual, winter, spring, summer, and autumn data, the summer datasets were used to compare with the summer data observed by the JARE-61 cruise. In addition, the summer datasets were used because sediment trap studies in the Southern Ocean have demonstrated that radiolarian flux in summer contributes much of the annual flux (Abelmann and Gersonde, 1991; Abelmann, 1992).

3.4 Q-mode factor analysis for surface sediments

A Q-mode factor analysis (Imbrie et al., 1971; Imbrie and Kipp, 1973) was performed to clarify specific radiolarian assemblages for each water mass. For factor analysis, the size of the broad dataset of counted radiolarians was reduced to a total of 24 taxa. Following the procedure of Abelmann and Gowing (1997), species with abundances below 1% and species that only occur in one or two samples with abundances below 2% were eliminated from the dataset. The groups of juvenile nassellarians and spummellarians, which could not be identified to the species level, were not included in the statistical data. Furthermore, the dataset was simplified by grouping some taxa together to reduce counting uncertainty and to facilitate the reproducibility of counts for taxa with a complex taxonomy (e.g., *Acanthosphaera* spp.). About 100–400 specimens were counted on the F-slide for 36 samples, where less than 100 specimens were not identified on 17 samples due to scarce radiolarian content. Therefore, 19 samples were used for statical analysis. The PAST

statistical software package (Paleontological Statistics ver. 4.4) (Hammer et al., 2001) was used for the Q-mode factor analysis. Before the analysis, the data were normalized, following the method of Itaki et al. (2008, 2010).

4. Results

4.1 Hydrographic condition

AASW with low temperature (−2 to 1°C) and low salinity (~34.5) was observed in the surface layer (~400 m) at all continental shelf sites south of SB (Figure 3) (hereinafter called "nearshore AASW"). In some sites in the continental shelf of PB and SC areas, relatively warm water (~1°C) existed in the surface layer (upper 100 m) due to the summer solar heating. This warm surface water was especially characteristic of the polynya areas (e.g., St. X23-KG, St. CD4-KG; see Supplementary Figures). In addition, the surface layer (upper 100 m) has low salinity (33.2–34.2) due to meltwaters of sea ice and glacial ice in most sites. At the abyssal plain area north of SB, the temperature in AASW, which occupies the surface layer (upper 100 m), increases from south to north (Figure 2) (hereinafter called "offshore AASW").

CDW with high salinity (~34.7) and warm temperature (1–2°C) is observed below AASW in the abyssal plain sites north of SB (water depth of 200–3000 m). This CDW shoals toward the south due to wind-driven upwelling (Figure 2). A warm and high salinity water below 400 m is observed at continental shelf sites of SC and LHB, reflecting that mCDW intrudes the continental shelf. Especially, high temperature (>0°C) is observed at St. 83-KG and St. X23-KG (Figure 3 and Supplementary Figures), indicating a significant intrusion of relatively warm mCDW into these sites. At St. LH1a-KG, relatively warm (>0°C) water was recognized in the bottom layer, indicating an intrusion of mCDW (Figure 3 and Supplementary Figures).

On the other hand, the bottom layer in the PB area is characterized by high salinity (>34.5) and low temperature (<−1.5°C) (Figure 3), indicating the presence of Dense Shelf Water (DSW) and

subsequent AABW production near this site. AABW produced in this area sinks along the continental slope and spreads northward to fill most of the abyssal ocean deeper than 4000 m (Figure 2).

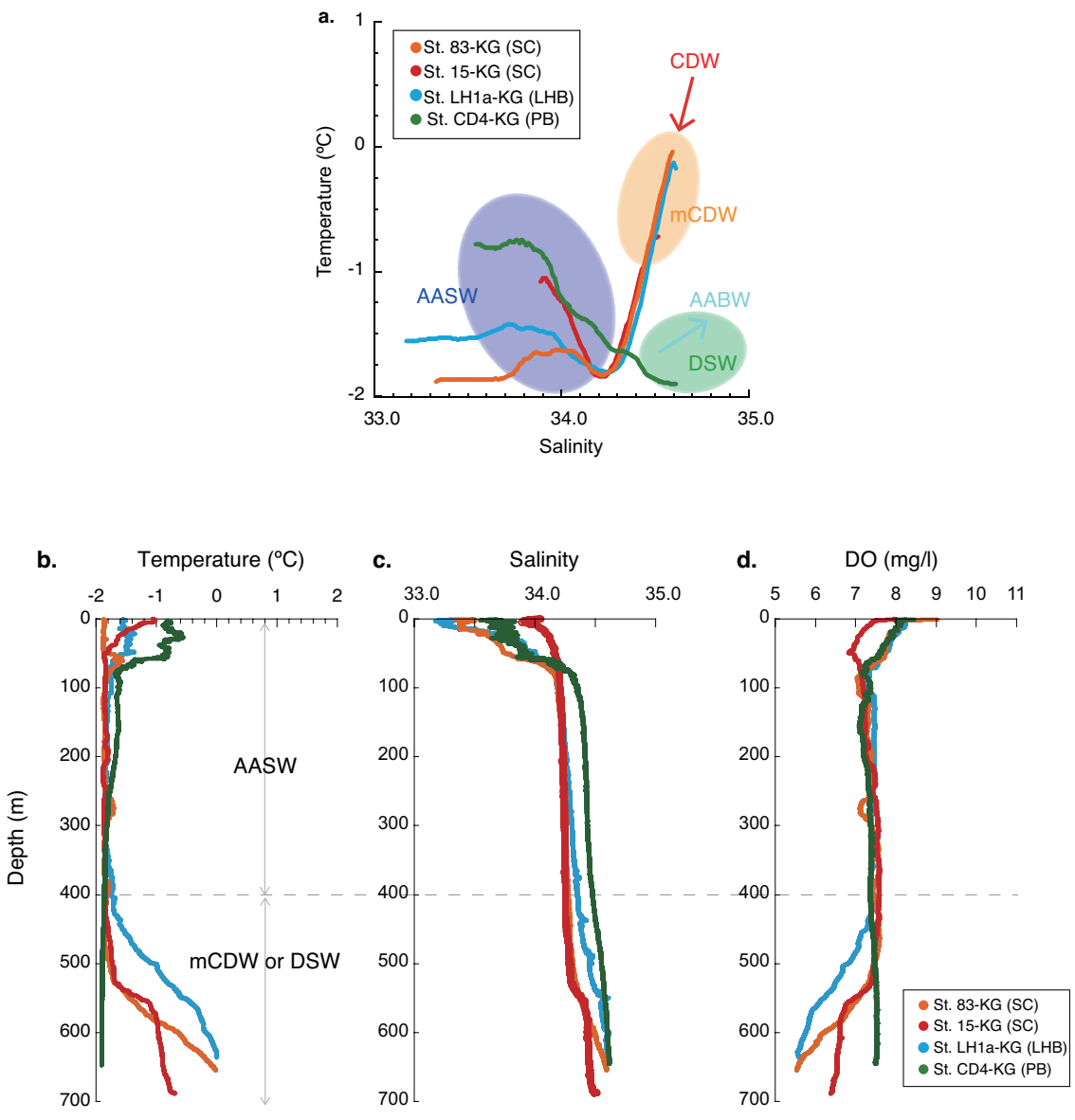


Figure 3 | Temperature and Salinity profiles. a, Example temperature and salinity profiles in each area (smoothed data). **b, c, d** Example vertical profiles of temperature, salinity, and Dissolved oxygen in each area, respectively.

4.2 Surface sediments

4.2.1 Radiolarian abundance and assemblage

Figures 1 and 4a show the radiolarian absolute abundance in surface sediments (specimens/g) at the studied sites. The abundance ranged between 0 and 19600 specimens/g (mean: 4700 specimens/g) at the continental shelf and between 0 and 426700 specimens/g (mean: 77300 specimens/g) at the continental rise and abyssal plain (Figure 4a). However, radiolarians were absent or very rare at stations on the continental slope (Figure 4a). The radiolarian preservation is generally good in all stations where radiolarians were observed. The radiolarian abundance tends to increase with water depth but stays relatively constant in the abyssal plain stations with relatively high values. On the other hand, the abundance varies widely among the continental shelf stations, with lower prevalence in LHB and PB and higher prevalence in SC (Figure 4a).

A total of 52 taxa of radiolarians were found in this study. The number of species tends to be higher at the continental slope and abyssal plain (less than 35 taxa/sample) than at the continental shelf (less than 23 taxa/sample). The most dominant taxa were *Antarctissa denticulata*, accounting for 29–73% of the total assemblage for each sample, followed by *Antarctissa strelkovi* (0–21%), *Lithomelissa* sp. A (0–12%), and *Larcopyle buetschlii* (0–24%). Figure 4b shows the composition of the above species for each site.

As accompanied radiolarians, *Acanthosphaera* spp., *Cenosphaera* spp., *Cycladophora bicornis*, *Larcopyle nebulum*, *Larcopyle weddelium*, *Spongopyle osculosa*, and *Peripyramis* sp. were commonly observed in the abyssal plain. However, their occurrence was not observed at the continental shelf (Figure 4b). On the other hand, *Cycladophora davisiana*, *Larcopyle buetschlii*, *Zygocircus archicircus*, *Pseudodictyophimus gracilipes*, *Lithelius minor*, *Phormospyris stabilis antarctica*, *Saccospyris antarctica*, and *Spongotrochus glacialis* were common not only in the abyssal plain but also in the continental shelf. *Spongodiscus resurgens*, *Lithomelissa* sp. A,

Lithelius nautiloides, and *Antarctissa strelkovi* were mainly found in the continental shelf samples. Similar radiolarian assemblages observed in this study have been recognized in previous studies in the Southern Ocean (e.g., Petrushevskaya, 1967; Abelmann et al., 1999; Cortese and Prebble, 2015).

Plectacantha oikiskos and *Rhizoplegma boreale* only appeared in the coastal area. Especially, the abundances of the *Plectacantha oikiskos* are quite conspicuous. *Plectacantha oikiskos* and *Rhizoplegma boreale* were observed in the coastal areas across the world's oceans, such as the Norwegian Sea and subarctic Pacific (Jørgensen, 1900; Jørgensen, 1905; Bjørklund, 1976; Ikenoue et al., 2012). Furthermore, Nishimura et al. (1997) describe these taxa as coastal area assemblages even in the Southern Ocean. Thus, the result of this study is consistent with previous studies.

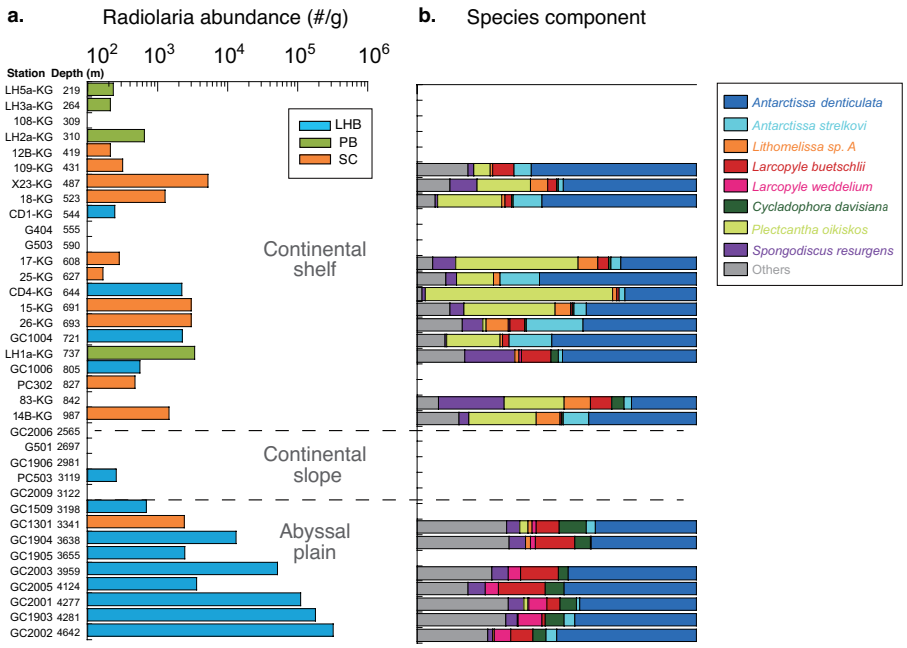


Figure 4 | Radiolarian abundance and Faunal components. a, Radiolarian abundance in each site. **b,** Faunal components of abundant taxa in each site.

4.2.2 Q-mode factor analysis for surface sediments

The Q-mode factor analysis is conducted based on 19 samples collected from the 431–4642 m water depth and 24 taxa, resulting in the definition of four factors, accounting for about 80% of the variance of the included fauna (Tables 2 and 3). Figure 5 shows distribution maps of each factor loading in the entire examined area. Figure 6 shows the close-up maps of the SC area.

Factor 1 (F1) is the dominant factor and explains 52% of the variance of the included fauna. In F1, *Antarctissa denticulata*, *Antarctissa strelkovi*, and *Lithelius nautiloides* show high scores (3.21, 2.61, and 2.47, respectively) (Table 4). In addition, F1 shows factor loadings higher than 0.5 at most continental shelf samples (water depth of 431–987 m) and loading from 0.10 to 0.31 at abyssal plain samples (water depth of 3341–4642 m) (Figures 5a and 6a, Table 3).

Factor 2 (F2) explains 17% of the variance and shows negative loadings less than −0.7 at abyssal plain samples (Figures 5b and 6b, Table 3). The radiolarian assemblage in F2 consists of 13 taxa (*Antarctissa denticulata*, *Cenosphaera* spp., *Cycladophora davisiana*, *Larcopyle buetschlii*, *Larcopyle weddelium*, *Larcopyle pylomaticus*, *Peripyramis* sp., *Phormospyris stabilis antarctica*, *Pseudodictyophimus gracilipes*, *Saccospyris antarctica*, *Spongopyle osculosa*, *Spongotrochus glacialis*, and *Zygocircus archicircus*) (Table 4). In general, negative scores mean the absence of taxa in the corresponding factor. However, due to the negative loadings of F2, negative scores would mean the presence of the corresponding taxa. Therefore, these taxa are present in F2.

Factor 3 (F3) explains 6.6% of the variance and shows factor loadings higher than 0.5 at continental shelf samples in SC and LHB areas and loading from −0.04 to 0.25 at abyssal plain samples and continental shelf samples in the Cooperation Sea (Figures 5c and 6c, Table 3). Values higher than 0.5 are observed at St. X23-KG, St. 83-KG in the SC, and St. LH1a-KG in LHB

(Figure 5c, 6c). For F3, *Actinomma leptoderma*, *Larcopyle buetschlii*, *Lithomelissa* sp. A, and *Spongodiscus resurgens* show high scores (2.06, 1.04, 2.85, and 2.75, respectively) (Table 4).

Factor 4 (F4) explains 4.2% of the variance and shows high loadings at coastal site samples, especially at ST. CD4-KG off Cape Darnley in the PB area and St. 15-KG and St. 17-KG in the SC area (Figures 5d and 6d, Table 3). For F4, *Plectacantha oikiskos* and *Lithomelissa* sp. A show high score (4.26, 1.35) (Table 4).

4.3 Plankton tows

4.3.1 Radiolarian abundance and assemblage

Figure 7 shows the living radiolarian abundance at the studied sites. The abundance of total radiolarians was greatest at KC05, the most northerly site, and the abundance of living radiolarians was 100 times at KC05 compared with the other sites. Generally, the radiolarians are not found in the surface layer above 50 m in most sites. The maximum numbers of living radiolarians were recognized in a water depth of 50–100 m and 100–200 m. The number of living radiolarians decreased with water depth.

A total of 26 radiolarian taxa were identified in the plankton samples (see Appendix data). These species are generally found in the Southern Ocean and are similar to the species from surface sediments. Juvenile *Antarctissa*, *Antarctissa denticulate*, and *Lithocampe* spp. were the dominant species from the plankton tow samples. *Lithocampe* spp. was rarely observed in the surface sediment samples, but they were abundant in plankton tow samples. *Antarctissa denticulata* was found from 50 to 500 m, while its juvenile was abundant in the surface layer (50–100 m). This tendency for adults and juveniles to thrive at different depths has also been observed in *Larcopyle buetschlii* and its juveniles in the Sea of Japan (Itaki, 2016).

4.3.2 Comparison of living and fossil radiolarian assemblages

Of the 19 taxa high loadings of the Q-mode factor analysis, 14 taxa were identified and five taxa (*Lithelius nautiloides*, *Larcopyle pylomaticus*, *Cenosphaera* spp., *Zygocircus archicircus*, and *Plectacantha oikiskos*) were absent in the plankton tow samples. *Antarctissa denticulata* and *Antarctissa strelkovi* loaded with F1 were present throughout the surface to subsurface layers. Of the taxa loadings of F2, *Phormospyris stabilis antarctica*, *Saccospyris antarctica*, *and Spongotrochus glacialis* were found at the surface layer (50–100 m). In contrast, *Cycladophora davisiana*, *Larcopyle buetschlii*, *Larcopyle weddelium*, *Peripyramis* sp., *Spongopyle osculosa*, *Pseudodictyophimus gracilipes*, *Lithomelissa* sp. A, *Actinomma leptoderma*, and *Spongodiscus resurgens* loadings of F2 and F3 were found in deeper waters (100–200 m and 200–500 m) (Figure 7 and Supplementary Figures).

Table 3 | Varimax factor matrix

Site	Factor 1	Factor 2	Factor 3	Factor 4
St. 109-KG	0.77	-0.39	0.14	0.16
St. X23-KG	0.64	-0.25	0.52	0.36
St. 18-KG	0.89	-0.19	0.03	0.23
St. 17-KG	0.33	-0.23	0.45	0.71
St. 25-KG	0.93	-0.13	0.14	0.17
St. CD4-KG	0.31	-0.05	0.11	0.83
St. 15-KG	0.46	-0.23	0.18	0.62
St. 26-KG	0.79	-0.20	0.40	0.15
GC1004	0.79	-0.15	0.04	0.31
St. LH1a-KG	0.39	-0.55	0.56	0.10
St. 83-KG	0.15	-0.20	0.87	0.24
St. 14B-KG	0.57	-0.11	0.46	0.39
GC1301	0.14	-0.76	0.22	0.13
GC1904	0.10	-0.80	0.25	0.03
GC2003	0.13	-0.90	0.07	0.10
GC2005	0.11	-0.88	0.08	0.10
GC2001	0.13	-0.81	0.12	0.14
GC1903	0.20	-0.84	0.10	0.07
GC2002	0.31	-0.84	-0.04	0.16

Table 4 | Varimax factor score matrix with scaled values

Species	Factor 1	Factor 2	Factor 3	Factor 4
Acanthosphaera spp.	-0.22	-0.76	0.15	-0.19
Actinomma leptoderma	-0.29	-0.15	**2.06**	-0.25
Antarctissa denticulata	**3.21**	**-1.21**	-0.09	0.79
Antarctissa strelkovi	**2.61**	0.29	-0.28	-0.35
Cenosphaera spp.	-0.28	**-1.30**	0.01	-0.11
Cycladophora bicornis	-0.19	-0.78	0.15	0.00
Cycladophora davisiana	-0.47	**-1.51**	0.77	-0.08
Larcopyle buetschlii	0.25	**-1.36**	**1.04**	-0.33
Larcopyle nebulum	-0.13	-0.82	-0.51	0.15
Larcopyle pylomaticus	-0.35	**-1.23**	0.24	0.07
Larcopyle weddelium	-0.19	**-1.50**	-0.51	-0.01
Lithelius nautiloides	**2.47**	0.16	0.01	-0.54
Lithocampe spp.	0.25	-0.42	0.23	0.43
Lithomelissa sp. A	0.39	0.57	**2.85**	**1.35**
Peripyramis sp.	-0.25	**-1.00**	-0.24	0.08
Plectcantha oikiskos	-0.15	0.44	-0.41	**4.26**
Phormospyris stabilis antarctica	0.42	**-1.19**	-0.26	0.25
Pseudodictyophimus gracilipes	-0.22	**-1.32**	-0.05	0.07
Rhizoplegma boreale	0.45	0.29	0.91	0.42
Saccospyris antarctica	0.11	**-1.31**	-0.53	0.52
Spongodiscus resurgens	-0.07	-0.25	**2.75**	-0.07
Spongopyle osculasa	-0.31	**-1.51**	-0.58	0.12
Spongotrochus glacialis	-0.25	**-1.01**	0.45	0.03
Zygocircus archicircus	0.22	**-1.13**	0.71	-0.47

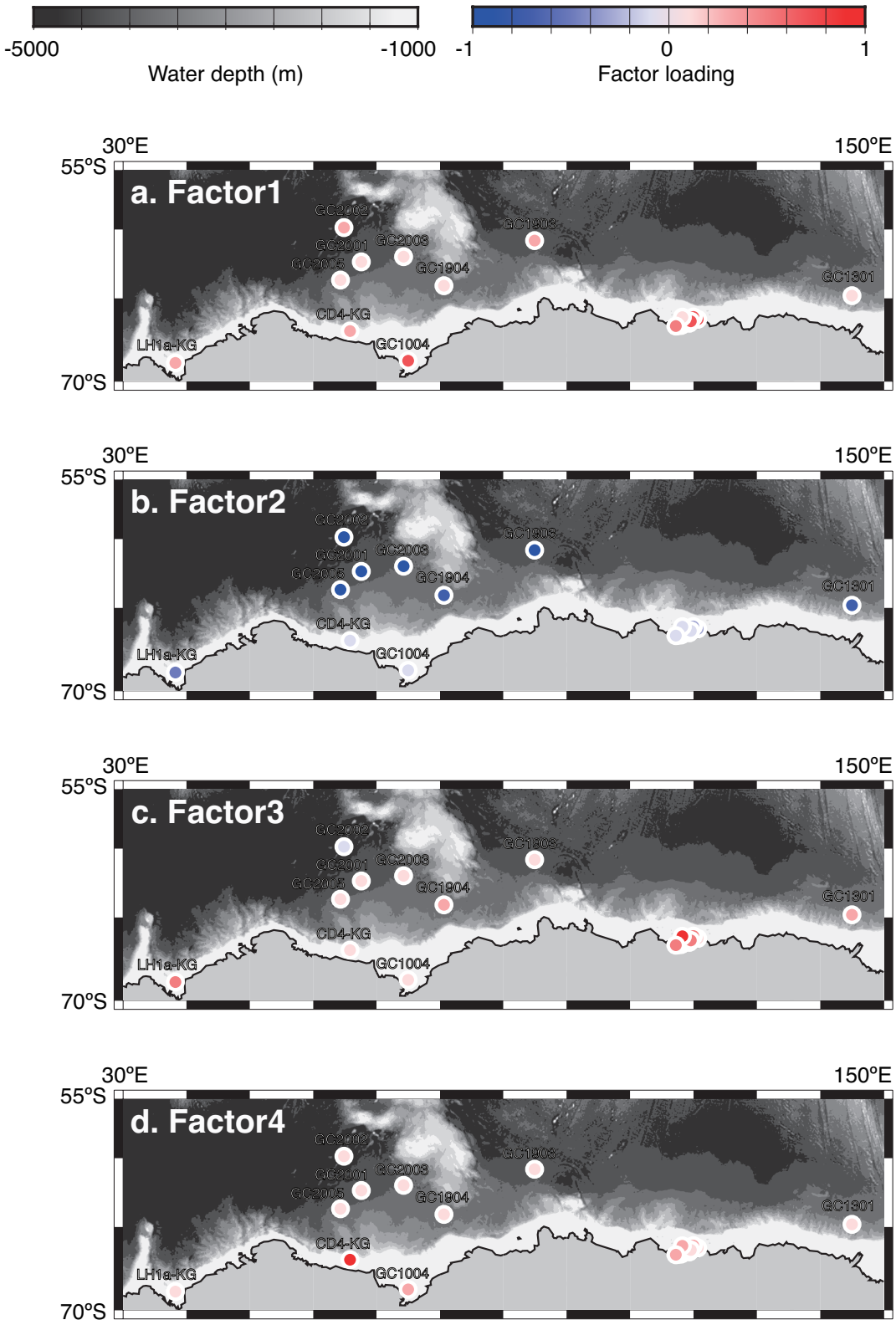


Figure 5 | Geographic distribution of factor 1–4 loadings. a, b, c, d, Geographic distribution of factor loadings of F1, F2, F3, F4, respectively. The maps showing previously published data overlain on the BEDMAP 2 subglacial topography (Fretwell et al., 2013).

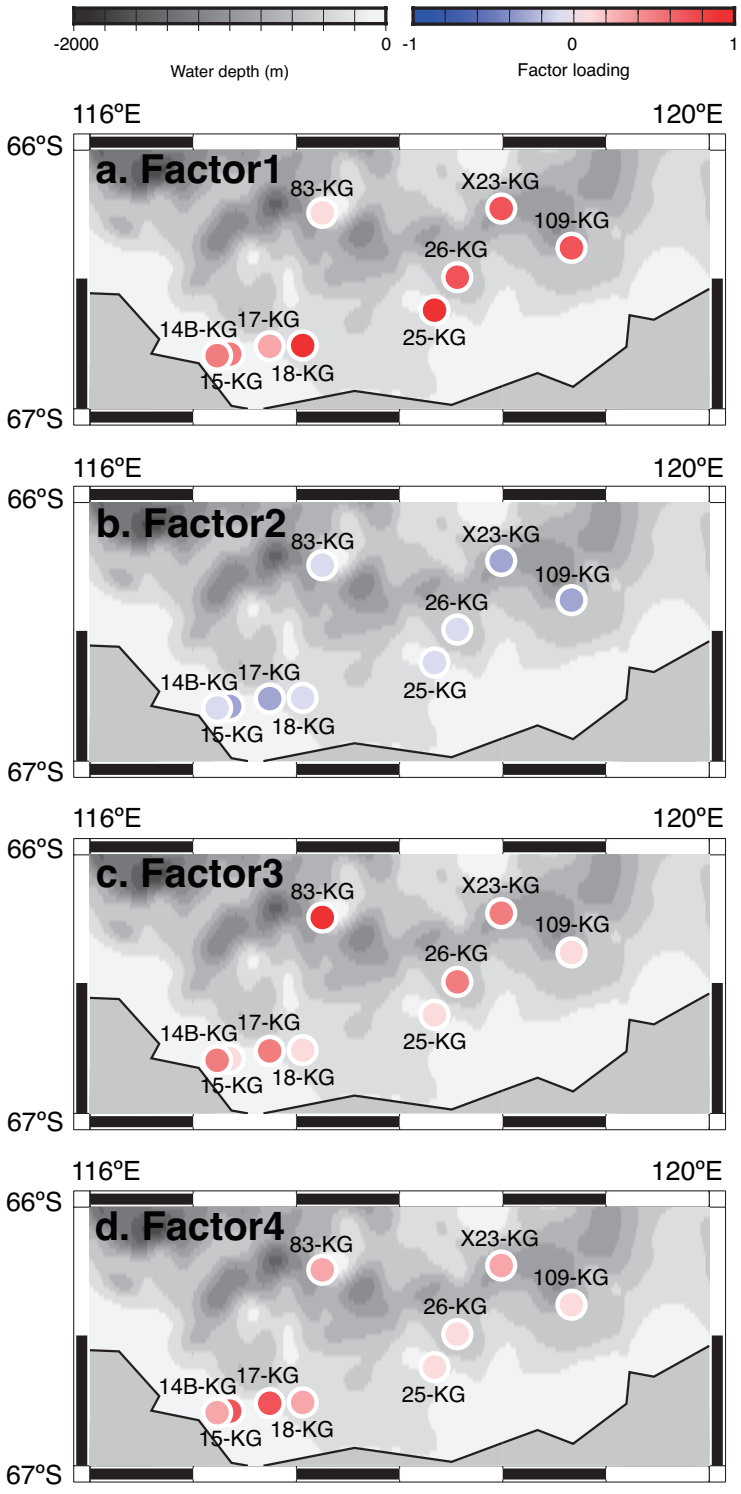


Figure 6 | Geographic distribution of factor 1–4 loadings in SC site. a, b, c, d, Geographic distribution of factor loadings of F1, F2, F3, F4, respectively, in SC site. The maps showing previously published data overlain on the BEDMAP 2 subglacial topography (Fretwell et al., 2013).

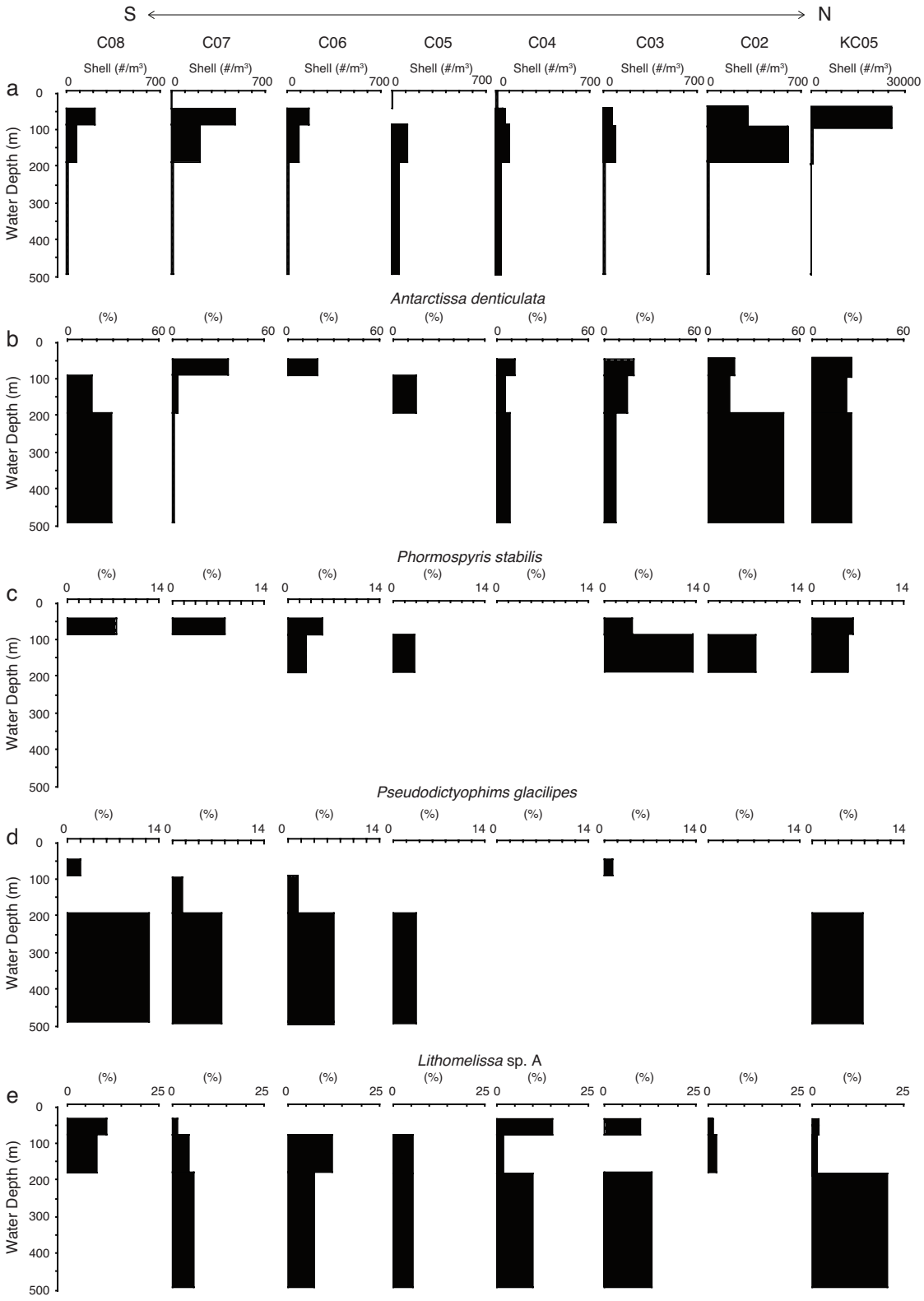


Figure 7 | The data from Plankton tow samples a, Depth profiles of total living radiolarians **b, c, d,** Living depth profiles of major radiolarian species from plankton tow samples.

5. Discussion

Although most radiolarian species live in surface to subsurface layers shallower than 200 m in the world ocean, deep-dwelling species distributed deeper than 200 m show discrete depth intervals related to the vertical water masses (e.g., Kling, 1976; Kling and Boltovskoy, 1995; Abelmann and Gowing, 1997). Therefore, such depth zonation of radiolarian assemblages through the water column from the surface to bottom reflects those in surface sediments (Itaki, 2003). Radiolarian assemblages related to different water masses in the Southern Ocean are discussed in this section based on a comparison between living radiolarian collected from plankton tow samples and Q-mode factors for radiolarian fossil from surface sediments.

5.1 Continental shelf AASW group (Factor 1)

F1 shows the highest and lowest loadings at continental shelf and abyssal plain samples, respectively (Figure 5a). *Lithelius nautiloides*, *Antarctissa denticulata*, and *Antarctissa strelkovi* show relatively high scores for this factor (Table 4). *Lithelius nautiloides* is abundant from surface sediments south of the PF (Hays, 1965; Petrushevskaya, 1971). *Antarctissa denticulate* presents in surface sediments south of the PF and is more frequent south of SB (Petrushevskaya, 1971). Abelmann (1999) showed that *Antarctissa strelkovi* is highly distributed at 53°–58°S and is limited south of the PF in the Weddell Sea (40°W–10°E). In contrast, Petrushevskaya (1971) showed that the abundance of *Antarctissa strelkovi* in surface sediment samples gradually increases from north to south (10–180°E) (Petrushevskaya, 1971). Dow (1978) concluded that *Antarctissa strelkovi* is highly distributed south of the PF based on factor analysis of the surface sediment (80–110°E). Although the reasons for the regional differences in the distribution of *Antarctissa strelkovi* are unclear, *Antarctissa strelkovi* is more abundant in the higher latitudes (continental shelf sites) in this study area (30–150°E). These previous studies are consistent with

the results in this study, showing that the three species loadings of F1 are abundant south of the SB.

In the data from plankton tow samples in this study, *Antarctissa denticulata* and *Antarctissa strelkovi* loadings of F1 were widely distributed in the surface to subsurface water (50–100 m, 100–200 m, and 200–500 m), showing that these two species live in the surface water south of the PF (Figure 7 and see Appendix data). Previous studies from plankton tow also show that three species loadings (*Antarctissa denticulata*, *Antarctissa strelkovi*, and *Lithelius nautiloides*) of F1 dominantly occur in surface water (~200 m) south of the PF (Morley and Stepien, 1985), which is consistent with the results of this study. The cold water cooled by meltwater from such ice sheets and sea ice is located in the nearshore AASW (Figure 2), indicating that *Antarctissa denticulata*, *Antarctissa strelkovi*, and *Lithelius nautiloides* inhabit the nearshore AASW even colder than offshore AASW.

5.2 Offshore AASW and CDW groups (Factor 2)

F2 shows the highest and lowest loadings at the abyssal plain and continental shelf samples, respectively (Figures 5b and 6b, Table 3), suggesting that the F2 taxa live in the open ocean north of SB. Although off shore AASW, CDW, and AABW are distributed (Figure 2), radiolarian-rich layers are limited to a depth below 1000 m in the oceans (Boltovskoy, 2017), and radiolarians living in AABW are likely to be scarce. Thus, 13 taxa loading relatively high factor scores (>1.0) could be living in the offshore AASW or CDW.

5.2.1 Offshore AASW group

Of the F2 taxa loadings, *Antarctissa denticulate*, *Phormospyris stabilis antarctica*, *Spongotrochus glacialis*, and *Saccospyris antarctica* were recognized in the surface water (50–100 m) from plankton tow samples (Figure 7 and see Appendix data). Moreover, previous studies of plankton tows and surface sediments show that these taxa are observed north of the SB (Morley

and Stepien, 1985; Abelmann and Gowing, 1997; Abelmann et al., 1999). Therefore, these taxa are likely to live in offshore AASW in the Southern Ocean. Comparing F1 taxa with these taxa, all taxa are different, except for *Antarctissa denticulata*. This suggests that radiolarian assemblage differs between nearshore and offshore.

Antarctissa denticulata reaches high factor loadings (loadings) (>1.0) in two factors (F1 and F2). The other two species (*Antarctissa strelkovi* and *Lithelius nautiloides*) that were loaded with high scores in F1 only are highly abundant on the nearshore, while *Antarctissa denticulata* is distributed in the wide region (south of 50°S) compared to these two species (Abelmann, 1999; Hays 1965). Therefore, it is suggested that *Antarctissa denticulata* shows high loadings not only on F1 (continental shelf) but also on F2 (abyssal plain), which is the offshore factor.

5.2.2 CDW group

Of the nine F2 taxa loadings and not identified from the surface water, the prevalence of six taxa (*Cycladophora davisiana*, *Larcopyle buetschlii*, *Larcopyle weddelium*, *Peripyramis* sp., *Pseudodictyophimus gracilipes*, and *Spongopyle osculosa*) increased with depth, and these taxa were most abundant in 200–500 m from plankton tow samples (Figure 7). Previous studies report that *Larcopyle pylomaticus*, *Larcopyle weddelium*, *Spongopyle osculosa*, and *Cycladophora davisiana* are also observed below a water depth of 200 m from the plankton tow in the Southern Ocean (Morley and Stepien, 1985). The habitat depth of *Larcopyle buetschlii* differs between juveniles and adults in the Sea of Japan, in which the adult is abundant between 200 and 1000 m of water depth. In contrast, the juvenile *Larcopyle buetschlii* is restricted to shallow water above 200 m (Itaki, 2016). Most of *Larcopyle buetschlii* observed in this study are adults, hence *Larcopyle buetschlii* that live in deeper habitats are likely counted. Although the ecological information on *Zygocircus archicircus* is uncertain, *Zygocircus* group is recognized in surface sediment and sediment trap samples in the oceans worldwide (e.g., Abelmann et al., 1992;

Boltovskoy and Riedel, 1980; Renz, 1976) and is reported to live in the mesopelagic zone in the North Pacific Ocean (Okazaki et al., 2004; Kling and Boltovskoy, 1995). The habitat depth of *Zygocircus archicircus* in the Southern Ocean is still unknown; however, if F2 taxa have similar habitat depths in the Southern Ocean, they can be identified as species that dwell in the mesopelagic zone. Although the habitat depth of *Cenosphaera* spp. has been unclear, they are likely to inhabit the mesopelagic zone of the Southern Ocean because they have not been found in the plankton nets from the surface layer of the Southern Ocean.

Thus, nine taxa that appear in F2 are suggested to dwell in deep water, indicating that they also dwell in CDW, warm deep water, in the south of 60° of the Southern Ocean. This result is also supported by the previous study of the horizontal and vertical distributions of living polycystine radiolarian taxa on the N–S transect (30–58°S) (Abelmann and Gowing, 1997), in which *Cycladophora davisiana*, *Larcopyle pylomaticus*, *Larcopyle weddelium*, *Pseudodictyophimus gracilipes*, and *Spongopyle osculosa* are closely related to the CDW factor (below 400 m) based on the Q-mode factor analysis.

5.3 mCDW group (Factor 3)

F3 shows the highest loadings at continental shelf samples in SC and LHB and the lowest loadings at the continental shelf in PB and abyssal plain samples (Figure 5c, and 6c). This factor is characterized by *Larcopyle buetschlii*, *Lithomelissa* sp. A, *Actinomma leptoderma*, and *Spongodiscus resurgens.* The plankton tow data in this study shows that these taxa were found in shallow and deep waters and were abundant in 200–500 m (Figure 7 and Supplementary Figures). As mentioned above, *Larcopyle buetschlii* (adult) dwells in deep water, and it was determined as the species that dwell in the mesopelagic zone. *Actinomma leptoderma* has been reported in high-latitude oceans, such as the Arctic Ocean and Greenland Sea (Hülsemann, 1963; Tibbs, 1967; Petrushevskaya, 1969), and observed in the relatively warm mesopelagic zone (Jørgensen, 1905).

It has been reported that *Lithomelissa* sp. A dwells in the mesopelagic zone in the Southern Ocean (~55°S) from factor analysis of plankton tow (Abelmann and Gowing, 1997). These insights suggest that these taxa inhabit relatively deep waters.

The high loading values in F3 were found at St. 83-KG, St. X23-KG, and LH1a-KG (0.87, 0.52, 0.56, respectively). The vertical profiles of temperature and salinity suggest the intrusion of mCDW into these sites (Figure 3 and Supplementary Figures). Therefore, if these taxa also live in the south of SB in the deep ocean, they can be identified as mCDW taxa. However, plankton tow data at the continental shelf are required to further understand the habitat depth of this species south of 65°S.

5.4 Coastal group

F4 shows the highest loadings in coastal samples (St.14B-KG, St. 15-KG, St. 12B-KG, St. 17-KG, and CD4-KG). Moreover, F4 is characterized by *Plectacantha oikiskos* and *Lithomelissa* sp. A. *Plectacantha oikiskos* has been observed in the coastal areas of high latitudes, such as fjords of the Norwegian Sea, Southern Ocean (e.g., Jørgensen, 1905; Nishimura et al, 1997), and reported to be common in the plankton at the ice edge in the Greenland Sea (Swanberg and Eide, 1992). *Lithomelissa* sp. A was abundant in the coastal area in the Southern Ocean (Petrushevskaya, 1967).

The sites with high F4 loadings (St.14B-KG, St. 15-KG, St. 12B-KG, St. 17-KG, and CD4-KG) were located near polynya (the edge of sea ice) and the edge of the glacier areas, suggesting that these taxa (*Plectacantha oikiskos* and *Lithomelissa* sp. A) may be related with the environment of the ice edge. *Lithomelissa* sp. A exhibited high loadings in both F3 and F4 and may be influenced by the ice edge environment as well as the water masses.

6. Conclusion

For the first time, this study provided the radiolarian assemblage dataset from the continental shelf to the abyssal plain of the Southern Ocean (south of the PF) based on the analysis of surface sediment and plankton tow samples. The abundance and diversity of radiolarians in surface sediments in the Southern Ocean (south of the PF) increase with water depth.

The four factors (F1–F4) related to the hydrographic conditions were found in the factor analysis through Q-mode factor analysis of the radiolarian dataset for 24 species and species groups (Figure 8) at 19 sites (Figure 9). F1 shows a high loading in continental shelf sites, suggesting that the taxa inhabit nearshore AASW, affected by ice sheet and sea ice melting water. F2 shows high loading on the abyssal plain sites, suggesting that the F2 taxa loadings inhabit the north of SB. The plankton tow data shows that the F2 taxa loadings consisted of the taxa living in CDW and offshore AASW. The taxa living in CDW and offshore AASW were identified (Figure 9). F3 shows loadings with high value at the continental shelf sites (St. 83-KG, St. X23-KG, and LH1a-KG) where mCDW intrudes into the continental shelf, suggesting that this assemblage lives in the mCDW. F4 shows loadings on the coastal area (ice edge areas), suggesting that this assemblage dwells near ice edge areas.

Consequently, the datasets in this study provide radiolarian assemblage related to hydrographic conditions. However, the sediment data do not provide direct evidence of habitat depth distribution of the radiolarians in the Southern Ocean south of the SB. Hence, it is crucial to accurately identify the habitat depth using plankton tow experiments in the Southern Ocean south of SB in the future.

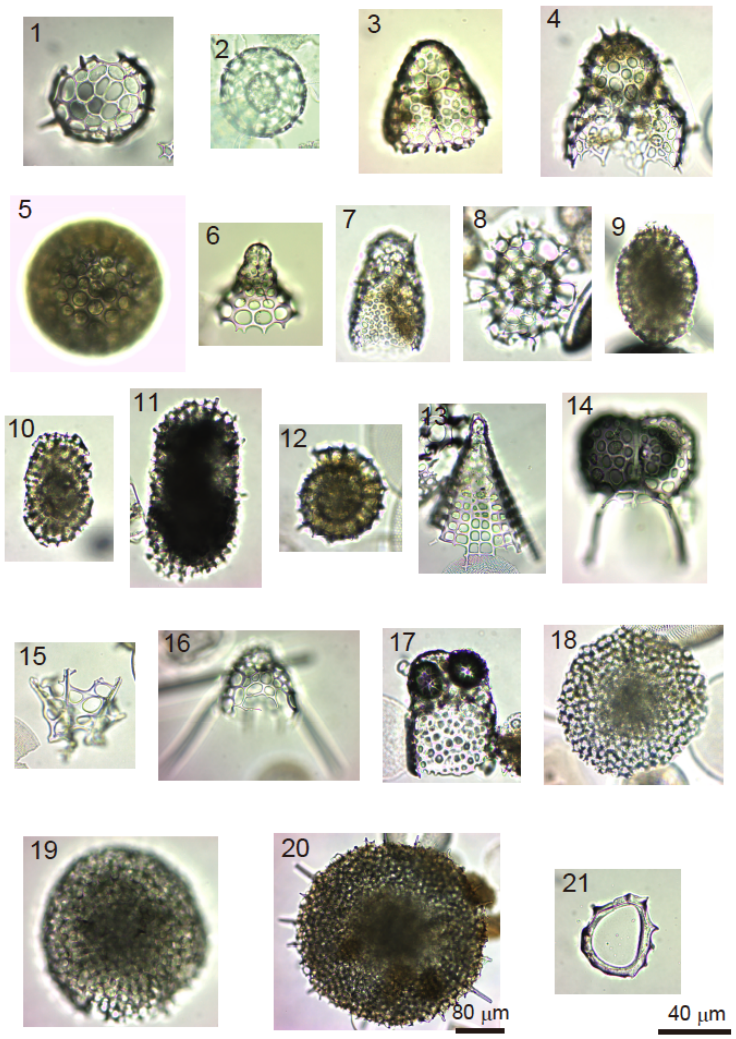
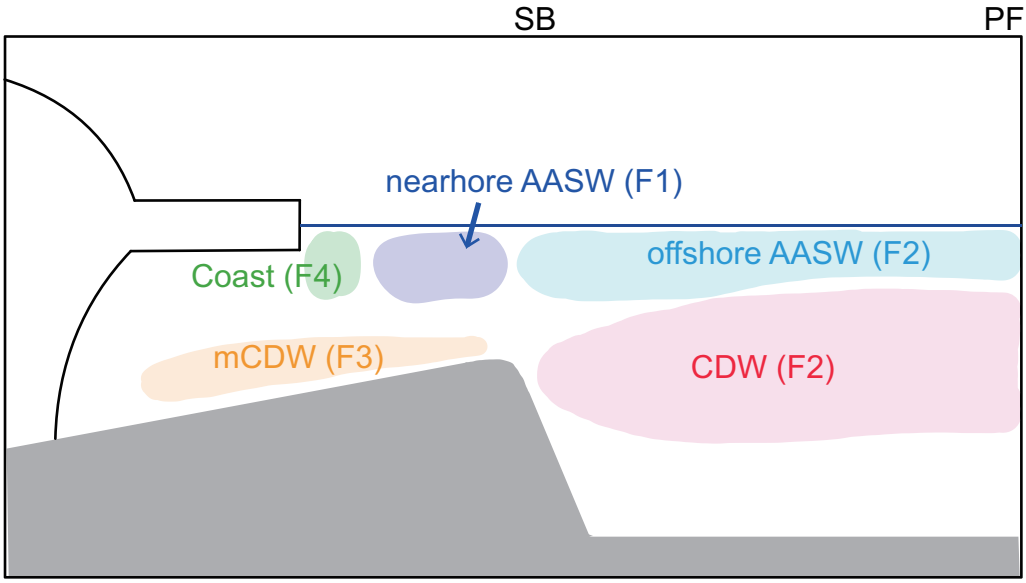


Figure 8 | 1, *Acanthosphaera* spp. (sample GC1904). 2, *Actinomma leptoderma* (Jorgensen) (GC1904). 3, *Antarctissa denticulata* (Ehrenberg) (GC1904). 4, *Antarctissa strelkovi* Petrushevskaya (14B-KG). 5, *Cenosphaera* spp. (GC1904). 6, *Cycladophora davisiana* Ehrenberg (GC1904). 7, *Lithomelissa* sp. A (C2002). 8, *Larcopyle buetschlii* Dreyer (GC1904) (Juvenile). 9, *Larcopyle buetschlii* Dreyer (14B-KG) (Adult). 10, *Larcopyle weddelium* (Lazarus, Faust and Popova-Goll) (GC1904). 11, *Larcopyle pylomaticus* (Riedel) (GC1904). 12, *Lithelius nautiloides* Popofsky (14B-KG). 13, *Peripyramis* sp. (GC2002). 14, *Phormospyris stabilis* (Goll) *antarctica* (Haecker) (GC2002). 15, *Plectacantha oikiskos* (Jørgensen) (14B-KG). 16, *Pseudodictyophimus gracilipes* (Bailey) (GC2002). 17, *Saccospyris antarctica* Haecker (GC1904). 18, *Spongodiscus resurgens* Ehrenberg (12B-KG). 19, *Spongopyle osculosa* Dreyer (GC2002). 20, *Spongotrochus glacialis* Popofsky (14B-KG). 21, *Zygocircus productus* Popofsky (GC1904).



Factor 1 (nearshore AASW)	Factor 2 (offshore AASW)	Factor 2 (CDW)	Factor 3 (mCDW)	Factor 4 (Coast)
Antarctissa denticulata	*Antarctissa denticulata*	*Cenosphaera* spp.	*Actinomma leptoderma*	*Lithomelissa* sp. A
Antarctissa strelkovi	*Phormospyris stabilis antarctica*	*Cycladophora davisiana*	*Larcopyle buetschlii*	*Plectcantha oikiskos*
Lithelius nautiloides	*Saccospyris antarctica*	*Larcopyle buetschlii*	*Lithomelissa* sp. A	
	Spongotrochus glacialis	*Larcopyle pylomaticus*	*Spongodiscus resurgens*	
		Larcopyle weddelium		
		Peripyramis sp.		
		Pseudodictyophimus gracilipes		
		Spongopyle osculasa		
		Zygocircus archicircus		

Figure 9 | Schematic figures showing the construction of the radiolarian assemblage. In this study area, the major fronts are the Polar Front (PF) and Southern Boundary of Antarctic circumpolar current (SB) and major water masses are Antarctic Surface Water (AASW), Circumpolar Deep Water (CDW), and modified CDW (mCDW).

Chapter 3

Developing an index for assessing circumpolar deep water strength and reconstructing circumpolar deep-water inflow during the Last interglacial in the high-latitude Southern Ocean

Abstract

The Last Interglacial (LIG: 130,000–115,000 years ago) was a period of warmer global mean temperatures than the preindustrial level and dynamic fluctuations of the East Antarctic Ice Sheet (EAIS). A better understanding of the interaction between EAIS and Southern Ocean (SO), especially the strength of CDW inflow in the high-latitude SO, during the LIG would provide valuable insights for projecting EAIS variability in future warming scenarios. However, the changes in the strength of the CDW inflow in the high-latitude SO during LIG remain mostly elusive. In this study, I propose a radiolarian CDW index based on radiolarian assemblage data in surface sediments collected from the high-latitude SO and apply it to the marine sediment core to reconstruct variability of the CDW inflow at the high-latitude site during the LIG period. My results suggest that the strength of CDW inflow significantly varied with rapid reduction and two episodic resumptions during the LIG. This result implies that the strength of CDW inflow relates to EAIS melting.

1. Introduction

In recent decades, Antarctica has been experiencing increased ice mass loss. Antarctic ice mass loss was first recognized in West Antarctica in the 1970s (Mercer, 1978), which is presumably linked to oceanic variability such as the strength of warm Circumpolar Deep Water (CDW) (Jenkins et al., 2018). On the other hand, the East Antarctic Ice Sheet (EAIS) has often been considered less vulnerable to ocean-climate warming compared to West Antarctica. However, recent observations suggest that the marine-based EAIS may also be susceptible to ocean-climate forcings, particularly the enhanced southward CDW inflow (Rintoul et al., 2016; Yamazaki et al., 2021). Therefore, there is a possibility that the EAIS mass may loss due to ocean-climate forcing in future warming scenarios. A key issue is that observational time series records are generally too short to determine whether recent trends will continue in future warming scenarios.

The temporal records of paleoclimate during the Last Interglacial (LIG: 130,000–115,000 years ago), when global temperatures were approximately 1ºC warmer than the preindustrial level (Friedrich et al., 2016), provide an opportunity to elucidate whether the variability of CDW inflow played a critical role in the significant mass loss of the EAIS under warm climate conditions. Sediment core records in the Southern Ocean (SO) reveal dynamic fluctuations of the ice sheet in the Wilkes Subglacial Basin (WSB) of East Antarctica during the LIG (Chapter 1). These records indicate thinning, melting, and potential retreat, leading to ice loss during both the early and late stages of the LIG. However, it has been unclear whether the enhanced CDW inflow is the primary cause of mass loss in the EAIS during LIG due to the absence of CDW variability records in the high-latitude SO.

Assemblages of polycystine radiolarians (hereafter, radiolarians), which are a group of planktonic microorganisms (Protista) found in oceans worldwide, are closely linked to the water masses in the SO (Chapter 2 and Abelmann and Gowing, 1996), making them a potential proxy

for assessing the strength of the CDW inflow. In this study, I reconstructed changes in the CDW inflow in the high-latitude SO during the LIG by applying a newly developed index (defined as radiolarian CDW index) to the marine sediment core GC1407 (63.75°S, 130.52°E, 3687 m water depth; Figure 1). This index, which indicates the strength of CDW inflow southward, was derived based on the radiolarian assemblages specifically associated with the CDW and Antarctic Surface Water (AASW). Furthermore, I discuss whether the enhanced CDW inflow cause EAIS mass loss by comparing my data with records of the EAIS behavior (Chapter 1) during the LIG.

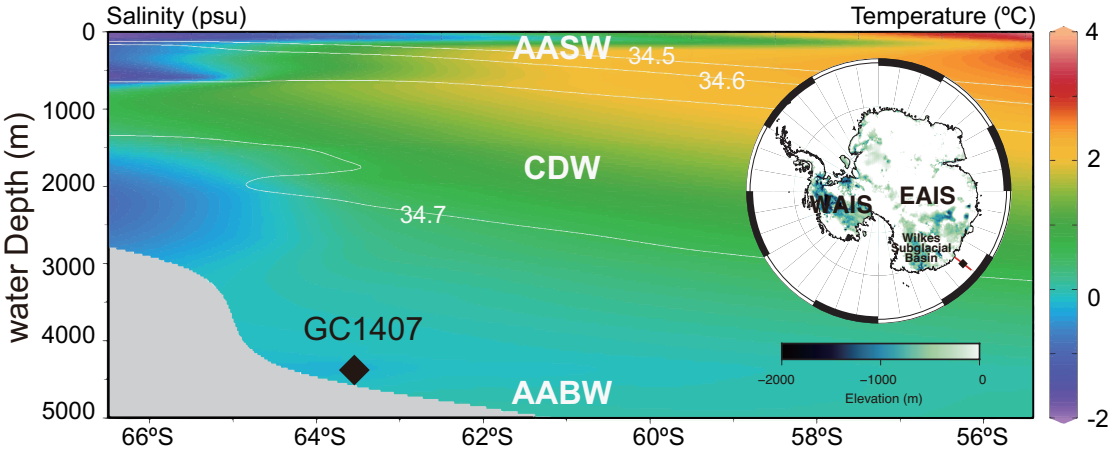


Figure 1 | Vertical section along 130ºE in the South Ocean putting GC1407 into hydrographic context. Color-mapped temperature, with salinity contours overlain, as drawn from the 2018 World Ocean Atlas. GC1407 is marked with a diamond. The inset map indicates the plotted section (red line) and shows subglacial bedrock elevation below sea level (Fretwell et al., 2013). Figure created with Ocean Data View (odv.awi.de).

2. Materials and Methods

2.1 Radiolarian assemblage from core GC1407

Freeze-dried subsamples were weighed (approximately 1–2 g) and then treated with 15% H_2O_2 to remove the organic matter, followed by treatment with HCl solution to remove the calcium carbonate. The samples were then wet sieved (45 μm mesh size), after which two types of permanent slides were made from the residue to quantify the abundance (Q-slide) and for faunal analysis (F-slide) using the method described by Itaki et al. (2018). Briefly, to prepare the Q-slides, all residues were transferred to a 200 mL beaker containing 100 mL of distilled water. The solution was then well mixed, after which a 0.5 mL sample was taken from the suspension using a micropipette and dropped onto a glass slide. The sample was then dried and mounted with Norland optical adhesive. The F-slides were made from the remaining residues in the beaker and then mounted with Norland (NOA61).

Radiolarian skeletons were observed under an optical microscope at magnifications of 100× or 200×, and 400×. The total number of radiolarians contained in 1–2 g of dry sediment (radiolarian concentration, RC) was estimated using the following equation: RC (specimens/g) =total on specimens in Q-slide ×200/sample weight (g). Relative abundance (percent of total assemblage) of radiolarian taxa was estimated by counting and identifying more than 300 specimens on the F-slide; however, when radiolarian individuals were scarce, as many could be identified were counted in the F-slide.

2.2 Age Model

The age models of core GC1407 are described in Chapter 1. Briefly, it is based on the correlation between the *Cylodophora davisiana* abundance in both cores GC1407 and RC11-120 (43.52°S, 79.87°E; 3135 m water depth), and $\delta^{18}O$ of the benthic foraminifera in core RC11-120 and the AICC2012 age mode in the Dome Fuji ice core (77.19ºS 39.40ºE).

2.3 Development of indicator of the CDW strength (radiolarian CDW index)

AASW, CDW, and AABW are distributed at the core GC1407 site, which is located on the continental rise (Figure 1). In general, radiolarian abundance decreases with water depth in the oceans (Boltovskoy, 2017), and radiolarian abundance in AABW, which is found below 4000 m water depth, is particularly scarce. Thus, it is likely that radiolarians preserved in the sediments of core GC1407 are dominated by species that inhabit the CDW and AASW. My data, obtained from surface marine sediment and plankton tow samples south of 60ºS (see Chapter 2), have identified six radiolarian taxa specific to the AASW and nine radiolarian taxa specific to the CDW (Figure 2). Therefore, these radiolarian taxa, which are associated with specific water masses, have the potential to be a tracer of the water masses.

Recent observations show that the southward shift of the PF leads to enhance CDW upwelling with a southward shift of the upwelling area, resulting in a thinning of the AASW layer (Yamazaki et al., 2021). Therefore, there is likely to be a negative relationship between volumes of the AASW and CDW south of the PF. Based on the relationship, I proposed the following radiolarian CDW index, which represents the strength of CDW inflow southward, using the two radiolarian assemblages dwelling in the AASW and CDW:

$$\text{Radiolarian CDW index} = \frac{\text{CDW assemblage}}{\text{AASW assemblage} + \text{CDW assemblage}} \qquad (1)$$

To test the reliability of the radiolarian CDW index, the modern distributions of the radiolarian CDW index were calculated from the radiolarian data set (Chapter 2; Lawler et al., 2021) of surface marine sediments and mapped. The radiolarian CDW index in surface sediments exhibited higher values at lower latitudes (Figure 2), consistent with the observation that the CDW volume increases towards the north. In the vicinity of 50°S, corresponding to the location of the Antarctic Polar Front, the radiolarian CDW indices show low values (Figure 2). The specific low value in

this region could be attributed to a significant change in the water mass structure caused by the transition of the front.

The radiolarian CDW index in the surface sediments ranged between 0.3 and 0.6 in the open ocean south of 60ºS but was around 0.1 on the continental shelf (Figure 2). This result is consistent with observations indicating that intrusion of CDW into the continental shelf is currently limited. Some areas of the continental shelf such as Sabrina coast and Lützow-Holm Bay have higher values of the CDW index (>0.2) (Figure 2), but these areas are characterized by enhanced CDW inflow (e.g., Hirano et al., 2020; Yamazaki et al., 2021). The good agreement between the proxy and observation-based results confirms the reliability of the proposed radiolarian CDW index as a proxy for the strength of CDW in the studied region. In the radiolarian index, an increase in value presumably represents the enhanced southward CDW inflow.

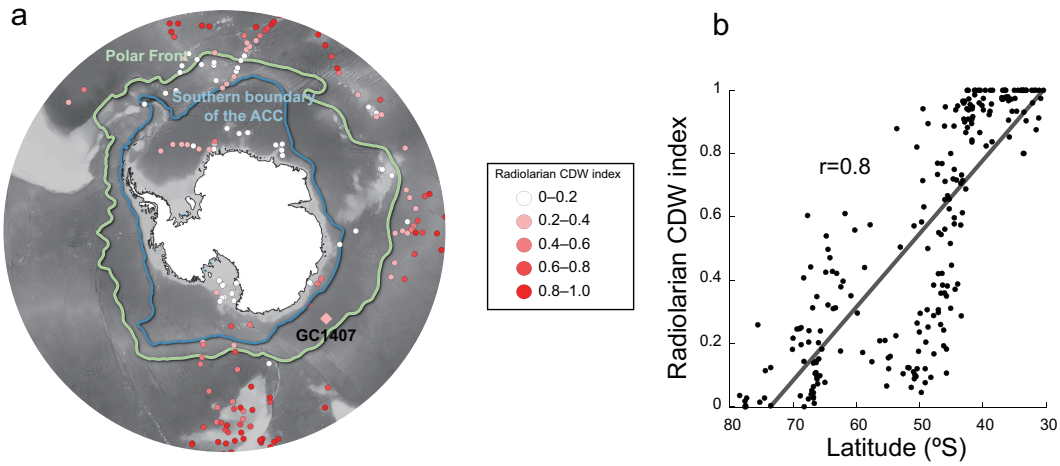


Figure 2 | Radiolarian CDW index in the surface marine sediments. a, The distribution of radiolarian CDW index in surface sediments in the Southern Ocean. **b,** Relationship between radiolarian CDW index in surface sediments and latitude. Map created using the Quantarctica GIS package (Matsuoka et al., 2021) developed by the Norwegian Polar Institute and published under the Creative Commons Attribution 4.0 International License.

3. Results and Discussions

3.1 Influence of strength of CDW to ice mass loss from the WSB

I verified the applicability of the proposed radiolarian CDW index at core GC1407 site, specifically investigating whether there is a negative correlation between the AASW and CDW water masses during the LIG. The results showed that the temporal patterns of the ratio of the radiolarian assemblages dwelling in the AASW and CDW exhibited a negative relationship (R= −0.43) (Figure 3), indicating a close link between the changes in the CDW and AASW during the LIG. Therefore, I concluded that the radiolarian CDW index represents the enhanced CDW index with the stratification of AASW at core site GC1407, indicating the applicability of the new index at this site.

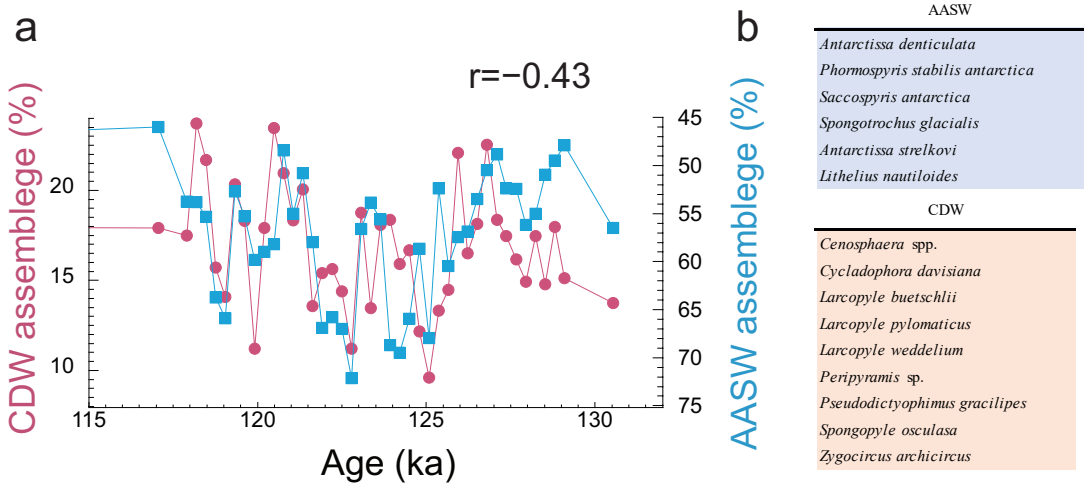


Figure 3 | Relationship between changes in AASW and CDW assemblages. a, The ratios of the CDW and AASW radiolarian assemblages during the LIG. **b,** The radiolarian taxa correspond to each water mass (Chapter 2).

The radiolarian CDW index in core GC1407 during the late Holocene (5–0 ka) ranges from 0.12 to 0.23 with a relatively stable low value (average of 0.19) (Figure 2) compared to the open ocean south of 60ºS (0.3–0.6). This difference is likely attributed to the limited CDW inflow to the continental rise compared to the open ocean (Figure 1). On the other hand, the radiolarian CDW index in the core GC1407 shows significant fluctuations (around 0.1–0.3) with average value of 0.23 during the LIG. Notably, two episodic increases (129–126 ka and 122–120 ka) and a rapid decrease (126–122 ka) are observed in the radiolarian CDW index during the LIG (Figure 4), indicating dynamic changes in CDW strength. These two episodic increases reached values around 0.3 comparable to that of the modern open ocean (>0.3), while the rapid decrease fell to values around 0.1, equivalent to the modern values on the continental shelf (<0.1). These findings indicate that during the two episodic increase events, CDW inflows at the core GC1407 site strengthened, while during the rapid decrease event, the CDW inflows at the core GC1407 site significantly reduced. Hence, the results indicate significant fluctuations in CDW strength throughout the LIG.

Comparison of the ε_{Nd} (an indicator of WSB grounding line retreat) and radiolarian CDW index in the core GC1407 reveals that the increases in ε_{Nd} during both the early and late LIG (Chapter 1) correspond well with the peaks in the radiolarian CDW index (Figure 4). This coincident in both proxies suggests a close relationship between ice mass loss from the WSB and enhanced CDW inflow to the continental rise. Presently, iceberg calving is a significant contributor to ice mass loss from the WSB. However, considering that the WSB ice is a marine-based, it is possible that ice-sheet mass loss during warmer periods such as the LIG (Chapter 1) was influenced by basal melting of the ice shelf due to ocean forcing (such as ocean warming and/or enhanced CDW inflow) (Fretwell et al., 2013).

During the early LIG, the core GC1407 record shows notable peaks in iceberg rafted debris (IBRD; weight percent of grains of 250 μm–2 mm diameter), which is an indicator of iceberg calving and melting. In contrast, the $^{10}Be/^{9}Be$ record in the core GC1407, which provides an indicator of ice-sheet melting, shows a slight increase at this time (Figure 4). Additionally, the ε_{Nd} record in the core GC1407 exhibits a peak at the same time. These findings suggest that ice-sheet shrinkage was primarily due to iceberg calving, with limited basal melting and grounding line retreat (Chapter 1). Furthermore, ice core records of air temperature (Jouzel et al., 2013) show rapid increases during the early LIG, and my records also indicate a rapid increase in CDW inflow at the same time (Figure 4). These results indicate that both rapid increases in air temperature and enhanced CDW inflow contributed to significant iceberg calving and small-scale ice-shelf basal melting.

On the other hand, during the late LIG, notable increases in ε_{Nd} and $^{10}Be/^{9}Be$ were observed, while there were no significant events of iceberg rafted debris (IBRD). This suggests that ice-shelf basal melting may have played a relatively more important role than iceberg calving in the loss of ice mass from the WSB (Chapter 1). The record of the radiolarian CDW index consistently shows a relatively high average value, corresponding to the occurrence of basal melt and grounding line retreat in the WSB indicated by εNd and $^{10}Be/^{9}Be$ during the late LIG (Figure 4). Therefore, the substantial basal melting and retreat of the grounding line in the WSB are closely associated with the persistent enhanced inflow of CDW during the late LIG. Furthermore, the intensity of ice-sheet basal melting was more pronounced during the late LIG (122–118 ka) compared to the early LIG (129–126 ka), potentially due to the prolonged duration of the enhanced CDW inflow. Given the decreasing trend in air temperatures during the late LIG, it is possible that even without an increase in air temperatures, the inflow of CDW alone could lead to significant ice sheet attrition in the WSB.

3.2 Causes of the strength of the CDW inflow in the Indian Ocean

Recent oceanographic observations between 1930 and 2018 suggest that the southward shift of the ACC's southern boundary in the Indian Ocean has resulted in the enhanced southward CDW inflow, leading to the EAIS melting (Herraiz-Borreguero et al., 2022). The southward shift of the ACC's southern boundary also contributes to an increase in SST in the vicinity of the boundary (Herraiz-Borreguero et al., 2022). Although direct evidence of the southward shift of the ACC's southern boundary is limited during the LIG, diatom assemblage records from marine sediment cores collected in the Indian Ocean suggest an increase in SST during the LIG near the ACC's southern boundary due to the southward shift of ACC (Chadwick et al., 2022). Additionally, other SST records near the ACC's southern boundary show remarkable increases during both the early and late stages of the LIG (Crosta et al., 2020; Crosta et al., 2004) (Figure 5). The two episodic increases in SST during the early and late LIG coincide with the timing of enhanced CDW inflow (Figure 5). Therefore, the increase in SST could have been caused by the southward shift of boundary during the early and late LIG periods, and it may cause enhanced CDW inflow into the continental rise.

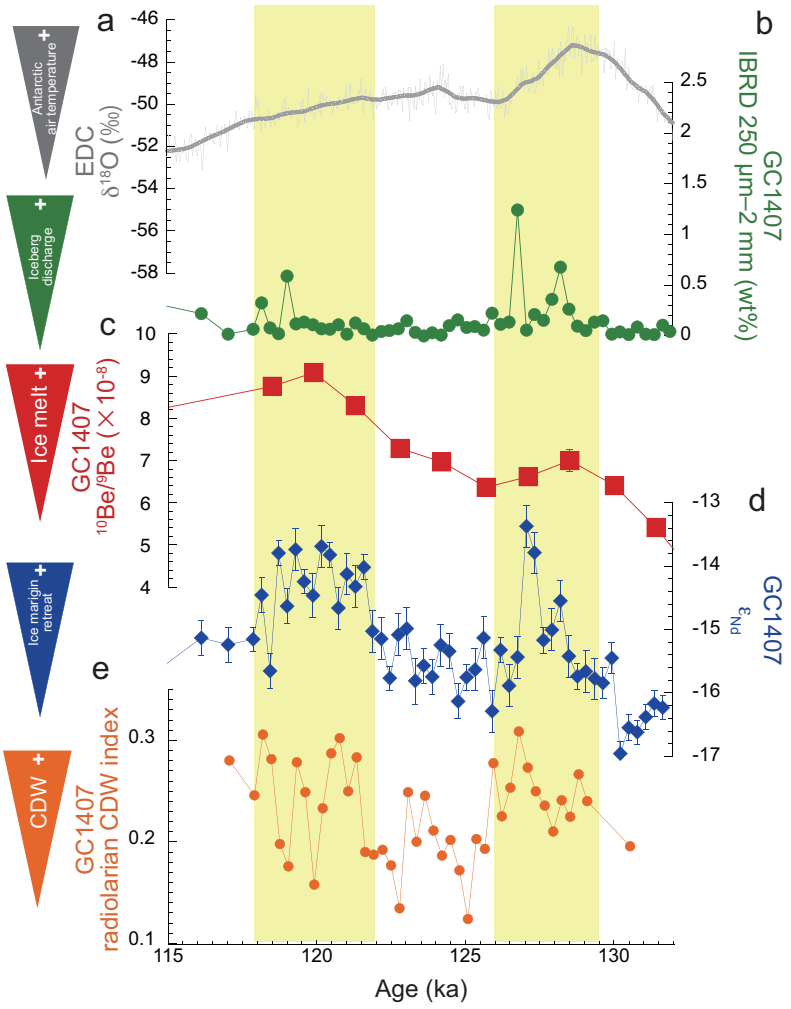


Figure 4 | Paleoclimate records during the LIG. a, $\delta^{18}O$ record from EPICA Dome C (EDC) ice core (thin and bold gray lines are the raw signals and weighted smoothing, respectively) (grey line) (Masson-Delmotte et al., 2013). **B,** Iceberg rafted debris (IBRD, percent 250 µm–2 mm) from core GC1407 (green circles, this study). **c,** Authigenic $^{10}Be/^{9}Be$ ratios from core GC1407 (red squares, this study) (error bars are 1 s.d.). **d,** Detrital sediment Nd isotopes (ε_{Nd}) from core GC1407 (dark blue diamonds, this study) (error bars are 2 s.d.). **e,** Radiolarian CDW index from core GC1407 (orange circles, this study). Yellow bars indicate two episodes of inferred increased radiolarian CDW index during the early and late Last Interglacial.

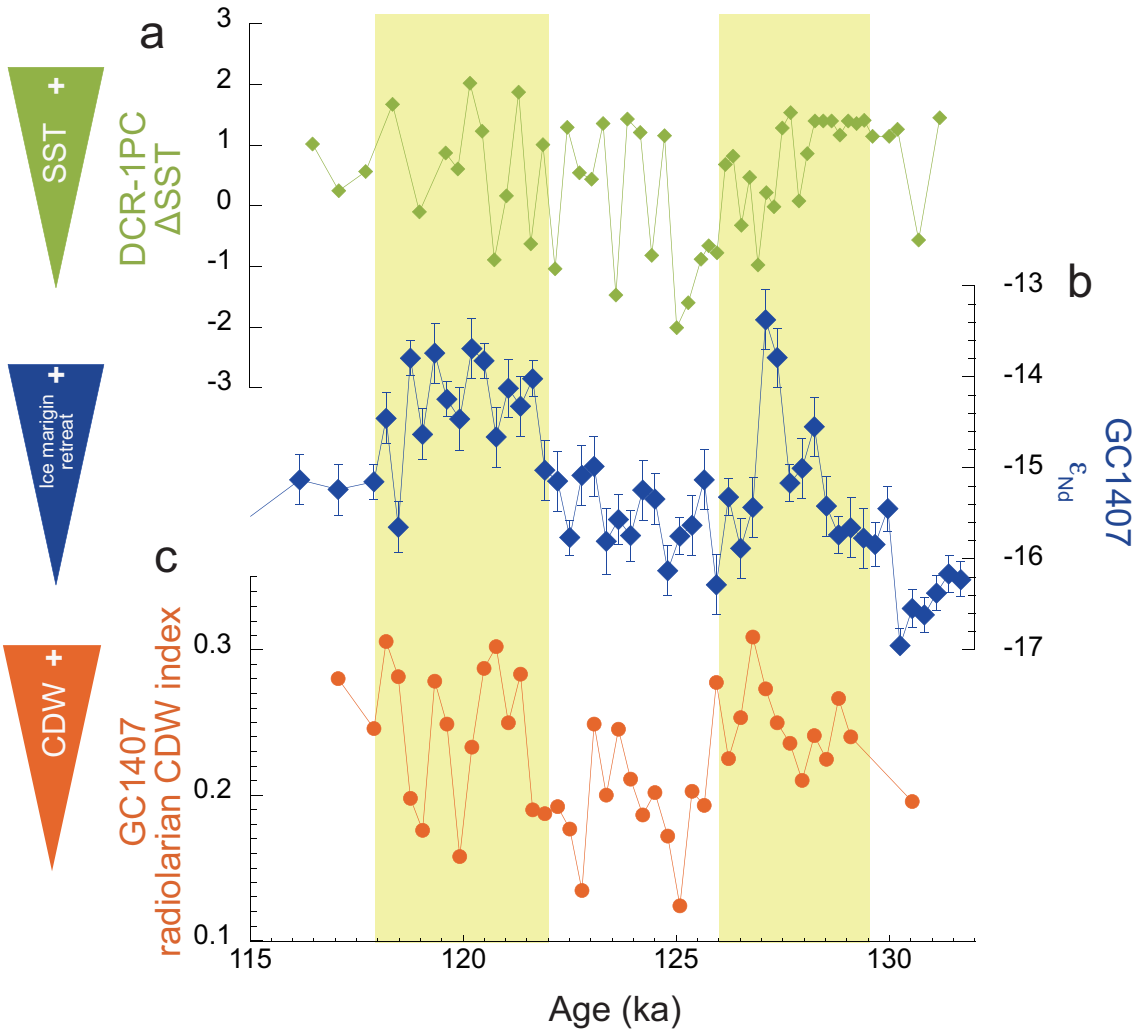


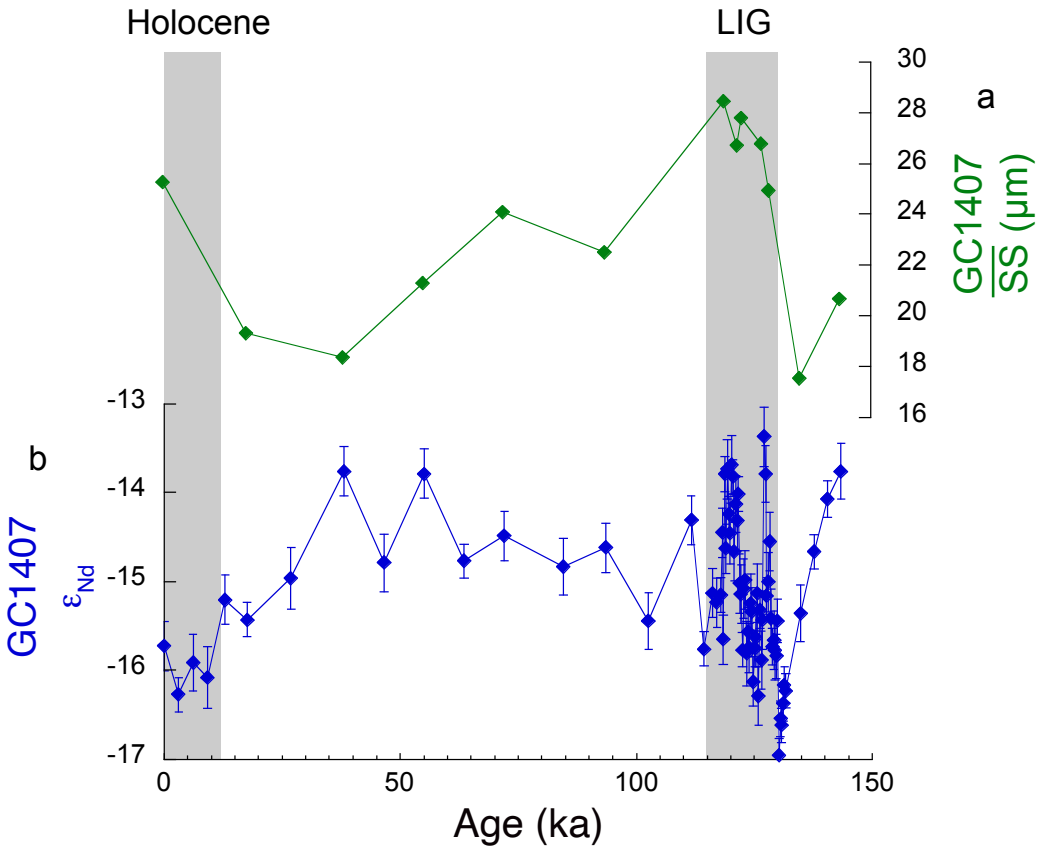
Figure 5 | Comparison of core GC1407 records to sea surface temperature in the Southern Ocean during the LIG. a, Southern Ocean sea surface temperature (SST) from diatom assemblages in core DCR-1PC (light green diamonds) (Crosta et al., 2020). **b,** Detrital sediment Nd isotopes (ε_{Nd}) from core GC1407 (dark blue diamonds, this study) (error bars are 2 s.d.). **c,** Radiolarian CDW index from core GC1407 (orange circles, this study). Yellow bars indicate two episodes of inferred increased radiolarian CDW index during the early and late Last Interglacial.

4. Conclusion and Perspectives

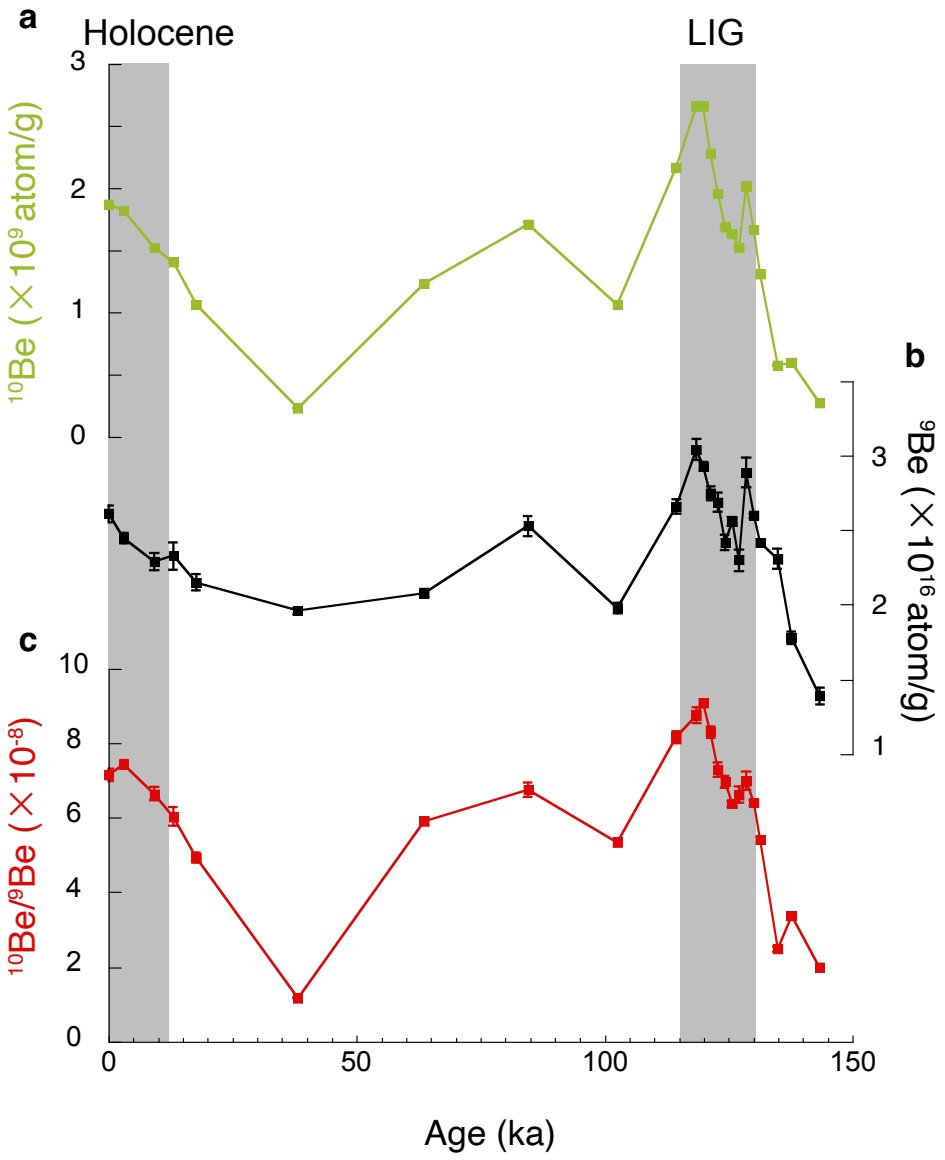
In this study, I proposed the radiolarian CDW index as a measure of the strength of CDW inflow. The radiolarian CDW index was validated using radiolarian data from modern surface sediments and was shown to represent the variations in CDW strength. Furthermore, I applied the radiolarian CDW index to sediment core GC1407 to investigate the relationship between CDW strength fluctuations and ice mass loss during the LIG. The results revealed a close correspondence between CDW strength and ice mass variations. Additionally, comparisons of my data with other paleoclimate records support the notion that the southward shift of the ACC's boundary in the Indian Ocean has led to enhanced CDW inflow, resulting in significant ice melting from the WSB during the LIG. Such a result offers valuable insights into the future dynamics of the EAIS and the high-latitude Southern Ocean.

My findings suggest that in the event of a potential southward shift of the ACC's boundary in the future, the ice sheet in the WSB region could undergo substantial retreat. To gain deeper insights into the mechanisms driving changes in the ACC's boundary, a more comprehensive dataset of paleoclimate information from the LIG is needed.

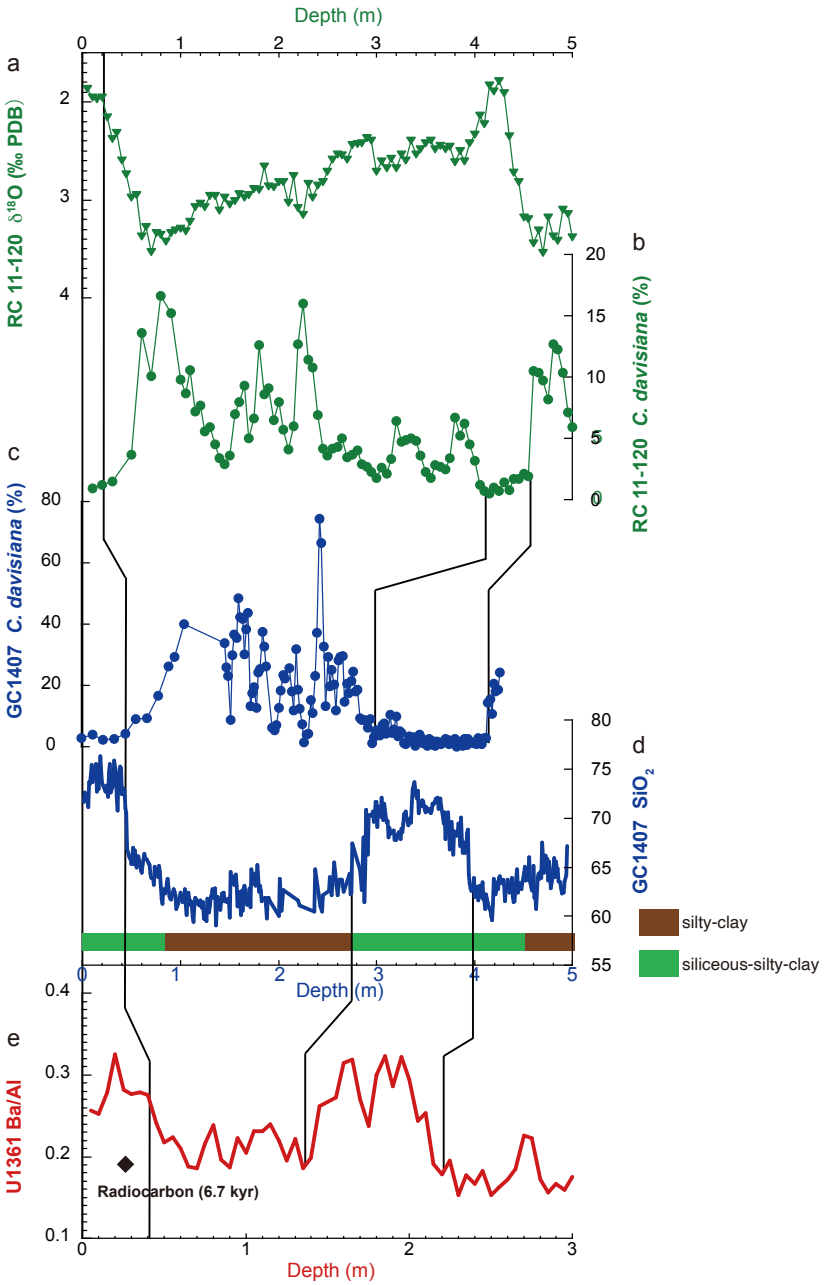
Supplementary data for Chapter 1



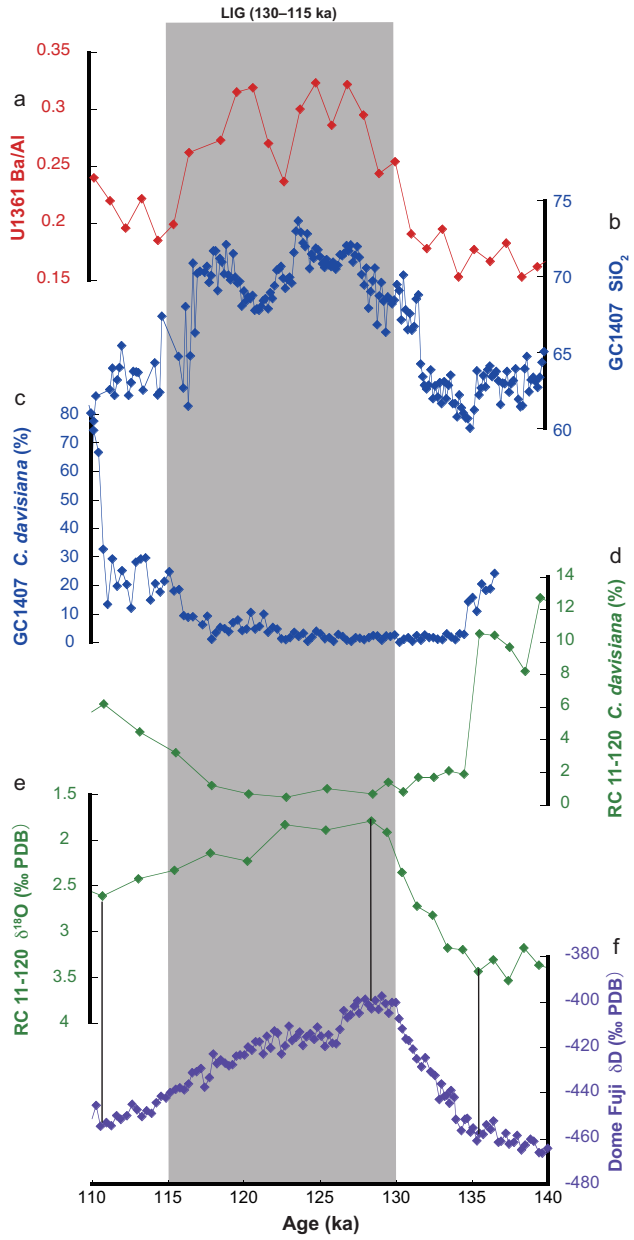
Supplementary Figure 1 | Grain-size analysis in core GC1407 from the Last Interglacial to the Holocene a, Mean grain size of the sortable silt fraction ($\overline{SS}$: 10–63 μm) in core GC1407 (green diamonds). **b**, Detrital sediment Nd isotopes (ε_{Nd}) in core GC1407 (blue diamonds) (error bars are 2 s.d.). Grey bars highlight the Holocene (11–0 ka) and Last Interglacial (LIG; 130–115 ka) intervals.



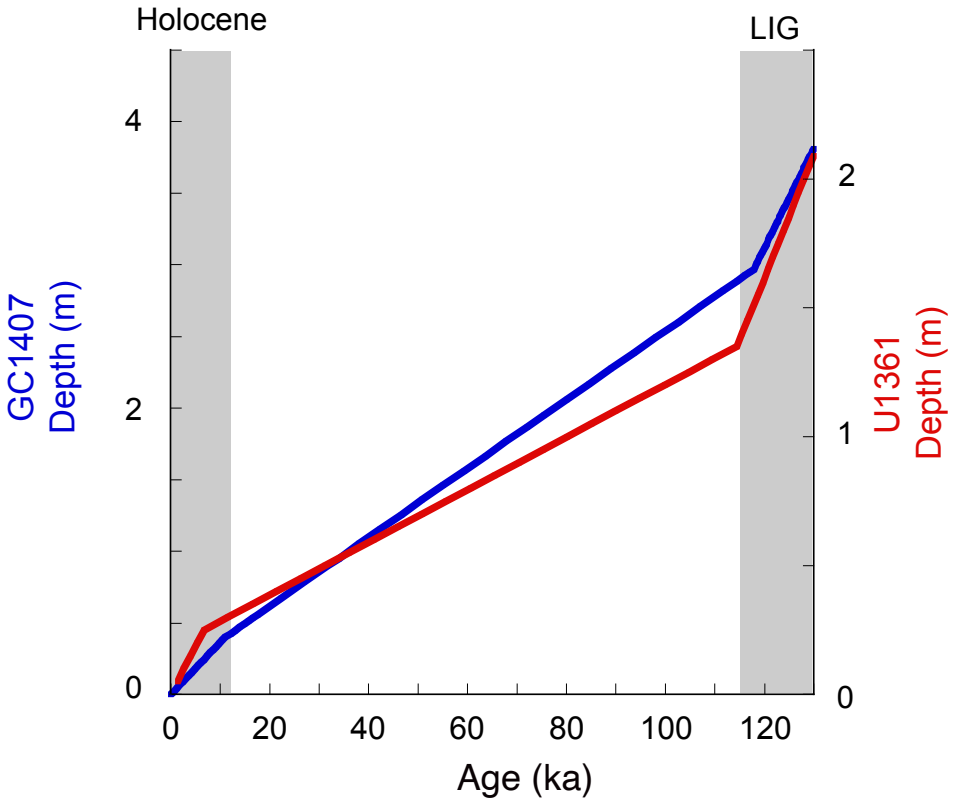
Supplementary Figure 2 | Authigenic Be isotope records in core GC1407 from the Last Interglacial to the Holocene. **a**, ^{10}Be record (light green squares). **b**, ^{9}Be record (black squares). **c**, ^{10}Be/^{9}Be record (red squares) (error bars are 1 s.d.). Grey bars highlight the Holocene (11–0 ka) and Last Interglacial (LIG; 130–115 ka) intervals.



Supplementary Figure 3 | Chronological constraints from the Last Interglacial to the Holocene. a and **b**, Planktonic foraminifera (*Globigerina bulloides*) $\delta^{18}O$ and *C. davisiana* abundance in core RC11-120 (Hays et al., 1976) (green triangles and dots). **c** and **d**, *C. davisiana* abundance and SiO_2 content with lithological log in core GC1407 (blue dots and line). **e**, Ba/Al ratios (from XRF core-scanning) in core U1361A (red line), and radiocarbon age indicated by black diamond (Wilson et al., 2018). Vertical lines indicate tie points.



Supplementary Figure 4 | Transferring marine sediment cores onto the AICC2012 chronology during the Last Interglacial. a, Ba/Al ratios (from XRF core-scanning) in core U1361A (Wilson et al., 2018) (red symbols and line). **b** and **c**, SiO_2 content and *C. davisiana* abundance in core GC1407 (blue symbols and lines). **d** and **e**, *C. davisiana* abundance and planktonic foraminiferal $\delta^{18}O$ in core RC11-120 (Howard et al., 1992; Martinson et al., 1987; Hays et al., 1976) (green symbols and lines). **f**, dD in Dome Fuji ice core (Uemura et al., 2012) (purple symbols and line). Vertical lines indicate tie points. Grey bar highlights the Last Interglacial (LIG; 130–115 ka).



Supplementary Figure 5 | Depth-age models in cores GC1407 and U1361A. Depth versus age plot showing sedimentation rates in cores GC1407 (blue line) and U1361A (red line) (Wilson et al., 2018). Grey bars highlight the Holocene (11–0 ka) and Last Interglacial (LIG; 130–115 ka) intervals.

Supplementary Table 1 | Chronostratigraphy in the GC1407, RC11-120, and U1361.

RC11-120

Depth (m)	Age (ka)
0.65	17
3.79	108.1
4.24	129
4.59	135.2

GC1407

Depth (m)	Age (ka)
0.4	11
2.97	117.9
4.13	134.9

U1361

Depth (m)	Age (ka)
0.4	11.6
1.35	114.5
2.2	132.2

Supplementary Table 2 | Neodymium isotopes in the GC1407

Top depth (mbsf cm)	Age (kyr)	$^{143}Nd/^{144}Nd$	± 2 S.E.	e_{Nd}	± 2 S.D.
0	0.0	0.511830	0.000010	-15.76	0.28
11	3.1	0.511804	0.000008	-16.27	0.19
22	n.d.	0.511822	0.000011	-15.92	0.32
34	n.d.	0.511813	0.000009	-16.08	0.35
45	n.d.	0.511856	0.000009	-15.25	0.28
56	n.d.	0.511847	0.000008	-15.43	0.19
80	n.d.	0.511871	0.000010	-14.96	0.35
105	n.d.	0.511928	0.000008	-13.84	0.28
126	n.d.	0.511880	0.000009	-14.79	0.32
146	n.d.	0.511929	0.000009	-13.82	0.28
166	n.d.	0.511881	0.000007	-14.77	0.19
187	n.d.	0.511892	0.000008	-14.56	0.28
217	n.d.	0.511877	0.000010	-14.84	0.32
238	n.d.	0.511892	0.000010	-14.55	0.28
260	n.d.	0.511846	0.000010	-15.45	0.32
282	n.d.	0.511904	0.000010	-14.32	0.28
288	n.d.	0.511830	0.000008	-15.76	0.19
293	n.d.	0.511867	0.000011	-15.04	0.28
295	n.d.	0.511861	0.000010	-15.16	0.28
297	117.9	0.511861	0.000009	-15.15	0.19
299	118.2	0.511897	0.000012	-14.46	0.28
301	118.5	0.511831	0.000011	-15.73	0.28
303	118.8	0.511931	0.000008	-13.79	0.19
305	119.0	0.511889	0.000008	-14.62	0.28
307	119.3	0.511927	0.000010	-13.87	0.33
309	119.6	0.511908	0.000008	-14.24	0.19
311	119.9	0.511897	0.000010	-14.46	0.35
313	120.2	0.511929	0.000007	-13.84	0.33
315	120.5	0.511929	0.000007	-13.82	0.19
317	120.8	0.511877	0.000008	-14.85	0.33
319	121.1	0.511914	0.000009	-14.12	0.32
321	121.3	0.511894	0.000009	-14.52	0.33
323	121.6	0.511919	0.000009	-14.02	0.19
325	121.9	0.511868	0.000009	-15.02	0.33
327	122.2	0.511860	0.000010	-15.18	0.33
329	122.5	0.511830	0.000008	-15.77	0.19
331	122.8	0.511855	0.000007	-15.28	0.33
333	123.1	0.511868	0.000009	-15.02	0.33
335	123.4	0.511824	0.000010	-15.87	0.28
337	123.6	0.511846	0.000009	-15.44	0.28
339	123.9	0.511834	0.000006	-15.69	0.28
341	124.2	0.511858	0.000010	-15.22	0.33
343	124.5	0.511854	0.000011	-15.30	0.28

345	124.8	0.511819	0.000009	-15.97	0.28
347	125.1	0.511831	0.000008	-15.75	0.20
349	125.4	0.511836	0.000009	-15.64	0.33
351	125.7	0.511865	0.000008	-15.09	0.33
353	125.9	0.511805	0.000010	-16.24	0.33
355	126.2	0.511852	0.000008	-15.32	0.20
357	126.5	0.511829	0.000009	-15.79	0.33
359	126.8	0.511848	0.000009	-15.40	0.33
361	127.1	0.511954	0.000008	-13.33	0.33
363	127.4	0.511931	0.000009	-13.79	0.32
365	127.7	0.511861	0.000008	-15.16	0.20
367	127.9	0.511875	0.000007	-14.88	0.33
369	128.2	0.511901	0.000008	-14.38	0.33
371	128.5	0.511854	0.000009	-15.30	0.33
373	128.8	0.511831	0.000009	-15.74	0.20
375	129.1	0.511846	0.000008	-15.45	0.33
377	129.4	0.511846	0.000010	-15.44	0.33
379	129.7	0.511819	0.000009	-15.98	0.25
381	130.0	0.511836	0.000011	-15.65	0.25
383	130.2	0.511773	0.000011	-16.87	0.21
385	130.5	0.511790	0.000009	-16.55	0.20
387	130.8	0.511787	0.000010	-16.61	0.21
389	131.1	0.511798	0.000011	-16.38	0.21
391	131.4	0.511809	0.000009	-16.17	0.20
393	131.7	0.511803	0.000008	-16.28	0.21
415	134.8	0.511851	0.000010	-15.36	0.32
435	137.6	0.511881	0.000009	-14.76	0.21
455	140.5	0.511917	0.000009	-14.07	0.20
475	143.4	0.511939	0.000009	-13.64	0.43

Supplementary Table 3 | Beryllium isotopes in the GC1407

Top depth (mbsf cm)	Age (kyr)	Decaly corr. 10Be conc (atom/g)	10Be-STD (1σ)/g	9Besample (atom/g) _ICP-MS	9Be-STD_ICP-MS	Authigenic 10Be/9Be _ICP-MS	STD (1σ)_ ICP-MS
0	0.0	1.87E+09	1.2E+07	2.61E+16	5.66E+14	7.16	0.16
11	3.1	1.82E+09	1.2E+07	2.45E+16	3.64E+14	7.43	0.12
34	n.d.	1.52E+09	9410375	2.29E+16	5.96E+14	6.65	0.18
45	n.d.	1.41E+09	1.1E+07	2.33E+16	9.06E+14	6.04	0.24
56	n.d.	1.06E+09	7500151	2.15E+16	5.58E+14	4.93	0.13
105	n.d.	2.31E+08	2726471	1.96E+16	2.19E+14	1.18	0.02
166	n.d.	1.23E+09	9048699	2.08E+16	2.56E+14	5.91	0.08
217	n.d.	1.71E+09	1.3E+07	2.53E+16	6.79E+14	6.75	0.19
260	n.d.	1.06E+09	7918594	1.98E+16	3.47E+14	5.35	0.10
288	n.d.	2.17E+09	1.6E+07	2.66E+16	4.89E+14	8.17	0.16
301	118.5	2.66E+09	1.8E+07	3.04E+16	7.02E+14	8.75	0.21
311	119.9	2.66E+09	1.8E+07	2.93E+16	2.67E+14	9.08	0.10
321	121.3	2.28E+09	1.9E+07	2.75E+16	4.62E+14	8.30	0.16
331	122.8	1.96E+09	1.8E+07	2.69E+16	6.39E+14	7.29	0.19
341	124.2	1.69E+09	1.3E+07	2.42E+16	5.5E+14	6.97	0.17
351	125.7	1.63E+09	1.3E+07	2.56E+16	2.96E+14	6.37	0.09
361	127.1	1.52E+09	1.5E+07	2.3E+16	7.39E+14	6.62	0.22
371	128.5	2.02E+09	1.6E+07	2.89E+16	1.01E+15	7.00	0.25
381	130.0	1.67E+09	1.7E+07	2.6E+16	1.37E+14	6.41	0.07
391	131.4	1.31E+09	1.3E+07	2.42E+16	1.45E+14	5.42	0.06
415	134.8	5.76E+08	5423241	2.31E+16	6.77E+14	2.49	0.08
435	137.6	5.99E+08	5748977	1.78E+16	4.15E+14	3.37	0.09
475	143.4	2.76E+08	2870258	1.39E+16	5.6E+14	1.99	0.08

Supplementary Table 4 | Grain size in the GC1407

Top depth (mbsf cm)	Age (kyr)	IBRD (wt% 250 µm-2 mm)	Sortable Silt (µm)
0	0.0	0.11	25.28
11	3.1	0.05	
22	n.d.	0.10	
34	n.d.	0.19	
45	n.d.	0.04	
56	n.d.	0.17	19.33
67	n.d.	0.09	
78	n.d.	0.03	
89	n.d.	0.03	
95	n.d.	0.01	
105	n.d.	0.00	18.38
115	n.d.	0.15	
126	n.d.	1.63	
136	n.d.	0.04	
146	n.d.	0.47	21.28
156	n.d.	0.02	
166	n.d.	0.03	
177	n.d.	0.02	
187	n.d.	0.04	24.09
195	n.d.	0.08	
206	n.d.	0.08	
217	n.d.	0.02	
228	n.d.	0.00	
238	n.d.	0.19	22.51
249	n.d.	0.00	
260	n.d.	0.46	
271	n.d.	0.08	
282	n.d.	0.13	
288	n.d.	0.34	
293	n.d.	0.22	
295	n.d.	0.02	
297	117.9	0.07	
299	118.2	0.33	
301	118.5	0.08	
303	118.8	0.02	28.45
305	119.0	0.59	
307	119.3	0.12	
309	119.6	0.14	
311	119.9	0.11	
313	120.2	0.07	
315	120.5	0.07	
317	120.8	0.11	
319	121.1	0.02	
321	121.3	0.13	

323	121.6	0.07	26.72
325	121.9	0.01	
327	122.2	0.04	
329	122.5	0.05	27.79
331	122.8	0.07	
333	123.1	0.15	
335	123.4	0.04	
337	123.6	0.00	
339	123.9	0.03	
341	124.2	0.01	
343	124.5	0.10	
345	124.8	0.16	
347	125.1	0.08	
349	125.4	0.09	
351	125.7	0.06	
353	125.9	0.22	
355	126.2	0.12	
357	126.5	0.14	
359	126.8	1.24	26.79
361	127.1	0.06	
363	127.4	0.21	
365	127.7	0.15	
367	127.9	0.36	
369	128.2	0.68	24.93
371	128.5	0.26	
373	128.8	0.10	
375	129.1	0.05	
377	129.4	0.14	
379	129.7	0.15	
381	130.0	0.02	
383	130.2	0.04	
385	130.5	0.01	
387	130.8	0.09	
389	131.1	0.02	
391	131.4	0.01	
393	131.7	0.11	
395	131.9	0.04	
397	132.2	0.15	
399	132.5	0.21	
401	132.8	0.08	
403	133.1	0.07	
405	133.4	0.04	
407	133.6	0.12	
409	133.9	0.00	
415	134.8	0.04	17.55
425	136.2	0.02	

433	137.4	0.03	
443	138.8	0.02	
455	140.5	0.00	
465	141.9	0.03	
475	143.4	0.03	20.67
485	144.8	0.05	

Supplementary Table 5 | *C. davisiana* relative abundance in the GC1407

Top depth (mbsf cm)	Age (kyr)	*C. davisiana* relative abundance (%)
0	0.0	2.89
11	3.1	3.93
22	n.d.	2.31
34	n.d.	2.66
45	n.d.	4.30
56	n.d.	8.97
67	n.d.	9.30
78	n.d.	16.61
89	n.d.	26.14
95	n.d.	29.41
105	n.d.	40.00
146	n.d.	33.97
148	n.d.	25.88
150	n.d.	23.08
152	n.d.	8.76
154	n.d.	29.82
156	n.d.	36.81
158	n.d.	35.50
160	n.d.	48.46
162	n.d.	42.34
164	n.d.	41.83
166	n.d.	30.13
168	n.d.	38.46
171	n.d.	43.81
173	n.d.	13.21
175	n.d.	17.62
177	n.d.	19.47
179	n.d.	12.73
181	n.d.	24.36
183	n.d.	25.48
185	n.d.	37.62
187	n.d.	32.69
189	n.d.	26.21
195	n.d.	6.36
197	n.d.	5.31
199	n.d.	7.21
202	n.d.	12.86
204	n.d.	18.32
206	n.d.	23.38
208	n.d.	22.45
212	n.d.	25.78
215	n.d.	18.22
217	n.d.	11.88
219	n.d.	32.00

221	n.d.	18.52
223	n.d.	12.38
225	n.d.	7.28
228	n.d.	1.56
230	n.d.	3.94
232	n.d.	4.35
234	n.d.	15.26
236	n.d.	10.96
238	n.d.	23.15
241	n.d.	37.24
243	n.d.	74.37
245	n.d.	66.67
247	n.d.	32.64
249	n.d.	13.33
252	n.d.	29.25
254	n.d.	19.74
256	n.d.	25.16
258	n.d.	20.34
260	n.d.	12.00
262	n.d.	28.23
265	n.d.	29.33
267	n.d.	29.70
269	n.d.	14.83
271	n.d.	20.60
273	n.d.	17.55
275	n.d.	21.33
278	n.d.	24.70
280	n.d.	18.01
282	n.d.	18.61
284	n.d.	9.41
286	n.d.	8.85
288	n.d.	8.91
293	n.d.	6.25
295	n.d.	9.12
297	117.9	1.14
299	118.2	3.26
301	118.5	5.31
303	118.8	4.92
305	119.0	3.75
307	119.3	6.98
309	119.6	7.78
311	119.9	4.14
313	120.2	4.72
315	120.5	10.44
317	120.8	4.59
319	121.1	5.64

321	121.3	9.97
323	121.6	3.56
325	121.9	5.19
327	122.2	4.62
329	122.5	1.25
331	122.8	0.94
333	123.1	1.70
335	123.4	3.50
337	123.6	1.95
339	123.9	3.24
341	124.2	0.31
343	124.5	1.92
345	124.8	3.89
347	125.1	2.89
349	125.4	1.28
351	125.7	1.72
353	125.9	0.32
355	126.2	2.72
357	126.5	2.13
359	126.8	0.65
361	127.1	0.32
363	127.4	1.64
365	127.7	1.50
367	127.9	0.98
369	128.2	1.59
371	128.5	2.48
373	128.8	2.22
375	129.1	0.78
377	129.4	2.15
379	129.7	2.01
381	130.0	2.53
383	130.2	0.00
385	130.5	1.05
387	130.8	1.62
389	131.1	0.32
391	131.4	2.48
393	131.7	0.64
395	131.9	2.64
397	132.2	1.59
399	132.5	1.59
401	132.8	1.17
403	133.1	0.98
405	133.4	2.99
407	133.6	1.90
409	133.9	0.98
411	134.2	2.98

413	134.5	2.81
415	134.8	14.29
417	135.1	15.66
419	135.4	10.77
421	135.6	20.48
423	135.9	18.13
425	136.2	18.75
427	136.5	24.24

Supplementary Table 6 | SiO_2 contents in the GC1407

Top depth (mbsf cm)	Age (kyr)	SiO2(ms%)
1	0.3	71.68
2	0.6	72.62
3	0.9	72.29
4	1.2	72.28
6	1.5	71.11
7	1.8	73.69
8	2.2	73.53
9	2.5	75.45
10	2.8	73.71
13	n.d.	75.50
15	n.d.	72.71
16	n.d.	74.16
17	n.d.	73.01
18	n.d.	76.31
19	n.d.	74.75
20	n.d.	73.61
23	n.d.	72.75
25	n.d.	73.36
26	n.d.	72.20
27	n.d.	74.61
28	n.d.	75.53
29	n.d.	72.64
30	n.d.	73.12
31	n.d.	73.31
32	n.d.	75.89
34	n.d.	74.64
35	n.d.	72.13
36	n.d.	70.78
37	n.d.	74.22
38	n.d.	75.23
39	n.d.	75.12
40	n.d.	72.44
41	n.d.	73.04
42	n.d.	72.89
44	n.d.	71.06
45	n.d.	70.53
46	n.d.	66.90
47	n.d.	66.24
48	n.d.	65.91
49	n.d.	65.94
50	n.d.	65.32
51	n.d.	66.97
53	n.d.	65.33
54	n.d.	66.75

55	n.d.	64.94
56	n.d.	66.07
57	n.d.	66.08
58	n.d.	65.65
59	n.d.	64.70
60	n.d.	64.45
61	n.d.	65.31
63	n.d.	66.37
64	n.d.	65.92
65	n.d.	65.87
66	n.d.	65.79
67	n.d.	65.44
68	n.d.	65.25
69	n.d.	64.35
70	n.d.	63.89
72	n.d.	63.90
73	n.d.	63.18
74	n.d.	65.09
75	n.d.	64.26
76	n.d.	64.60
77	n.d.	64.00
78	n.d.	65.18
79	n.d.	64.54
80	n.d.	61.76
82	n.d.	61.26
83	n.d.	62.75
84	n.d.	62.30
85	n.d.	62.50
86	n.d.	63.34
87	n.d.	63.82
88	n.d.	62.07
89	n.d.	61.80
91	n.d.	61.69
92	n.d.	62.40
93	n.d.	62.75
94	n.d.	62.50
95	n.d.	62.18
96	n.d.	60.76
97	n.d.	61.29
98	n.d.	61.78
99	n.d.	61.95
100	n.d.	62.45
101	n.d.	61.99
102	n.d.	61.46
103	n.d.	61.57
104	n.d.	62.80

105	n.d.	61.16
106	n.d.	60.13
107	n.d.	61.79
108	n.d.	62.38
109	n.d.	61.18
110	n.d.	61.56
111	n.d.	61.07
112	n.d.	59.93
113	n.d.	59.42
114	n.d.	61.21
115	n.d.	61.86
116	n.d.	61.62
117	n.d.	61.30
118	n.d.	61.16
119	n.d.	61.10
121	n.d.	61.59
122	n.d.	60.82
123	n.d.	61.46
124	n.d.	59.73
125	n.d.	59.70
126	n.d.	60.26
127	n.d.	59.50
128	n.d.	61.80
129	n.d.	60.37
130	n.d.	61.09
131	n.d.	61.96
132	n.d.	62.15
133	n.d.	62.72
134	n.d.	61.91
135	n.d.	62.81
136	n.d.	59.04
137	n.d.	60.80
138	n.d.	62.00
139	n.d.	61.21
140	n.d.	61.57
141	n.d.	60.67
142	n.d.	62.30
143	n.d.	62.34
144	n.d.	62.40
145	n.d.	61.56
146	n.d.	61.56
147	n.d.	61.41
148	n.d.	61.78
149	n.d.	61.50
150	n.d.	59.83
151	n.d.	64.49

152	n.d.	63.38
153	n.d.	64.10
154	n.d.	63.20
155	n.d.	63.70
156	n.d.	64.24
157	n.d.	63.09
158	n.d.	61.00
159	n.d.	62.51
160	n.d.	61.83
161	n.d.	60.16
162	n.d.	62.58
163	n.d.	60.56
164	n.d.	62.80
165	n.d.	63.14
166	n.d.	62.65
167	n.d.	61.16
168	n.d.	61.15
169	n.d.	62.26
171	n.d.	62.84
172	n.d.	60.89
173	n.d.	64.80
174	n.d.	63.30
175	n.d.	63.59
176	n.d.	64.31
177	n.d.	63.11
178	n.d.	63.84
179	n.d.	65.23
180	n.d.	62.52
181	n.d.	63.07
182	n.d.	62.58
183	n.d.	61.55
184	n.d.	61.76
185	n.d.	61.75
186	n.d.	61.87
187	n.d.	61.13
188	n.d.	59.76
189	n.d.	61.84
190	n.d.	61.86
191	n.d.	61.59
200	n.d.	60.04
202	n.d.	63.86
203	n.d.	60.55
205	n.d.	62.67
220	n.d.	61.61
221	n.d.	61.06
236	n.d.	60.50

237	n.d.	64.75
241	n.d.	62.22
243	n.d.	61.03
244	n.d.	60.47
245	n.d.	62.16
252	n.d.	62.56
253	n.d.	63.96
254	n.d.	62.17
255	n.d.	63.21
256	n.d.	64.00
257	n.d.	65.46
260	n.d.	62.19
261	n.d.	63.03
262	n.d.	63.78
263	n.d.	63.72
265	n.d.	63.69
267	n.d.	62.54
272	n.d.	64.33
273	n.d.	62.21
274	n.d.	62.39
275	n.d.	67.40
283	n.d.	64.74
285	n.d.	62.66
286	n.d.	68.02
287	n.d.	61.47
288	n.d.	64.80
290	n.d.	70.88
291	n.d.	66.31
292	n.d.	70.21
293	n.d.	70.34
295	n.d.	70.26
296	n.d.	70.65
297	117.9	69.60
298	118.0	70.07
299	118.2	71.67
300	118.3	71.68
301	118.5	69.10
302	118.6	71.18
303	118.8	70.93
304	118.9	70.17
305	119.0	72.09
306	119.2	70.09
307	119.3	69.79
308	119.5	71.52
309	119.6	69.96
310	119.8	69.57

311	119.9	69.69
312	120.1	68.06
313	120.2	69.04
314	120.3	68.36
315	120.5	68.67
316	120.6	68.54
317	120.8	68.75
318	120.9	67.77
319	121.1	67.87
320	121.2	67.79
321	121.3	68.03
322	121.5	68.40
323	121.6	68.57
324	121.8	67.89
325	121.9	68.93
326	122.1	68.55
327	122.2	69.40
328	122.4	70.42
329	122.5	70.47
330	122.6	70.66
331	122.8	69.90
332	122.9	69.24
333	123.1	69.81
334	123.2	69.98
335	123.4	69.58
336	123.5	71.57
337	123.6	72.99
338	123.8	73.64
339	123.9	72.91
340	124.1	72.23
341	124.2	71.97
342	124.4	72.81
343	124.5	70.54
344	124.6	71.46
345	124.8	71.21
346	124.9	71.85
347	125.1	71.76
348	125.2	71.30
349	125.4	70.83
350	125.5	70.58
351	125.7	71.13
352	125.8	70.76
353	125.9	70.68
354	126.1	70.94
355	126.2	70.48
356	126.4	70.75

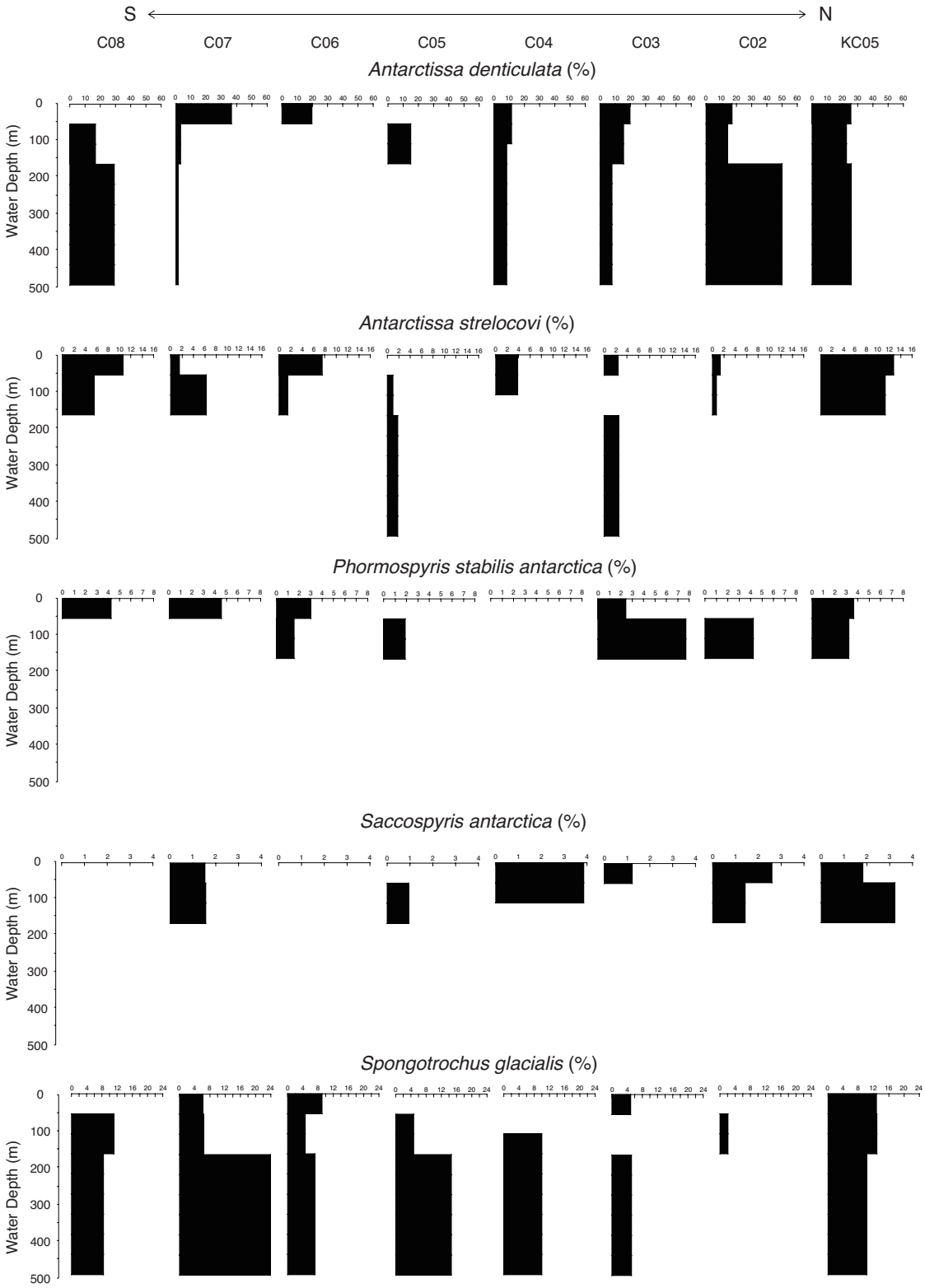
357	126.5	71.44
358	126.7	71.37
359	126.8	71.54
360	126.9	72.03
361	127.1	71.70
362	127.2	72.07
363	127.4	70.96
364	127.5	71.41
365	127.7	71.98
366	127.8	71.25
367	127.9	70.15
368	128.1	69.43
369	128.2	70.57
370	128.4	67.90
371	128.5	69.00
372	128.7	69.71
373	128.8	70.57
374	129.0	66.84
375	129.1	68.74
376	129.2	69.61
377	129.4	68.37
378	129.5	66.32
379	129.7	68.67
380	129.8	68.49
381	130.0	68.21
382	130.1	68.43
383	130.2	69.48
384	130.4	69.09
385	130.5	67.13
386	130.7	70.11
387	130.8	67.81
388	131.0	66.50
389	131.1	67.55
390	131.2	66.49
391	131.4	66.73
392	131.5	68.51
393	131.7	68.81
394	131.8	64.27
395	132.0	63.41
396	132.1	62.86
397	132.2	62.60
398	132.4	62.86
399	132.5	63.88
400	132.6	61.96
401	132.8	62.82
402	132.9	62.07

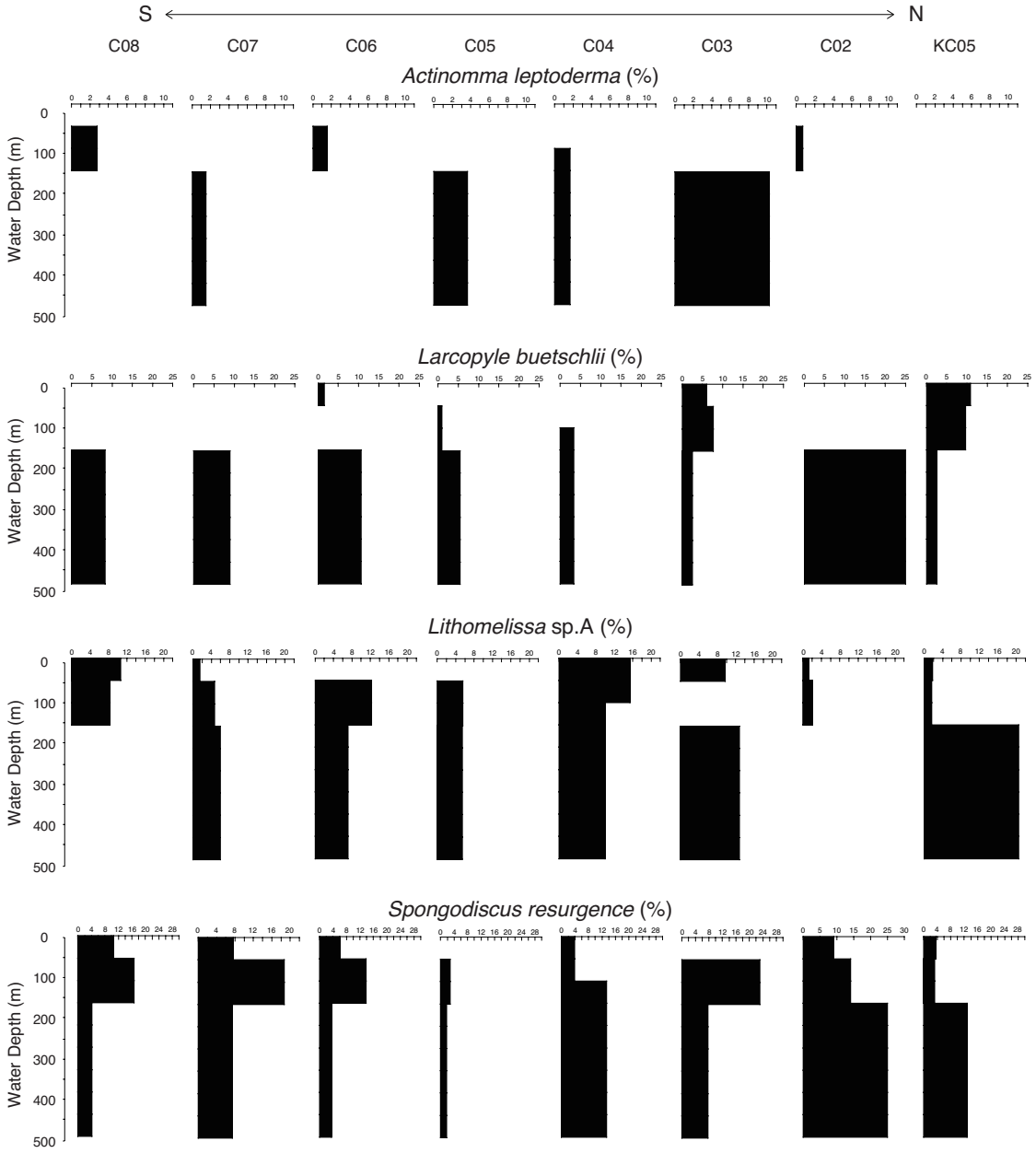
403	133.1	63.02
404	133.2	61.64
405	133.4	63.08
406	133.5	61.96
407	133.6	62.84
408	133.8	63.51
409	133.9	61.67
410	134.1	61.65
411	134.2	60.78
412	134.4	62.22
413	134.5	61.35
414	134.6	61.03
415	134.8	60.70
416	134.9	60.65
417	135.1	60.04
418	135.2	59.63
419	135.4	61.23
420	135.5	63.78
421	135.6	62.20
422	135.8	62.65
423	135.9	63.47
424	136.1	62.75
425	136.2	63.87
426	136.4	64.10
427	136.5	63.40
428	136.6	63.58
429	136.8	63.75
430	136.9	63.13
431	137.1	61.56
432	137.2	62.99
433	137.4	62.95
434	137.5	63.75
435	137.6	62.40
436	137.8	62.96
437	137.9	63.18
438	138.1	63.92
439	138.2	61.95
440	138.4	61.45
441	138.5	61.52
442	138.7	63.92
443	138.8	64.76
444	138.9	62.44
445	139.1	63.21
446	139.2	63.38
447	139.4	63.08
448	139.5	62.72

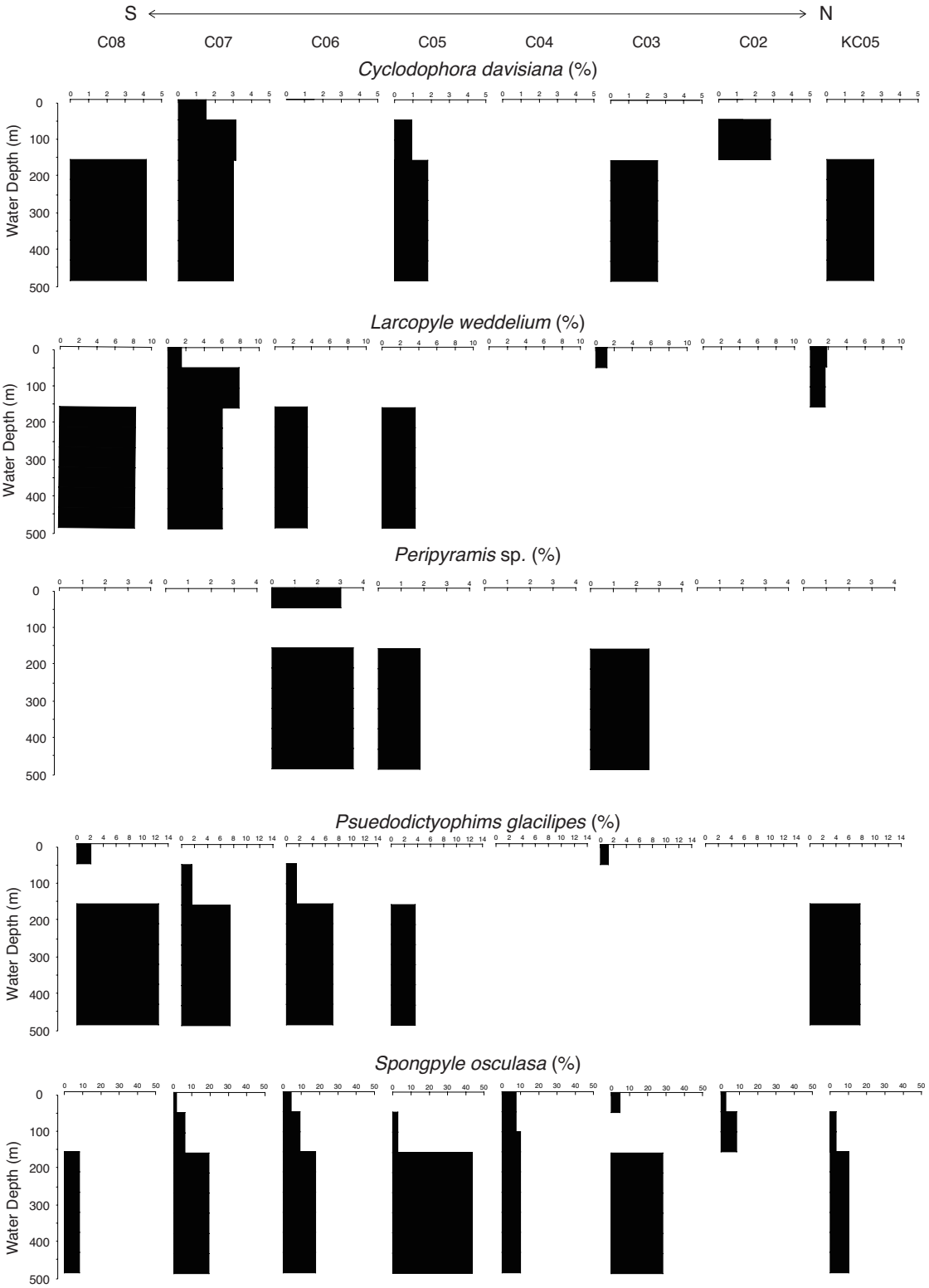
449	139.7	63.37
450	139.8	64.35
451	139.9	65.07
452	140.1	63.65
453	140.2	64.80
454	140.4	63.72
455	140.5	64.35
456	140.7	66.04
457	140.8	63.53
458	140.9	62.65
459	141.1	62.58
460	141.2	65.17
461	141.4	61.89
462	141.5	62.22
463	141.7	60.76
464	141.8	63.98
465	141.9	64.34
466	142.1	63.85
467	142.2	64.49
468	142.4	63.93
469	142.5	67.55
470	142.7	66.10
471	142.8	64.39
472	142.9	66.18
473	143.1	65.74
474	143.2	65.83
475	143.4	63.68
476	143.5	65.58
477	143.7	64.67
478	143.8	62.86
479	143.9	63.90
480	144.1	64.71
481	144.2	65.92
482	144.4	64.03
483	144.5	65.58
484	144.7	64.88
485	144.8	64.90
486	144.9	63.55
487	145.1	63.43
488	145.2	62.89
489	145.4	62.30
490	145.5	62.78
491	145.7	62.39
492	145.8	63.59
493	145.9	64.15
494	146.1	67.20

Supplementary data for Chapter 2

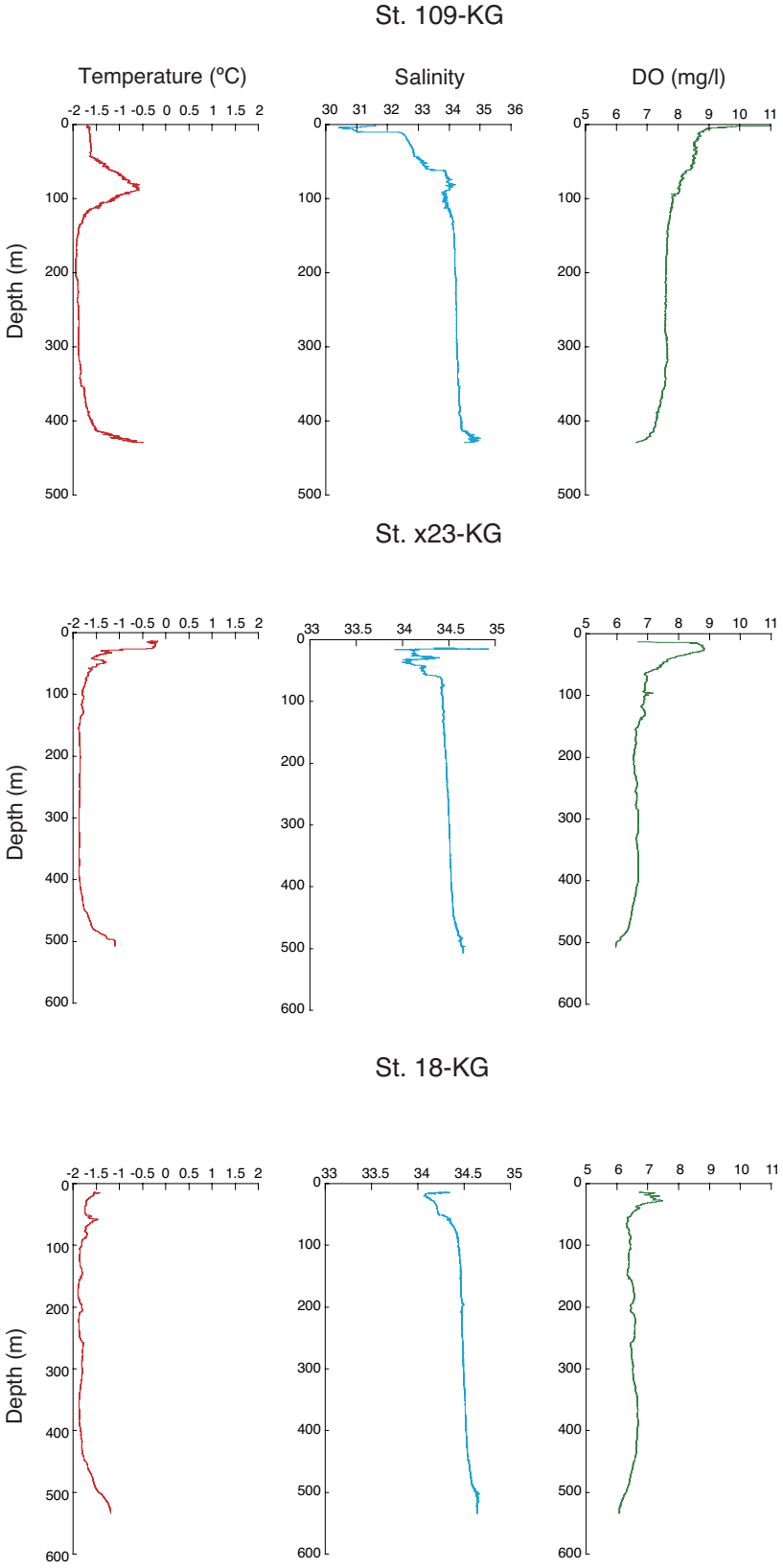
Supplementary Figure 1 | Living depth profiles of radiolarian species from plankton tow samples.



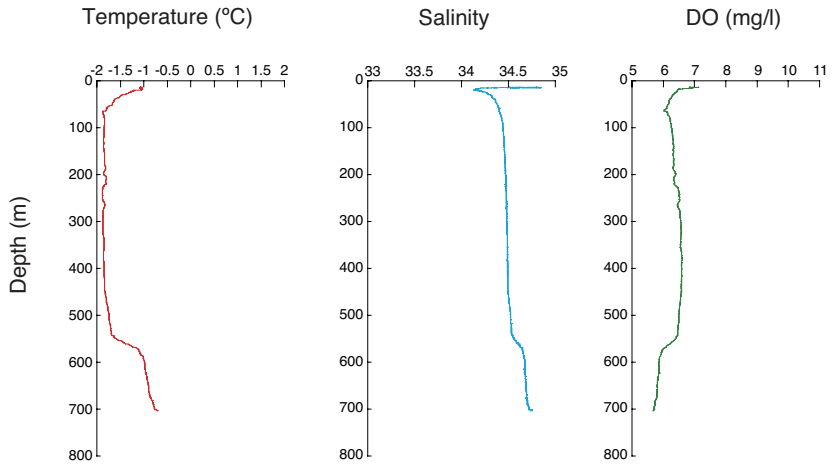

S
N
C08
C07
C06
C05
C04
C03
C02
KC05
Actinomma leptoderma (%)
Larcopyle buetschlii (%)
Lithomelissa sp.A (%)
Spongodiscus resurgence (%)
Water Depth (m)


S
N
C08
C07
C06
C05
C04
C03
C02
KC05
Cyclodophora davisiana (%)
Larcopyle weddelium (%)
Peripyramis sp. (%)
Psuedodictyophims glacilipes (%)
Spongpyle osculasa (%)
Water Depth (m)

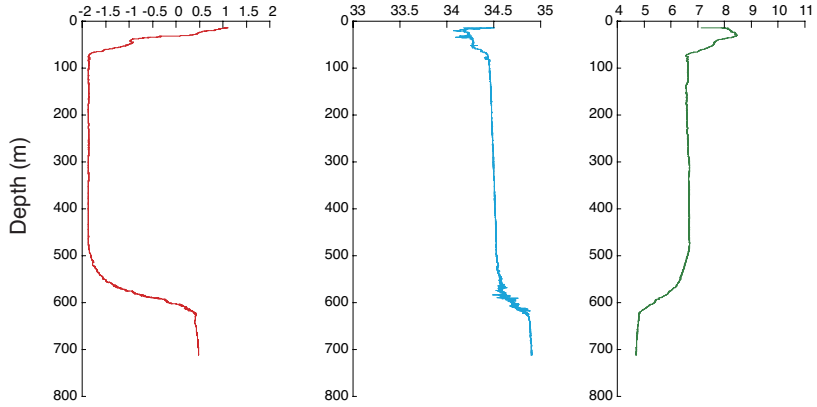
Supplementary Figure 2 | Temperature and Salinity profiles



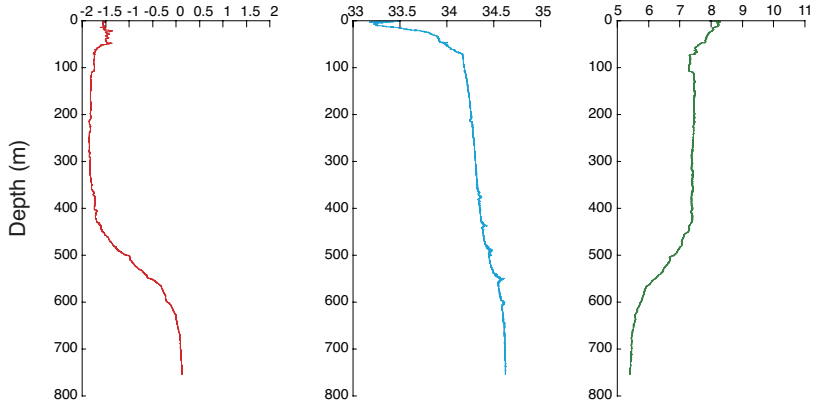
St. 15-KG



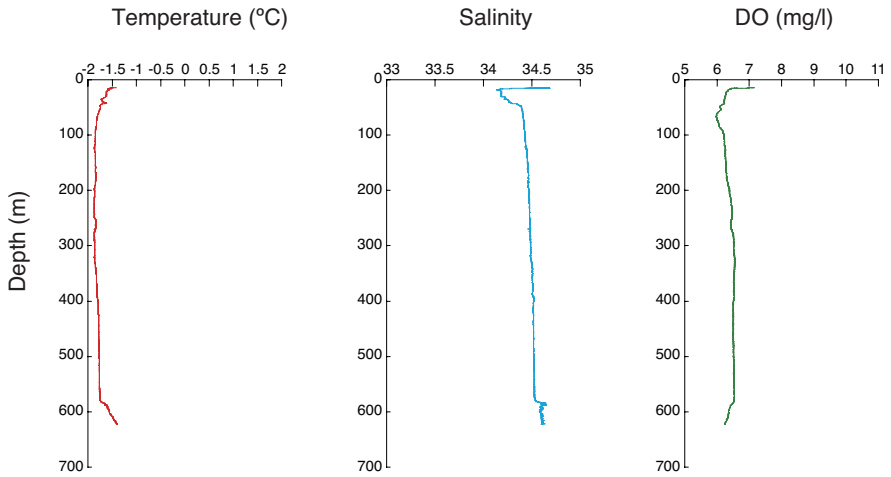
St. 26-KG



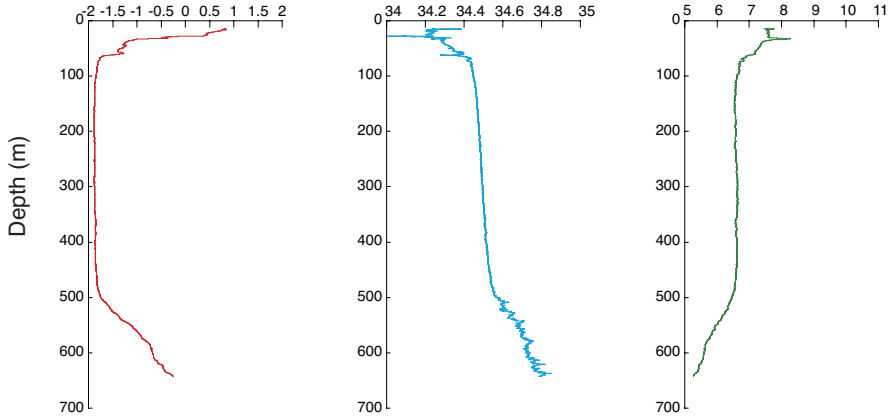
St. LH1a-KG



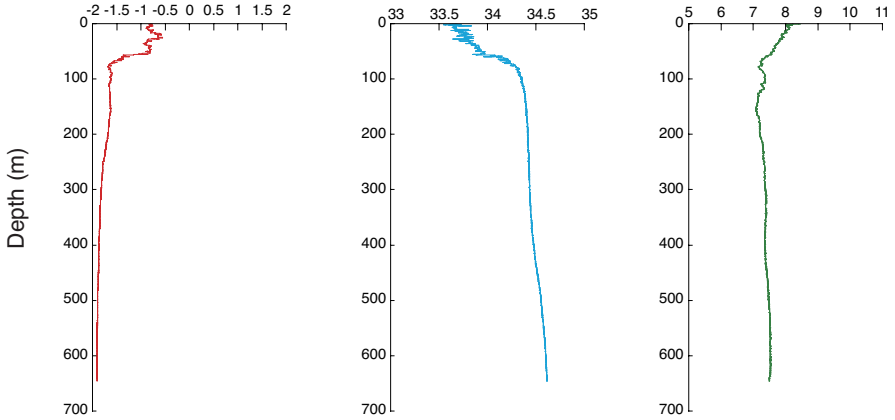
St. 17-KG

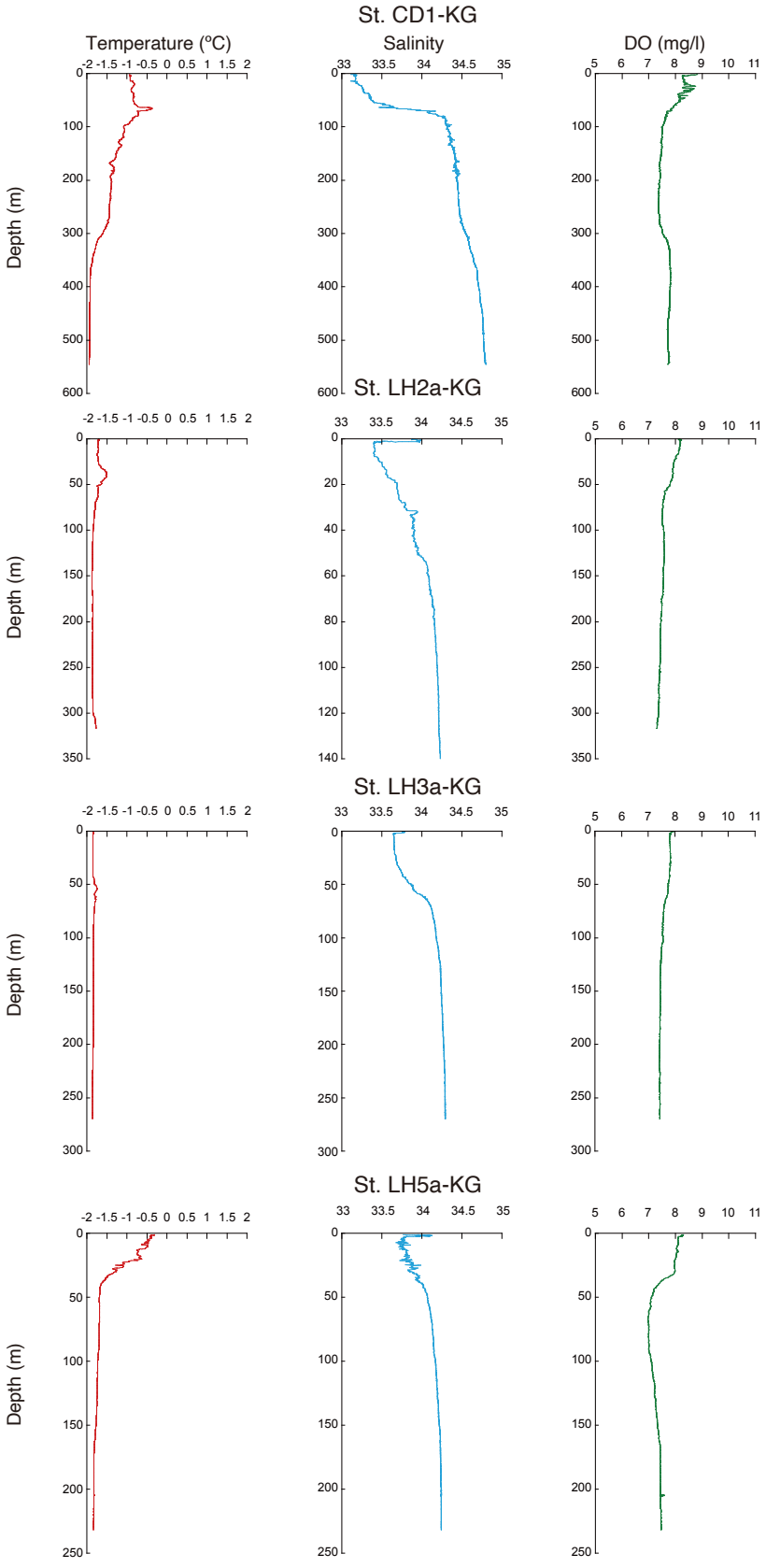


St. 25-KG

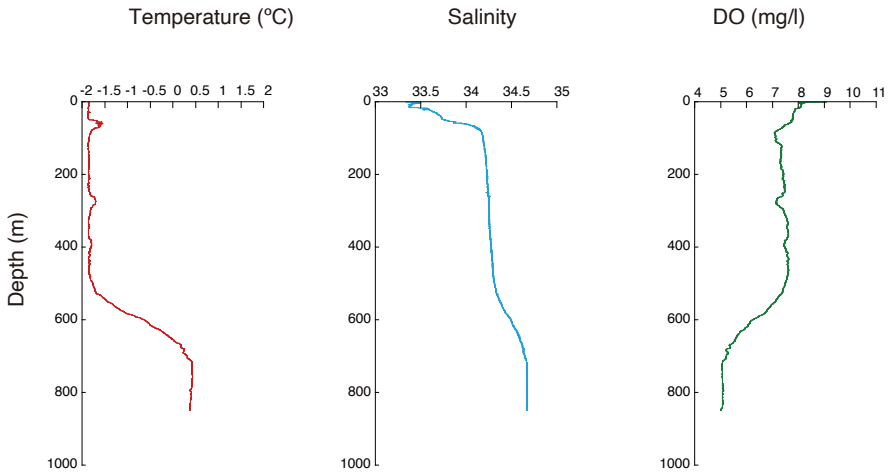


St. CD4-KG

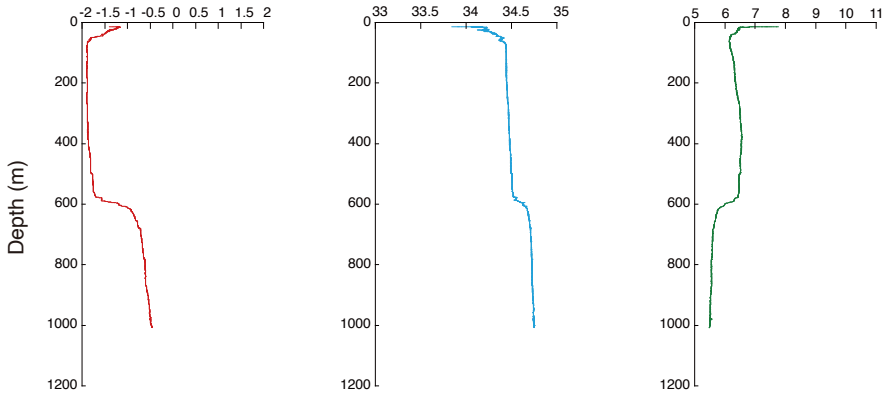



St. CD1-KG
Temperature (°C)
Salinity
DO (mg/l)
Depth (m)
St. LH2a-KG
St. LH3a-KG
St. LH5a-KG

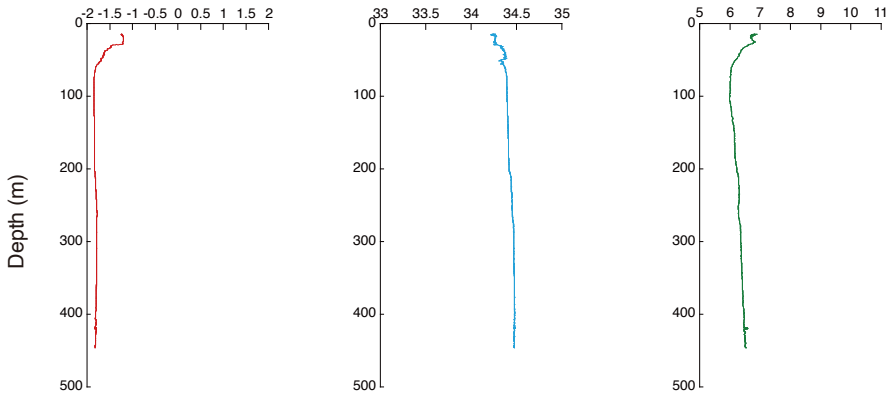
St. 83-KG



St. 14B-KG



St. 12B-KG



Supplementary Table 1 | Taxonomic references

Taxa	Taxonomic references
Acanthosphaera spp.	
Actinomma antarcticum (Haeckel)	Nigrini (1967), p. 26, pl. 2, figs. 1a-d.
Actinomma delicatulum (Dogiel)	Welling (1996), p. 207, pl. 2, figs. 6–7.
Actinomma boreale (Cleve)	Itaki et al. (2009), p. 44, pl. 2, figs, 5, 6, 11.
Actinomma leptodermum (Jorgensen)	Itaki et al. (2009), p. 44, pl. 2, figs, 1–4.
Antarctissa denticulata (Ehrenberg)	Petrushevskaya (1967), p. 87, figs. 49 I-VI.
Antarctissa strelkovi Petrushevskaya	Petrushevskaya (1967), p. 89, figs. 51 III-VI.
Cenosphaera spp.	
Ceratocyrtis histricosus (Jørgensen)	Itaki (2009), p. 52, pl. 20, figs. 1–3, 7–8.
Ceratospyris borealis Bailey	Itaki (2009), p. 48, pl. 13, figs. 6, 10, 11.
Cladoscenium ancoratum Haeckel	Takahashi (1991), p. 94, pl. 24, figs. 9–14.
Collosphaera spp.	
Cornutella profunda (Ehrenberg)	Takahashi (1991), p. 113, pl. 35, fig. 3–9.
Cycladophora bicornis (Popofsky)	Takahashi (1991), p. 122, pl. 41, figs. 4–6, 8–11.
Cycladophora cornutoides Petrushevskaya	Motoyama (1997), p. 57, pl. 1, figs. 1–3.
Cycladophora davisiana Ehrenberg	Motoyama (1997) p. 57, pl. 1, figs. 4–10.
Druppatractus variabilis Dumitrice	Dumitrica (1973), p.833, pl. 6, fig. 4, pl. 20, figs. 6, 7.
Eucecryphalus cervus (Ehrenberg)	Petrushevskaya (1971), p. 223–224, figs. 104 I–VII.
Hexapyle dodecantha Haeckel	Renz (1976), p. 113-114, pl. 1, fig. 11
Larcopyle buetschlii Dreyer	Itaki (2009), p. 48, pl. 12, figs. 1-21.
Larcopyle nebulum Lazarus, Faust and Popova	Itaki (2009), p. 48, pl. 11, fig. 9.
Larcopyle pylomaticus (Riedel)	Lazarus et al. (2005), p. 116, pl. 9, figs. 1-12.
Larcopyle weddelium (Lazarus, Faust and Popova-Goll)	Itaki (2009), p. 48, pl. 11, fig. 5.
Larcospira minor (Jørgensen)	Dolven et al. (2014), p. 33–35, pl. 2, figs. 7–10.
Lithelius nautiloides Popofsky	Petrushevskaya (1967), p. 53-55, figs. 27, 28.
Lithocampe spp.	
Lithomelissa sp. A	Petrushevskaya (1967), p. 76, figs. 45 I-VIII, figs. 46 I-III.
Lonchosphaera spicata Popofsky	Dumitrica (2014), p. 61-62, figs. 1a-1d, 2f.
Lophospyris pentagona (Ehrenberg)	Petrushevskaya (1971), p. 254, figs. 132 I–IX.
Peripyramis sp.	
Peripyramis circumtexta Haeckel	Petrushevskaya (1967), p. 113–114, figs. 64 I-II, figs. 65 I-II.
Plectacantha oikiskos (Jørgensen)	Benson (1983), p. 506, pl. 7, figs.13–14.
Phormospyris stabilis (Goll) *antarctica* (Haecker)	Nigrini and Moore (1979), p. N17-N18, pl. 20, figs. 1a-d.
Phorticium clevei Haeckel	Matsuzaki et al. (2015), p. 32, Figs. 6.9–6.10
Phorticium pylonium (Haeckel) group	Matsuzaki et al. (2015), p. 32, Figs. 6.11–6.12
Plectaniscus cortiniscus (Heackel)	Haeckel (1887), p. 925, pl. 91, fig. 9.
Pseudodictyophimus bicornis (Ehrenberg)	Welling (1996), p. 223, pl. 13, Figs. 13-14.
Pseudodictyophimus gracilipes (Bailey)	Welling (1996), p. 223, pl. 13, Figs. 16-20.
Pseudodictyophimus platycephalus (Haeckel)	Welling (1996), p. 223, pl. 13, Fig. 23.
Rhizoplegma boreale (Cleve)	Jørgensen (1905), pl. 9, Fig. 38, pl. 10, Fig. 38e, 38f.
Saccospyris antarctica Haecker	Goll (1967), p. 394, pl. 4, figs. 7-9.
Saccospyris conithorax Petrushevskaya	Johnson and Nigrini, p. 139, fig. 15b, pl. 4, fig. 12
Siphocampe arachnea (Ehrenberg)	Nigrini, (1977), p. 256, pl. 3, figs. 7-8.
Spongodiscus biconcavus Haeckel	Itaki et al. (2010), figs. 3.15–3.16
Spongodiscus resurgens Ehrenberg	Takahashi (1991), p. 84, pl. 19, fig. 1
Spongopyle osculosa Dreyer	Nigrini and Moore (1979), p. S115, pl. 15, Fig. 1.
Spongotrochus glacialis Popofsky	Petrushevskaya (1967), figs. 21 I–VII, 22 I–VII, 26 II.
Stylatractus neptunus Heackel	Sugiyama et al., p. 12, pl. 3, figs. 7-10
Stylodictya spp.	
Tetrapyle octacantha Müller group	Itaki (2009), p.47, pl.10, figs. 1–10.
Zygocircus archicircus Popofsky	Goll (1979), p. 380-381, pl. 1, figs. 1-2, 5-15.
Dictyophims spp.	

Supplementary Table 3 | Radiolarian abundance of plankton tows

Site	Depth	Standing stock (specimens/m^3)
KC5	50-100	26005
KC5	100-200	878
KC5	200-500	23
C02	50-100	306
C02	100-200	608
C02	200-500	9
C03	0-50	0
C03	50-100	60
C03	100-200	94
C03	200-500	15
C04	0-50	13
C04	50-100	57
C04	100-200	101
C04	200-500	37
C05	0-50	7
C05	50-100	0
C05	100-200	111
C05	200-500	51
C06	0-50	0
C06	50-100	168
C06	100-200	94
C06	200-500	18
C07	0-50	6
C07	50-100	474
C07	100-200	220
C07	200-500	14
C08	50-100	219
C08	100-200	72
C08	200-500	17

Supplementary Table 4 | Radiolarian abundance of surface sediments

Local station	Abundance (specimens/g)
St. 12B-KG	1766
St. 14B-KG	7566
St. 15-KG	13002
St. 17-KG	2203
St. 18-KG	6879
St. 25-KG	1485
St. 26-KG	13104
St. X23-KG	19636
St. LH5a-KG	0
St. LH1a-KG	3377
St. LH2a-KG	645
St. LH3a-KG	0
St. CD4-KG	10194
St. CD1-KG	1939
St. 83-KG	0
St. 109-KG	2399
PC302	3247
PC503	2008
G404	0
G501	0
GC1004	10246
GC1006	3627
GC1301	10983
GC1509	4246
GC1903	275661
GC1904	38747
GC1905	0
GC1906	0
GC2001	190928
GC2002	426742
GC2003	107576
GC2005	14588
GC2006	0
GC2009	0

Supplementary Table 3 | Radiolarian counts of (a) living and (b) dead specimens in plankton tows

(a) Live specimens

Site	KC5	KC5	KC5	C02	C02	C02
Depth (m)	50-100	100-200	200-500	50-100	100-200	200-500
***Acanthosphaera* spp.**	0	0	0	0	0	0
Actinomma antarcticum	0	0	0	3	3	0
Actinomma leptderma	0	0	0	0	1	0
Antarctissa denticulata	14	14	10	39	34	2
***Antarctissa* juvenile**	8	8	1	26	43	0
Antarctissa strelkovi	7	7	0	1	1	0
***Cenosphaera* spp.**	0	0	0	0	0	0
Cycladophora bicornis	0	2	0	1	5	0
Cycladophora davisiana	0	0	1	0		0
Larcopyle buetschlii	6	6	1	0	0	1
Larcopyle juvenile	1	1	0	8	15	0
Larcopyle weddelium	1	1	0	0	0	0
Larcospira minor	0	0	0	0	0	0
***Lithocampe* spp.**	0	1	2	0	0	0
***Lithomelissa* sp. A**	1	1	8	1	3	0
***Peripyramis* sp.**	0	0	0	0	0	0
Plectcantha oikiskos	5	5	0	0	0	0
Phormospyris stabilis antarctica	2	2	0	0	6	0
Pseudodictyophimus bicornis	0	0	0	0	0	0
Pseudodictyophimus gracilipes	0	0	3	0	0	0
Rhizoplegma boreale	0	0	0	0	0	0
Saccospyris antarctica	1	2	0	2	2	0
Spongodiscus resurgens	2	2	5	7	20	1
Spongopyle osculasa	0	2	4	2	12	0
Spongotrochus glacialis	7	8	4	0	3	0
***Stylodictya* spp.**	0	0	0	0	0	0
others	0	0	0	0	1	0

(a) Live specimens

Site	**C03**	**C03**	**C03**	**C03**	**C04**	**C04**
Depth (m)	**0-50**	**50-100**	**100-200**	**200-500**	**0-50**	**50-100**
***Acanthosphaera* spp.**	0	2	0	0	0	0
Actinomma antarcticum	0	0	0	0	2	0
Actinomma leptderma	0	0	0	4	0	0
Antarctissa denticulata	0	18	2	3	0	3
***Antarctissa* juvenile**	0	12	3	3	1	5
Antarctissa strelkovi	0	2	0	1	1	1
***Cenosphaera* spp.**	0	0	0	0	0	0
Cycladophora bicornis	0	6	1	1	0	0
Cycladophora davisiana	0	0	0	1	0	0
Larcopyle buetschlii	0	5	1	1	0	0
Larcopyle juvenile	0	1	2	0	0	5
Larcopyle weddelium	0	1	0	0	0	0
Larcospira minor	0	5	0	1	0	2
***Lithocampe* spp.**	0	11	0	0	0	0
***Lithomelissa* sp. A**	0	8	0	5	0	4
***Peripyramis* sp.**	0	0	0	1	0	0
Plectcantha oikiskos	0	0	0	0	0	0
Phormospyris stabilis antarctica	0	2	1	0	0	0
Pseudodictyophimus bicornis	0	0	0	2	0	0
Pseudodictyophimus gracilipes	0	1	0	0	0	0
Rhizoplegma boreale	0	0	0	0	0	2
Saccospyris antarctica	0	1	0	0	0	1
Spongodiscus resurgens	0	0	3	3	1	1
Spongopyle osculasa	0	4	0	11	0	2
Spongotrochus glacialis	0	4	0	2	0	0
***Stylodictya* spp.**	0	0	0	0	0	0
others	0	0	0	0	0	0

(a) Live specimens

Site	**C04**	**C04**	**C05**	**C05**	**C05**	**C05**
Depth (m)	**100-200**	**200-500**	**0-50**	**50-100**	**100-200**	**200-500**
***Acanthosphaera* spp.**	2	1	0	0	2	0
Actinomma antarcticum	0	0	0	0	0	0
Actinomma leptderma	0	1	0	0	0	2
Antarctissa denticulata	3	9	0	0	18	2
***Antarctissa* juvenile**	3	8	0	0	35	0
Antarctissa strelkovi	0	0	0	0	1	1
***Cenosphaera* spp.**	0	0	1	0	0	0
Cycladophora bicornis	1	1	0	0	3	0
Cycladophora davisiana	1	0	0	0	1	1
Larcopyle buetschlii	4	2	0	0	1	3
Larcopyle juvenile	6	4	0	0	14	1
Larcopyle weddelium	0	0	0	0	0	2
Larcospira minor	1	1	0	0	0	3
***Lithocampe* spp.**	2	8	0	0	13	0
***Lithomelissa* sp. A**	1	6	0	0	6	3
***Peripyramis* sp.**	0	0	0	0	0	1
Plectcantha oikiskos	0	0	0	0	0	0
Phormospyris stabilis antarctica	0	0	0	0	2	0
Pseudodictyophimus bicornis	0	0	0	0	0	1
Pseudodictyophimus gracilipes	0	0	0	0	0	2
Rhizoplegma boreale	0	0	0	0	0	0
Saccospyris antarctica	0	0	0	0	1	0
Spongodiscus resurgens	17	8	2	0	3	1
Spongopyle osculasa	9	6	0	0	3	24
Spongotrochus glacialis	4	6	0	0	5	8
***Stylodictya* spp.**	1	0	0	0	0	0
others	2	1	0	0	0	1

(a) Live specimens

Site	C06	C06	C06	C06	C07	C07
Depth (m)	0-50	50-100	100-200	200-500	0-50	50-100
***Acanthosphaera* spp.**	0	2	1	0	0	0
Actinomma antarcticum	0	0	0	0	0	0
Actinomma leptderma	0	0	1	0	0	0
Antarctissa denticulata	0	13	0	6	1	24
***Antarctissa* juvenile**	0	19	0	1	0	17
Antarctissa strelkovi	0	5	1	0	0	1
***Cenosphaera* spp.**	0	0	0	0	0	0
Cycladophora bicornis	0	1	2	0	0	0
Cycladophora davisiana	0	1	0	0	0	1
Larcopyle buetschlii	0	1	0	3	0	0
Larcopyle juvenile	0	4	2	1	0	5
Larcopyle weddelium	0	0	0	1	0	1
Larcospira minor	0	0	1	0	0	0
***Lithocampe* spp.**	0	1	29	4	0	1
***Lithomelissa* sp. A**	0	0	8	2	0	1
***Peripyramis* sp.**	0	2	0	1	0	0
Plectcantha oikiskos	0	0	0	1	0	1
Phormospyris stabilis antarctica	0	2	1	0	0	3
Pseudodictyophimus bicornis	0	0	0	0	0	0
Pseudodictyophimus gracilipes	0	0	1	2	0	0
Rhizoplegma boreale	0	0	0	0	0	0
Saccospyris antarctica	0	0	0	0	0	1
Spongodiscus resurgens	0	4	9	1	0	5
Spongopyle osculasa	0	3	6	5	0	1
Spongotrochus glacialis	0	6	3	2	0	4
***Stylodictya* spp.**	0	0	0	1	0	0
others	0	2	0	0	0	0

(a) Live specimens

Site	C07	C07	C08	C08	C08
Depth (m)	100-200	200-500	50-100	100-200	200-500
***Acanthosphaera* spp.**	1	0	1	0	0
Actinomma antarcticum	0	0	0	0	0
Actinomma leptderma	0	1	0	1	0
Antarctissa denticulata	2	1	0	6	7
***Antarctissa* juvenile**	5	0	24	4	0
Antarctissa strelkovi	4	0	5	2	0
***Cenosphaera* spp.**	0	0	0	0	0
Cycladophora bicornis	0	0	0	1	0
Cycladophora davisiana	2	2	0	0	1
Larcopyle buetschlii	0	6	0	0	2
Larcopyle juvenile	1	1	0	0	0
Larcopyle weddelium	5	4	0	0	2
Larcospira minor	0	0	0	1	0
***Lithocampe* spp.**	18	3	1	8	2
***Lithomelissa* sp. A**	3	4	5	3	0
***Peripyramis* sp.**	0	0	0	0	0
Plectcantha oikiskos	0	0	3	0	0
Phormospyris stabilis antarctica	0	0	2	0	0
Pseudodictyophimus bicornis	0	0	0	0	0
Pseudodictyophimus gracilipes	1	5	1	0	3
Rhizoplegma boreale	0	0	0	0	0
Saccospyris antarctica	1	0	0	0	0
Spongodiscus resurgens	12	5	5	6	1
Spongopyle osculasa	4	13	0	0	2
Spongotrochus glacialis	4	16	0	4	2
***Stylodictya* spp.**	0	0	0	0	0
others	1	6	0	0	2

(b) Dead specimens

Site	**KC5**	**KC5**	**KC5**	**C02**	**C02**	**C02**
Depth (m)	**50-100**	**100-200**	**200-500**	**50-100**	**100-200**	**200-500**
***Acanthosphaera* spp.**	0	0	0	0	0	0
Actinomma antarcticum	0	0	0	0	0	0
Actinomma leptderma	0	0	0	0	0	0
Antarctissa denticulata	1	1	1	1	0	0
***Antarctissa* juvenile**	0	0	1	2	0	0
Antarctissa strelkovi	7	1	0	0	0	0
***Cenosphaera* spp.**	0	0	0	0	0	0
Cycladophora bicornis	0	0	0	0	0	0
Cycladophora davisiana	0	1	0	0	0	0
Larcopyle buetschlii	0	0	1	0	0	0
Larcopyle juvenile	0	0	0	0	0	0
Larcopyle weddelium	0	0	0	0	0	0
Larcospira minor	0	0	0	0	0	0
***Lithocampe* spp.**	0	0	0	0	0	0
***Lithomelissa* sp. A**	0	2	1	0	0	0
***Peripyramis* sp.**	0	0	0	0	0	0
Plectcantha oikiskos	0	0	0	0	0	0
Phormospyris stabilis antarctica	0	0	0	0	0	0
Pseudodictyophimus bicornis	0	0	0	0	0	0
Pseudodictyophimus gracilipes	0	0	0	0	0	0
Rhizoplegma boreale	0	0	1	0	0	0
Saccospyris antarctica	0	0	0	0	0	0
Spongodiscus resurgens	0	0	0	0	0	0
Spongopyle osculasa	0	2	0	0	0	0
Spongotrochus glacialis	0	0	0	0	0	0
***Stylodictya* spp.**	0	0	0	0	0	0
others	0	0	0	0	0	0

(b) Dead specimens

Site	**C03**	**C03**	**C03**	**C03**	**C04**	**C04**
Depth (m)	**0-50**	**50-100**	**100-200**	**200-500**	**0-50**	**50-100**
***Acanthosphaera* spp.**	0	0	0	0	0	0
Actinomma antarcticum	0	0	0	0	0	0
Actinomma leptderma	0	0	0	0	0	0
Antarctissa denticulata	0	1	1	7	0	0
***Antarctissa* juvenile**	0	2	0	3	0	0
Antarctissa strelkovi	0	0	0	0	0	0
***Cenosphaera* spp.**	0	0	0	0	0	0
Cycladophora bicornis	0	0	0	0	0	0
Cycladophora davisiana	0	0	0	0	0	0
Larcopyle buetschlii	0	0	0	0	0	0
Larcopyle juvenile	0	0	0	3	0	0
Larcopyle weddelium	0	0	0	0	0	0
Larcospira minor	0	0	0	0	0	0
***Lithocampe* spp.**	0	2	0	0	0	0
***Lithomelissa* sp. A**	0	3	0	7	0	0
***Peripyramis* sp.**	0	0	0	0	0	0
Plectcantha oikiskos	0	0	0	0	0	0
Phormospyris stabilis antarctica	0	0	0	0	0	0
Pseudodictyophimus bicornis	0	0	0	1	0	1
Pseudodictyophimus gracilipes	0	0	0	0	0	0
Rhizoplegma boreale	0	0	0	0	0	0
Saccospyris antarctica	0	0	0	0	0	0
Spongodiscus resurgens	0	0	0	0	0	0
Spongopyle osculasa	0	0	0	0	0	0
Spongotrochus glacialis	0	0	0	0	0	0
***Stylodictya* spp.**	0	0	0	0	0	0
others	0	0	0	0	0	0

(b) Dead specimens

Site	**C04**	**C04**	**C05**	**C05**	**C05**	**C05**
Depth (m)	**100-200**	**200-500**	**0-50**	**50-100**	**100-200**	**200-500**
***Acanthosphaera* spp.**	0	1	0	0	0	0
Actinomma antarcticum	0	0	0	0	0	0
Actinomma leptderma	0	0	0	0	0	0
Antarctissa denticulata	0	0	0	0	3	0
***Antarctissa* juvenile**	0	0	0	0	3	0
Antarctissa strelkovi	0	0	0	0	0	0
***Cenosphaera* spp.**	0	0	0	0	0	0
Cycladophora bicornis	1	0	0	0	0	0
Cycladophora davisiana	0	0	0	0	0	0
Larcopyle buetschlii	0	0	0	0	0	0
Larcopyle juvenile	0	0	0	0	0	0
Larcopyle weddelium	0	0	0	0	0	0
Larcospira minor	0	0	0	0	0	0
***Lithocampe* spp.**	0	0	0	0	0	0
***Lithomelissa* sp. A**	0	0	0	0	0	0
***Peripyramis* sp.**	0	0	0	0	0	0
Plectcantha oikiskos	0	0	0	0	0	0
Phormospyris stabilis antarctica	0	0	0	0	0	0
Pseudodictyophimus bicornis	1	0	0	0	0	0
Pseudodictyophimus gracilipes	0	0	0	0	0	0
Rhizoplegma boreale	1	0	0	0	0	1
Saccospyris antarctica	0	0	0	0	0	0
Spongodiscus resurgens	0	0	0	0	0	0
Spongopyle osculasa	0	0	2	0	0	0
Spongotrochus glacialis	0	0	0	0	0	0
***Stylodictya* spp.**	0	0	0	0	0	0
others	0	0	0	0	0	0

(b) Dead specimens

Site	**C06**	**C06**	**C06**	**C06**	**C07**	**C07**
Depth (m)	**0-50**	**50-100**	**100-200**	**200-500**	**0-50**	**50-100**
***Acanthosphaera* spp.**	0	0	0	0	0	0
Actinomma antarcticum	0	0	0	0	0	0
Actinomma leptderma	0	0	0	0	0	0
Antarctissa denticulata	0	0	1	7	0	0
***Antarctissa* juvenile**	0	0	0	0	0	0
Antarctissa strelkovi	0	0	0	0	0	0
***Cenosphaera* spp.**	0	0	0	0	2	0
Cycladophora bicornis	0	0	0	0	0	0
Cycladophora davisiana	0	0	0	0	0	0
Larcopyle buetschlii	0	0	0	0	0	0
Larcopyle juvenile	0	0	0	0	0	0
Larcopyle weddelium	0	0	0	0	0	0
Larcospira minor	0	0	0	0	0	0
***Lithocampe* spp.**	0	0	0	0	0	0
***Lithomelissa* sp. A**	0	0	0	0	0	0
***Peripyramis* sp.**	0	0	0	0	0	0
Plectcantha oikiskos	0	0	0	0	0	0
Phormospyris stabilis antarctica	0	0	0	0	0	0
Pseudodictyophimus bicornis	0	0	0	0	0	0
Pseudodictyophimus gracilipes	0	0	0	0	0	0
Rhizoplegma boreale	0	0	0	0	0	0
Saccospyris antarctica	0	0	0	0	0	0
Spongodiscus resurgens	0	0	0	0	0	0
Spongopyle osculasa	0	0	0	0	0	0
Spongotrochus glacialis	0	0	0	0	0	0
***Stylodictya* spp.**	0	0	0	0	0	0
others	0	0	0	0	0	0

(b) Dead specimens

Site	**C07**	**C07**	**C08**	**C08**	**C08**
Depth (m)	**100-200**	**200-500**	**50-100**	**100-200**	**200-500**
***Acanthosphaera* spp.**	0	1	0	0	0
Actinomma antarcticum	0	0	0	0	0
Actinomma leptderma	0	0	0	0	0
Antarctissa denticulata	0	25	0	0	0
***Antarctissa* juvenile**	0	1	0	0	0
Antarctissa strelkovi	0	1	0	0	0
***Cenosphaera* spp.**	0	0	0	0	0
Cycladophora bicornis	0	0	0	0	0
Cycladophora davisiana	0	0	0	0	0
Larcopyle buetschlii	0	0	0	0	0
Larcopyle juvenile	0	0	0	0	0
Larcopyle weddelium	0	0	0	0	0
Larcospira minor	0	0	0	0	0
***Lithocampe* spp.**	0	1	0	0	0
***Lithomelissa* sp. A**	0	0	0	1	0
***Peripyramis* sp.**	0	0	0	0	0
Plectcantha oikiskos	0	0	0	0	0
Phormospyris stabilis antarctica	0	0	0	0	0
Pseudodictyophimus bicornis	0	0	0	0	0
Pseudodictyophimus gracilipes	0	0	0	0	0
Rhizoplegma boreale	0	0	0	0	0
Saccospyris antarctica	0	0	0	0	0
Spongodiscus resurgens	0	0	0	0	0
Spongopyle osculasa	0	0	0	0	0
Spongotrochus glacialis	0	0	0	0	0
***Stylodictya* spp.**	0	0	0	0	0
others	0	0	0	0	0

Supplementary Table 4 | Radiolarian abundance (%) from plankton tow samples

Living specimens (%)

Site	KC5	KC5	KC5	C02	C02
Depth	50-100	100-200	200-500	50-100	100-200
Acanthosphaera spp.	0	0	0	0	0
Actinomma antarcticum	0	0	0	3.90	2.11
Actinomma leptoderma	0	0	0	0	0.70
Antarctissa denticulata	25.45	22.58	25.64	33.77	19.01
Antarctissa juvenile	14.55	12.90	2.56	33.77	30.28
Antarctissa strelkovi	12.73	11.29	0	1.30	0.70
Cenosphaera spp.	0	0	0	0	0
Cycladophora bicornis	0	3.23	0	1.30	3.52
Cycladophora davisiana	0	0	2.56	0	0
Larcopyle buetschlii	10.91	9.68	2.56	0	0
Larcopyle buetschlii juvenile	1.82	1.61	0	10.39	10.56
Larcopyle weddelium	1.82	1.61	0	0	0
Lithelius minor	0	0	0	0	0
Lithocampe spp.	0	1.61	5.13	0	0
Lithomelissa sp. A	1.82	1.61	20.51	1.30	2.11
Peripyramis sp.	0	0	0	0	0
Plectcantha oikiskos	9.09	8.06	0	0	0
Phormospyris stabilis antarctica	3.64	3.23	0	0	4.23
Pseudodictyophimus bicornis	0	0	0	0	0
Pseudodictyophimus gracilipes	0	0	7.69	0	0
Rhizoplegma boreale	0	0	0	0	0
Saccospyris antarctica	1.82	3.23	0	2.60	1.41
Spongodiscus resurgens	3.64	3.23	12.82	9.09	14.08
Spongopyle osculasa	0	3.23	10.26	2.60	8.45
Spongotrochus glacialis	12.73	12.90	10.26	0	2.11
Stylodictya spp.	0	0	0	0	0
others	0	0	0	0	0.70

Living specimens (%)

Site	C02	C03	C03	C03	C03
Depth	200-500	0-50	50-100	100-200	200-500
Acanthosphaera spp.	0	0	2.44	0	0
Actinomma antarcticum	0	0	0	0	0
Actinomma leptoderma	0	0	0	0	10.26
Antarctissa denticulata	50.00	0	20.73	15.38	7.69
Antarctissa juvenile	0	0	14.63	23.08	7.69
Antarctissa strelkovi	0	0	2.44	0	2.56
Cenosphaera spp.	0	0	0	0	0
Cycladophora bicornis	0	0	7.32	7.69	2.56
Cycladophora davisiana	0	0	0	0	2.56
Larcopyle buetschlii	25.00	0	6.10	7.69	2.56
Larcopyle juvenile	0	0	1.22	15.38	0
Larcopyle weddelium	0	0	1.22	0	0
Lithelius minor	0	0	6.10	0	2.56
Lithocampe spp.	0	0	13.41	0	0
Lithomelissa sp. A	0	0	9.76	0	12.82
Peripyramis sp.	0	0	0	0	2.56
Plectcantha oikiskos	0	0	0	0	0
Phormospyris stabilis antarctica	0	0	2.44	7.69	0
Pseudodictyophimus bicornis	0	0	0	0	5.13
Pseudodictyophimus gracilipes	0	0	1.22	0	0
Rhizoplegma boreale	0	0	0	0	0
Saccospyris antarctica	0	0	1.22	0	0
Spongodiscus resurgens	25.00	0	0	23.08	7.69
Spongopyle osculasa	0	0	4.88	0	28.21
Spongotrochus glacialis	0	0	4.88	0	5.13
Stylodictya spp.	0	0	0	0	0
others	0	0	0	0	0

Living specimens (%)

Site	C04	C04	C04	C04	C05
Depth	0-50	50-100	100-200	200-500	0-50
Acanthosphaera spp.	0	0	3.51	1.67	0
Actinomma antarcticum	40.00	0	0	0	0
Actinomma leptoderma	0	0	0	1.67	0
Antarctissa denticulata	0	11.54	5.26	11.67	0
Antarctissa juvenile	20.00	19.23	5.26	13.33	0
Antarctissa strelkovi	20.00	3.85	0	0	0
Cenosphaera spp.	0	0	0	0	0
Cycladophora bicornis	0	0	1.75	1.67	0
Cycladophora davisiana	0	0	1.75	0	0
Larcopyle buetschlii	0	0	7.02	3.33	0
Larcopyle juvenile	0	19.23	10.53	6.67	0
Larcopyle weddelium	0	0	0	0	0
Lithelius minor	0	7.69	1.75	1.67	0
Lithocampe spp.	0	0	3.51	13.33	0
Lithomelissa sp. A	0	15.38	1.75	10.00	0
Peripyramis sp.	0	0	0	0	0
Plectcantha oikiskos	0	0	0	0	0
Phormospyris stabilis antarctica	0	0	0	0	0
Pseudodictyophimus bicornis	0	0	0	0	0
Pseudodictyophimus gracilipes	0	0	0	0	0
Rhizoplegma boreale	0	7.69	0	0	0
Saccospyris antarctica	0	3.85	0	0	0
Spongodiscus resurgens	20.00	3.85	29.82	13.33	0
Spongopyle osculasa	0	7.69	15.79	10.00	0
Spongotrochus glacialis	0	0	7.02	10.00	0
Stylodictya spp.	0	0	1.75	0	0
others	0	0	3.51	1.67	0

Living specimens (%)

Site	C05	C05	C05	C06	C06
Depth	50-100	100-200	200-500	0-50	50-100
Acanthosphaera spp.	0	1.87	0	0	3.03
Actinomma antarcticum	0	0	0	0	0
Actinomma leptoderma	0	0	3.64	0	0
Antarctissa denticulata	0	15.89	1.82	0	19.70
Antarctissa juvenile	0	32.71	0	0	28.79
Antarctissa strelkovi	0	0.93	1.82	0	7.58
Cenosphaera spp.	0	0	0	0	0
Cycladophora bicornis	0	2.80	0	0	1.52
Cycladophora davisiana	0	0.93	1.82	0	1.52
Larcopyle buetschlii	0	0.93	5.45	0	1.52
Larcopyle juvenile	0	13.08	1.82	0	6.06
Larcopyle weddelium	0	0	3.64	0	0
Lithelius minor	0	0	5.45	0	0
Lithocampe spp.	0	12.15	0	0	1.52
Lithomelissa sp. A	0	5.61	5.45	0	0
Peripyramis sp.	0	0	1.82	0	3.03
Plectcantha oikiskos	0	0	0	0	0
Phormospyris stabilis antarctica	0	1.87	0	0	3.03
Pseudodictyophimus bicornis	0	0	1.82	0	0
Pseudodictyophimus gracilipes	0	0	3.64	0	0
Rhizoplegma boreale	0	0	0	0	0
Saccospyris antarctica	0	0.93	0	0	0
Spongodiscus resurgens	0	2.80	1.82	0	6.06
Spongopyle osculasa	0	2.80	43.64	0	4.55
Spongotrochus glacialis	0	4.67	14.55	0	9.09
Stylodictya spp.	0	0	0	0	0
others	0	0	1.82	0	3.03

Living specimens (%)

Site	C06	C06	C07	C07	C07
Depth	100-200	200-500	0-50	50-100	100-200
Acanthosphaera spp.	1.5	0	0	0	1.6
Actinomma antarcticum	0	0	0	0	0
Actinomma leptoderma	1.5	0	0	0	0
Antarctissa denticulata	0	10.71	0	36.4	3.1
Antarctissa juvenile	0	3.6	0	25.8	7.8
Antarctissa strelkovi	1.5	0	0	1.5	6.3
Cenosphaera spp.	0	0	0	0	0
Cycladophora bicornis	3.1	0	0	0	0
Cycladophora davisiana	0	0	0	1.5	3.1
Larcopyle buetschlii	0	10.7	0	0	0
Larcopyle juvenile	3.1	3.6	0	7.6	1.6
Larcopyle weddelium	0	3.6	0	1.5	7.8
Lithelius minor	1.5	0	0	0	0
Lithocampe spp.	44.6	14.3	0	1.5	28.1
Lithomelissa sp. A	12.3	7.1	0	1.5	4.7
Peripyramis sp.	0	3.6	0	0	0
Plectcantha oikiskos	0	3.6	0	1.5	0
Phormospyris stabilis antarctica	1.5	0	0	4.5	0
Pseudodictyophimus bicornis	0	0	0	0	0
Pseudodictyophimus gracilipes	1.5	7.1	0	0	1.6
Rhizoplegma boreale	0	0	0	0	0
Saccospyris antarctica	0	0	0	1.5	1.6
Spongodiscus resurgens	13.8	3.6	0	7.6	18.8
Spongopyle osculasa	9.2	17.9	0	1.5	6.3
Spongotrochus glacialis	4.6	7.1	0	6.1	6.3
Stylodictya spp.	0	3.6	0	0	0
others	0	0	0	0	1.6

Living specimens (%)

Site	C07	C08	C08	C08
Depth	200-500	50-100	100-200	200-500
Acanthosphaera spp.	0	2.13	0	0
Actinomma antarcticum	0	0	0	0
Actinomma leptoderma	1.49	0	2.78	0
Antarctissa denticulata	1.49	0	16.67	29.17
Antarctissa juvenile	0	51.06	11.11	0
Antarctissa strelkovi	0	10.64	5.56	0
Cenosphaera spp.	0	0	0	0
Cycladophora bicornis	0	0	2.78	0
Cycladophora davisiana	2.99	0	0	4.17
Larcopyle buetschlii	8.96	0	0	8.33
Larcopyle juvenile	1.49	0	0	0
Larcopyle weddelium	5.97	0	0	8.33
Lithelius minor	0	0	2.78	0
Lithocampe spp.	4.48	2.13	22.22	8.33
Lithomelissa sp. A	5.97	10.64	8.33	0
Peripyramis sp.	0	0	0	0
Plectcantha oikiskos	0	6.38	0	0
Phormospyris stabilis antarctica	0	4.26	0	0
Pseudodictyophimus bicornis	0	0	0	0
Pseudodictyophimus gracilipes	7.46	2.13	0	12.50
Rhizoplegma boreale	0	0	0	0
Saccospyris antarctica	0	0	0	0
Spongodiscus resurgens	7.46	10.64	16.67	4.17
Spongopyle osculasa	19.40	0	0	8.33
Spongotrochus glacialis	23.88	0	11.11	8.33
Stylodictya spp.	0	0	0	0
others	8.96	0	0	8.33

Supplementary Table 5 | Radiolarian counts of specimens in surface sediments

Local Stations	St. 12B-KG	St. 14B-KG	St. 15-KG	St. 17-KG	St. 18-KG
***Acanthosphaera* spp.**	0	0	0	0	0
Actinomma antarcticum	0	0	0	0	0
Actinomma delicatulum	0	0	0	0	0
Actinomma leptoderma	0	1	0	2	1
Antarctissa denticulata	32	127	123	63	137
***Antarctissa* juvenile**	3	23	13	2	0
Antarctissa strelkovi	0	30	13	8	26
***Cenosphaera* spp.**	0	0	0	0	0
Ceratocyrtis histricosus	2	0	0	1	0
Cladoscenium ancoratum	0	3	2	0	1
***Collosphaera* sp.**	0	0	0	0	0
Cornutella profunda	0	0	0	0	0
Cycladophora bicornis	0	2	0	0	0
Cycladophora cornutoides	0	2	2	2	1
Cycladophora davisiana	0	0	0	0	0
***Dictyophims* spp.**	0	0	0	0	0
Duppatratus variabilis	0	0	0	0	0
Eucecryphalus cervus	0	0	0	0	0
Hexapyle dodecantha	0	0	0	0	0
Larcopyle buetschlii	1	2	2	9	6
Larcopyle nebulum	0	0	0	0	0
Larcopyle pylomaticus	0	0	0	0	0
Larcopyle weddelium	0	0	0	0	0
Lithelius minor	1	0	0	0	3
Lithelius nautiloides	0	4	4	0	7
***Lithocampe* spp.**	0	1	4	1	0
Lophospyris pentagona	0	0	0	0	0
Lonchosphaera spicata	0	0	0	0	0
***Lithomelissa* sp. A**	6	28	17	16	3
***Peripyramis* sp.A**	0	0	0	0	0
Peripyramis circumtexta	0	0	0	0	0
Plectcantha oikiskos	6	74	89	102	57
Phormospyris stabilis antarctica	0	1	0	3	1
Phorticium clevei	0	0	0	0	0
Plectaniscus cortiniscus	1	0	0	0	0
Pseudodictyophimus bicornis	0	0	0	0	0
Pseudodictyophimus platycephalus	0	3	0	0	0
Pseudodictyophimus gracilipes	0	2	0	1	1
Rhizoplegma boreale	0	4	0	0	0
Saccospyris antarctica	0	0	4	1	2
Saccospyris conithorax	0	0	0	0	0
Siphocampe arachnea	0	0	1	0	0
Spongodiscus biconcavus	0	0	0	0	0
Spongodiscus resurgens	0	12	15	19	2
Spongopyle osculasa	0	0	0	0	0
Spongotrochus glacialis	1	1	0	0	0
Stylatractus neptunus	0	0	0	0	0
***Stylodictya* spp.**	0	1	9	2	0
Tetrapyle octacantha	0	0	0	0	0
Zygocircus archicircus	0	3	0	0	0
Others	2	5	14	0	3
Total	53	324	298	232	248

Local Stations	St. 25-KG	St. 26-KG	St. X23-KG	St. LH5a-KG	St. LH1a-KG
***Acanthosphaera* spp.**	0	0	0	0	1
Actinomma antarcticum	0	0	0	0	0
Actinomma delicatulum	0	0	1	0	0
Actinomma leptoderma	0	0	1	0	6
Antarctissa denticulata	72	135	133	0	101
***Antarctissa* juvenile**	6	30	9	0	9
Antarctissa strelkovi	18	68	5	0	3
***Cenosphaera* spp.**	0	0	1	0	0
Ceratocyrtis histricosus	0	0	0	0	0
Cladoscenium ancoratum	0	0	0	0	0
***Collosphaera* sp.**	0	0	3	0	0
Cornutella profunda	0	0	0	0	0
Cycladophora bicornis	0	0	0	0	0
Cycladophora cornutoides	0	2	2	0	6
Cycladophora davisiana	0	0	0	0	0
***Dictyophims* spp.**	0	0	0	0	0
Duppatratus variabilis	0	0	0	0	0
Eucecryphalus cervus	0	0	0	0	0
Hexapyle dodecantha	0	0	0	0	0
Larcopyle buetschlii	0	17	9	0	22
Larcopyle nebulum	0	0	0	0	0
Larcopyle pylomaticus	0	0	0	0	2
Larcopyle weddelium	0	2	0	0	2
Lithelius minor	0	3	1	0	2
Lithelius nautiloides	3	6	4	0	2
***Lithocampe* spp.**	1	3	1	0	1
Lophospyris pentagona	0	0	0	0	0
Lonchosphaera spicata	0	0	0	0	0
***Lithomelissa* sp. A**	3	27	17	0	3
***Peripyramis* sp.A**	0	0	0	0	0
Peripyramis circumtexta	0	0	0	0	0
Plectcantha oikiskos	17	1	53	0	0
Phormospyris stabilis antarctica	0	4	0	0	1
Phorticium clevei	0	0	0	0	0
Plectaniscus cortiniscus	0	0	0	0	0
Pseudodictyophimus bicornis	0	1	0	0	0
Pseudodictyophimus platycephalus	0	0	0	0	0
Pseudodictyophimus gracilipes	0	0	0	0	2
Rhizoplegma boreale	0	1	1	0	1
Saccospyris antarctica	0	1	2	0	1
Saccospyris conithorax	0	0	0	0	0
Siphocampe arachnea	0	0	0	0	0
Spongodiscus biconcavus	2	0	0	0	0
Spongodiscus resurgens	5	24	27	0	38
Spongopyle osculasa	0	0	0	0	0
Spongotrochus glacialis	0	0	1	0	2
Stylatractus neptunus	0	0	0	0	1
***Stylodictya* spp.**	0	1	0	0	1
Tetrapyle octacantha	0	0	0	0	1
Zygocircus archicircus	1	4	3	0	1
Others	0	3	1	0	0
Total	128	330	274	0	208

Local Stations	St. LH3a-KG	St. CD4-KG	St. CD1-KG	St. 83-KG	St. 108-KG
***Acanthosphaera* spp.**	0	0	0	0	0
Actinomma antarcticum	0	0	0	0	0
Actinomma delicatulum	0	0	0	0	0
Actinomma leptoderma	0	1	1	7	0
Antarctissa denticulata	0	92	32	27	0
***Antarctissa* juvenile**	0	1	10	0	0
Antarctissa strelkovi	0	7	6	3	0
***Cenosphaera* spp.**	0	0	0	1	0
Ceratocyrtis histricosus	0	0	0	0	0
Cladoscenium ancoratum	0	0	0	0	0
***Collosphaera* sp.**	0	0	0	0	0
Cornutella profunda	0	0	0	0	0
Cycladophora bicornis	0	0	0	0	0
Cycladophora cornutoides	0	0	0	5	0
Cycladophora davisiana	0	0	0	0	0
***Dictyophims* spp.**	0	0	0	0	0
Duppatratus variabilis	0	0	0	0	0
Eucecryphalus cervus	0	0	0	0	0
Hexapyle dodecantha	0	0	0	0	0
Larcopyle buetschlii	0	3	0	9	0
Larcopyle nebulum	0	0	0	0	0
Larcopyle pylomaticus	0	1	0	0	0
Larcopyle weddelium	0	0	0	0	0
Lithelius minor	0	0	0	0	0
Lithelius nautiloides	1	1	1	0	0
***Lithocampe* spp.**	0	0	1	0	0
Lophospyris pentagona	0	0	0	0	0
Lonchosphaera spicata	0	0	0	0	0
***Lithomelissa* sp. A**	0	6	4	11	0
***Peripyramis* sp.A**	0	0	0	0	0
Peripyramis circumtexta	0	0	0	0	0
Plectcantha oikiskos	1	229	4	25	0
Phormospyris stabilis antarctica	0	0	0	0	0
Phorticium clevei	0	0	0	0	0
Plectaniscus cortiniscus	0	0	0	0	0
Pseudodictyophimus bicornis	0	0	0	0	0
Pseudodictyophimus platycephalus	0	0	0	0	0
Pseudodictyophimus gracilipes	0	0	0	0	0
Rhizoplegma boreale	0	1	1	0	0
Saccospyris antarctica	0	0	0	0	0
Saccospyris conithorax	0	0	0	0	0
Siphocampe arachnea	0	0	0	0	0
Spongodiscus biconcavus	0	0	0	0	0
Spongodiscus resurgens	0	5	2	27	0
Spongopyle osculasa	0	0	0	0	0
Spongotrochus glacialis	0	1	1	0	0
Stylatractus neptunus	0	0	0	0	0
***Stylodictya* spp.**	0	0	0	0	0
Tetrapyle octacantha	0	0	0	0	0
Zygocircus archicircus	0	0	1	1	0
Others	0	11	0	3	0
Total	2	348	64	116	0

Local Stations	St. LH3a-KG	St. CD4-KG	St. CD1-KG	St. 83-KG	St. 108-KG
***Acanthosphaera* spp.**	0	0	0	0	0
Actinomma antarcticum	0	0	0	0	0
Actinomma delicatulum	0	0	0	0	0
Actinomma leptoderma	0	1	1	7	0
Antarctissa denticulata	0	92	32	27	0
***Antarctissa* juvenile**	0	1	10	0	0
Antarctissa strelkovi	0	7	6	3	0
***Cenosphaera* spp.**	0	0	0	1	0
Ceratocyrtis histricosus	0	0	0	0	0
Cladoscenium ancoratum	0	0	0	0	0
***Collosphaera* sp.**	0	0	0	0	0
Cornutella profunda	0	0	0	0	0
Cycladophora bicornis	0	0	0	0	0
Cycladophora cornutoides	0	0	0	5	0
Cycladophora davisiana	0	0	0	0	0
***Dictyophims* spp.**	0	0	0	0	0
Duppatratus variabilis	0	0	0	0	0
Eucecryphalus cervus	0	0	0	0	0
Hexapyle dodecantha	0	0	0	0	0
Larcopyle buetschlii	0	3	0	9	0
Larcopyle nebulum	0	0	0	0	0
Larcopyle pylomaticus	0	1	0	0	0
Larcopyle weddelium	0	0	0	0	0
Lithelius minor	0	0	0	0	0
Lithelius nautiloides	1	1	1	0	0
***Lithocampe* spp.**	0	0	1	0	0
Lophospyris pentagona	0	0	0	0	0
Lonchosphaera spicata	0	0	0	0	0
***Lithomelissa* sp. A**	0	6	4	11	0
***Peripyramis* sp.A**	0	0	0	0	0
Peripyramis circumtexta	0	0	0	0	0
Plectcantha oikiskos	1	229	4	25	0
Phormospyris stabilis antarctica	0	0	0	0	0
Phorticium clevei	0	0	0	0	0
Plectaniscus cortiniscus	0	0	0	0	0
Pseudodictyophimus bicornis	0	0	0	0	0
Pseudodictyophimus platycephalus	0	0	0	0	0
Pseudodictyophimus gracilipes	0	0	0	0	0
Rhizoplegma boreale	0	1	1	0	0
Saccospyris antarctica	0	0	0	0	0
Saccospyris conithorax	0	0	0	0	0
Siphocampe arachnea	0	0	0	0	0
Spongodiscus biconcavus	0	0	0	0	0
Spongodiscus resurgens	0	5	2	27	0
Spongopyle osculasa	0	0	0	0	0
Spongotrochus glacialis	0	1	1	0	0
Stylatractus neptunus	0	0	0	0	0
***Stylodictya* spp.**	0	0	0	0	0
Tetrapyle octacantha	0	0	0	0	0
Zygocircus archicircus	0	0	1	1	0
Others	0	11	0	3	0
Total	2	348	64	116	0

Local Stations	GC1806	PC302	PC503	G404	G501
***Acanthosphaera* spp.**	0	0	0	0	0
Actinomma antarcticum	0	0	0	0	0
Actinomma delicatulum	0	0	0	0	0
Actinomma leptoderma	1	0	0	0	0
Antarctissa denticulata	29	0	0	0	0
***Antarctissa* juvenile**	0	0	0	0	0
Antarctissa strelkovi	0	0	0	0	0
***Cenosphaera* spp.**	0	0	0	0	0
Ceratocyrtis histricosus	0	0	0	0	0
Cladoscenium ancoratum	0	0	0	0	0
***Collosphaera* sp.**	0	0	0	0	0
Cornutella profunda	0	0	0	0	0
Cycladophora bicornis	0	0	0	0	0
Cycladophora cornutoides	3	0	0	0	0
Cycladophora davisiana	0	0	0	0	0
***Dictyophims* spp.**	0	0	0	0	0
Duppatratus variabilis	1	0	0	0	0
Eucecryphalus cervus	0	0	0	0	0
Hexapyle dodecantha	0	0	0	0	0
Larcopyle buetschlii	1	0	0	0	0
Larcopyle nebulum	0	0	0	0	0
Larcopyle pylomaticus	1	0	0	0	0
Larcopyle weddelium	0	0	0	0	0
Lithelius minor	0	0	0	0	0
Lithelius nautiloides	0	0	0	0	0
***Lithocampe* spp.**	0	0	0	0	0
Lophospyris pentagona	0	0	0	0	0
Lonchosphaera spicata	0	0	0	0	0
***Lithomelissa* sp. A**	1	0	0	0	0
***Peripyramis* sp.A**	0	0	0	0	0
Peripyramis circumtexta	0	0	0	0	0
Plectcantha oikiskos	2	0	0	0	0
Phormospyris stabilis antarctica	0	0	0	0	0
Phorticium clevei	0	0	0	0	0
Plectaniscus cortiniscus	0	0	0	0	0
Pseudodictyophimus bicornis	0	0	0	0	0
Pseudodictyophimus platycephalus	0	0	0	0	0
Pseudodictyophimus gracilipes	8	0	0	0	0
Rhizoplegma boreale	0	0	0	0	0
Saccospyris antarctica	0	0	0	0	0
Saccospyris conithorax	0	0	0	0	0
Siphocampe arachnea	0	0	0	0	0
Spongodiscus biconcavus	0	0	0	0	0
Spongodiscus resurgens	0	0	0	0	0
Spongopyle osculasa	0	0	0	0	0
Spongotrochus glacialis	0	0	0	0	0
Stylatractus neptunus	0	0	0	0	0
***Stylodictya* spp.**	0	0	0	0	0
Tetrapyle octacantha	0	0	0	0	0
Zygocircus archicircus	0	0	0	0	0
Others	2	0	0	0	0
Total	47	0	0	0	0

Local Stations	**G503**	**GC1004**	**GC1006**	**GC1301**	**GC1509**
***Acanthosphaera* spp.**	0	0	0	5	0
Actinomma antarcticum	0	0	0	0	0
Actinomma delicatulum	0	0	0	5	0
Actinomma leptoderma	0	1	0	5	0
Antarctissa denticulata	0	217	64	148	0
***Antarctissa* juvenile**	0	34	0	32	0
Antarctissa strelkovi	0	64	9	13	0
***Cenosphaera* spp.**	0	0	0	7	0
Ceratocyrtis histricosus	0	1	0	0	0
Cladoscenium ancoratum	0	0	0	2	0
***Collosphaera* sp.**	0	1	0	1	0
Cornutella profunda	0	0	0	1	0
Cycladophora bicornis	0	0	0	0	0
Cycladophora cornutoides	0	0	0	40	0
Cycladophora davisiana	0	0	0	0	0
***Dictyophims* spp.**	0	0	0	2	0
Duppatratus variabilis	0	0	0	1	0
Eucecryphalus cervus	0	0	0	0	0
Hexapyle dodecantha	0	0	0	0	0
Larcopyle buetschlii	0	10	0	34	0
Larcopyle nebulum	0	0	0	0	0
Larcopyle pylomaticus	0	0	0	3	0
Larcopyle weddelium	0	0	0	6	0
Lithelius minor	0	0	0	3	0
Lithelius nautiloides	0	0	1	1	0
***Lithocampe* spp.**	0	0	0	11	0
Lophospyris pentagona	0	0	0	0	0
Lonchosphaera spicata	0	0	0	0	0
***Lithomelissa* sp. A**	0	3	4	6	0
***Peripyramis* sp.A**	0	0	0	5	0
Peripyramis circumtexta	0	0	0	0	0
Plectcantha oikiskos	0	76	4	12	0
Phormospyris stabilis antarctica	0	0	0	3	0
Phorticium clevei	0	0	0	0	0
Plectaniscus cortiniscus	0	0	0	0	0
Pseudodictyophimus bicornis	0	0	0	1	0
Pseudodictyophimus platycephalus	0	0	0	4	0
Pseudodictyophimus gracilipes	0	0	0	17	0
Rhizoplegma boreale	0	1	0	0	0
Saccospyris antarctica	0	0	0	4	0
Saccospyris conithorax	0	0	0	0	0
Siphocampe arachnea	0	0	0	0	0
Spongodiscus biconcavus	0	0	0	2	0
Spongodiscus resurgens	0	3	0	19	0
Spongopyle osculasa	0	0	0	1	0
Spongotrochus glacialis	0	0	0	2	0
Stylatractus neptunus	0	0	0	1	0
***Stylodictya* spp.**	0	1	0	4	0
Tetrapyle octacantha	0	0	0	0	0
Zygocircus archicircus	0	0	0	8	0
Others	0	7	0	0	0
Total	0	412	82	404	0

Local Stations	GC1904	GC1905	GC2006	GC2009
***Acanthosphaera* spp.**	5	0	0	5
Actinomma antarcticum	1	0	0	14
Actinomma delicatulum	1	0	0	2
Actinomma leptoderma	3	0	0	2
Antarctissa denticulata	125	0	0	173
***Antarctissa* juvenile**	17	0	0	30
Antarctissa strelkovi	1	0	0	5
***Cenosphaera* spp.**	17	0	0	6
Ceratocyrtis histricosus	0	0	0	0
Cladoscenium ancoratum	1	0	0	5
***Collosphaera* sp.**	2	0	0	0
Cornutella profunda	2	0	0	0
Cycladophora bicornis	4	0	0	7
Cycladophora cornutoides	18	0	0	25
Cycladophora davisiana	2	0	0	2
***Dictyophims* spp.**	1	0	0	2
Duppatratus variabilis	0	0	0	0
Eucecryphalus cervus	1	0	0	1
Hexapyle dodecantha	0	0	0	0
Larcopyle buetschlii	47	0	0	19
Larcopyle nebulum	0	0	0	0
Larcopyle pylomaticus	2	0	0	0
Larcopyle weddelium	6	0	0	27
Lithelius minor	2	0	0	2
Lithelius nautiloides	1	0	0	0
***Lithocampe* spp.**	0	0	0	3
Lophospyris pentagona	1	0	0	0
Lonchosphaera spicata	0	0	0	0
***Lithomelissa* sp. A**	5	0	0	1
***Peripyramis* sp.A**	0	0	0	2
Peripyramis circumtexta	0	0	0	3
Plectcantha oikiskos	0	0	0	6
Phormospyris stabilis antarctica	2	0	0	6
Phorticium clevei	0	0	0	1
Plectaniscus cortiniscus	0	0	0	0
Pseudodictyophimus bicornis	1	0	0	0
Pseudodictyophimus platycephalus	0	0	0	1
Pseudodictyophimus gracilipes	5	0	0	7
Rhizoplegma boreale	0	0	0	0
Saccospyris antarctica	6	0	0	2
Saccospyris conithorax	0	0	0	1
Siphocampe arachnea	0	0	0	0
Spongodiscus biconcavus	0	0	0	0
Spongodiscus resurgens	20	0	0	24
Spongopyle osculasa	2	0	0	3
Spongotrochus glacialis	7	0	0	4
Stylatractus neptunus	1	0	0	0
***Stylodictya* spp.**	1	0	0	9
Tetrapyle octacantha	0	0	0	0
Zygocircus archicircus	6	0	0	15
Others	2	0	0	0
Total	311	0	0	410

Supplementary Table 6 | Radiolarian abundance (%) from surface sediments

Local Stations	St. 12B-KG	St. 14B-KG	St. 15-KG	St. 17-KG	St. 18-KG
***Acanthosphaera* spp.**	0	0	0	0	0
Actinomma antarcticum	0	0	0	0	0
Actinomma delicatulum	0	0	0	0	0
Actinomma leptoderma	0	0.3	0	0.9	0.4
Antarctissa denticulata	60.4	39.2	41.3	27.2	55.2
***Antarctissa* juvenile**	5.7	7.1	4.4	0.9	0
Antarctissa strelkovi	0	9.3	4.4	3.4	10.5
***Cenosphaera* spp.**	0	0	0	0	0
Ceratocyrtis histricosus	3.8	0	0	0.4	0
Cladoscenium ancoratum	0	0.9	0.7	0	0.4
***Collosphaera* sp.**	0	0	0	0	0
Cornutella profunda	0	0	0	0	0
Cycladophora bicornis	0	0.6	0	0	0
Cycladophora cornutoides	0	0.6	0.7	0.9	0.4
Cycladophora davisiana	0	0	0	0	0
***Dictyophims* spp.**	0	0	0	0	0
Duppatratus variabilis	0	0	0	0	0
Eucecryphalus cervus	0	0	0	0	0
Hexapyle dodecantha	0	0	0	0	0
Larcopyle buetschlii	1.9	0.6	0.7	3.9	2.4
Larcopyle nebulum	0	0	0	0	0
Larcopyle pylomaticus	0	0	0	0	0
Larcopyle weddelium	0	0	0	0	0
Lithelius minor	1.9	0	0	0	1.2
Lithelius nautiloides	0	1.2	1.3	0	2.8
***Lithocampe* spp.**	0	0.3	1.3	0.4	0
Lophospyris pentagona	0	0	0	0	0
Lonchosphaera spicata	0	0	0	0	0
***Lithomelissa* sp. A**	11.3	8.6	5.7	6.9	1.2
***Peripyramis* sp.A**	0	0	0	0	0
Peripyramis circumtexta	0	0	0	0	0
Plectcantha oikiskos	11.3	22.8	29.9	44.0	23.0
Phormospyris stabilis antarctica	0	0.3	0	1.3	0.4
Phorticium clevei	0	0	0	0	0
Plectaniscus cortiniscus	1.9	0	0	0	0
Pseudodictyophimus bicornis	0	0	0	0	0
Pseudodictyophimus platycephalus	0	0.9	0	0	0
Pseudodictyophimus gracilipes	0	0.6	0	0.4	0.4
Rhizoplegma boreale	0	1.2	0	0	0
Saccospyris antarctica	0	0	1.3	0.4	0.8
Saccospyris conithorax	0	0	0	0	0
Siphocampe arachnea	0	0	0.3	0	0
Spongodiscus biconcavus	0	0	0	0	0
Spongodiscus resurgens	0	3.7	5.0	8.2	0.8
Spongopyle osculasa	0	0	0	0	0
Spongotrochus glacialis	1.9	0.3	0	0	0
Stylatractus neptunus	0	0	0	0	0
***Stylodictya* spp.**	0	0.3	3.0	0.9	0
Tetrapyle octacantha	0	0	0	0	0
Zygocircus archicircus	0	0.9	0	0	0
Others	3.8	1.5	4.7	0	1.2

Local Stations	St. 25-KG	St. 26-KG	St. X23-KG	St. LH5a-KG	St. LH1a-KG
***Acanthosphaera* spp.**	0	0	0	0	0.5
Actinomma antarcticum	0	0	0	0	0
Actinomma delicatulum	0	0	0.4	0	0
Actinomma leptoderma	0	0	0.4	0	2.9
Antarctissa denticulata	56.3	40.9	48.5	0	48.6
***Antarctissa* juvenile**	4.7	9.1	3.3	0	4.3
Antarctissa strelkovi	14.1	20.6	1.8	0	1.4
***Cenosphaera* spp.**	0	0	0.4	0	0
Ceratocyrtis histricosus	0	0	0	0	0
Cladoscenium ancoratum	0	0	0	0	0
***Collosphaera* sp.**	0	0	1.1	0	0
Cornutella profunda	0	0	0	0	0
Cycladophora bicornis	0	0	0	0	0
Cycladophora cornutoides	0	0.6	0.7	0	2.9
Cycladophora davisiana	0	0	0	0	0
***Dictyophims* spp.**	0	0	0	0	0
Duppatratus variabilis	0	0	0	0	0
Eucecryphalus cervus	0	0	0	0	0
Hexapyle dodecantha	0	0	0	0	0
Larcopyle buetschlii	0	5.2	3.3	0	10.6
Larcopyle nebulum	0	0	0	0	0
Larcopyle pylomaticus	0	0	0	0	1.0
Larcopyle weddelium	0	0.6	0	0	1.0
Lithelius minor	0	0.9	0.4	0	1.0
Lithelius nautiloides	2.3	1.8	1.5	0	1.0
***Lithocampe* spp.**	0.8	0.9	0.4	0	0.5
Lophospyris pentagona	0	0	0	0	0
Lonchosphaera spicata	0	0	0	0	0
***Lithomelissa* sp. A**	2.3	8.2	6.2	0	1.4
***Peripyramis* sp.A**	0	0	0	0	0
Peripyramis circumtexta	0	0	0	0	0
Plectcantha oikiskos	13.3	0.3	19.3	0	0
Phormospyris stabilis antarctica	0	1.2	0	0	0.5
Phorticium clevei	0	0	0	0	0
Plectaniscus cortiniscus	0	0	0	0	0
Pseudodictyophimus bicornis	0	0.3	0	0	0
Pseudodictyophimus platycephalus	0	0	0	0	0
Pseudodictyophimus gracilipes	0	0	0	0	1.0
Rhizoplegma boreale	0	0.3	0.4	0	0.5
Saccospyris antarctica	0	0.3	0.7	0	0.5
Saccospyris conithorax	0	0	0	0	0
Siphocampe arachnea	0	0	0	0	0
Spongodiscus biconcavus	1.6	0	0	0	0
Spongodiscus resurgens	3.9	7.3	9.9	0	18.3
Spongopyle osculasa	0	0	0	0	0
Spongotrochus glacialis	0	0	0.4	0	1.0
Stylatractus neptunus	0	0	0	0	0.5
***Stylodictya* spp.**	0	0.3	0	0	0.5
Tetrapyle octacantha	0	0	0	0	0.5
Zygocircus archicircus	0.8	1.2	1.1	0	0.5
Others	0	0.9	0.4	0	0

Local Stations	**St. LH3a-KG**	**St. CD4-KG**	**St. CD1-KG**	**St. 83-KG**	**St. 108-KG**
***Acanthosphaera* spp.**	0	0	0	0	0
Actinomma antarcticum	0	0	0	0	0
Actinomma delicatulum	0	0	0	0	0
Actinomma leptoderma	0	0.3	1.6	6.0	0
Antarctissa denticulata	0	26.4	50.0	23.3	0
***Antarctissa* juvenile**	0	0.3	15.6	0	0
Antarctissa strelkovi	0	2.0	9.4	2.6	0
***Cenosphaera* spp.**	0	0	0	0.9	0
Ceratocyrtis histricosus	0	0	0	0	0
Cladoscenium ancoratum	0	0	0	0	0
***Collosphaera* sp.**	0	0	0	0	0
Cornutella profunda	0	0	0	0	0
Cycladophora bicornis	0	0	0	0	0
Cycladophora cornutoides	0	0	0	4.3	0
Cycladophora davisiana	0	0	0	0	0
***Dictyophims* spp.**	0	0	0	0	0
Duppatratus variabilis	0	0	0	0	0
Eucecryphalus cervus	0	0	0	0	0
Hexapyle dodecantha	0	0	0	0	0
Larcopyle buetschlii	0	0.9	0	7.8	0
Larcopyle nebulum	0	0	0	0	0
Larcopyle pylomaticus	0	0.3	0	0	0
Larcopyle weddelium	0	0	0	0	0
Lithelius minor	0	0	0	0	0
Lithelius nautiloides	50.0	0.3	1.6	0	0
***Lithocampe* spp.**	0	0	1.6	0	0
Lophospyris pentagona	0	0	0	0	0
Lonchosphaera spicata	0	0	0	0	0
***Lithomelissa* sp. A**	0	1.7	6.3	9.5	0
***Peripyramis* sp.A**	0	0	0	0	0
Peripyramis circumtexta	0	0	0	0	0
Plectcantha oikiskos	50.0	65.8	6.3	21.6	0
Phormospyris stabilis antarctica	0	0	0	0	0
Phorticium clevei	0	0	0	0	0
Plectaniscus cortiniscus	0	0	0	0	0
Pseudodictyophimus bicornis	0	0	0	0	0
Pseudodictyophimus platycephalus	0	0	0	0	0
Pseudodictyophimus gracilipes	0	0	0	0	0
Rhizoplegma boreale	0	0.3	1.6	0	0
Saccospyris antarctica	0	0	0	0	0
Saccospyris conithorax	0	0	0	0	0
Siphocampe arachnea	0	0	0	0	0
Spongodiscus biconcavus	0	0	0	0	0
Spongodiscus resurgens	0	1.4	3.1	23.3	0
Spongopyle osculasa	0	0	0	0	0
Spongotrochus glacialis	0	0.3	1.6	0	0
Stylatractus neptunus	0	0	0	0	0
***Stylodictya* spp.**	0	0	0	0	0
Tetrapyle octacantha	0	0	0	0	0
Zygocircus archicircus	0	0	1.6	0.9	0
Others	0	3.2	0	2.6	0

Local Stations	St. 109-KG	PC302	PC503	G404	G501
***Acanthosphaera* spp.**	0	0	3.1	0	0
Actinomma antarcticum	0.3	0	0	0.6	0
Actinomma delicatulum	0	0	1.6	0.6	0
Actinomma leptoderma	0.6	0	0.8	0.9	6.0
Antarctissa denticulata	59.5	0	44.2	32.2	45.8
***Antarctissa* juvenile**	13.6	0	3.1	2.4	0
Antarctissa strelkovi	6.3	0	5.4	3.3	0
***Cenosphaera* spp.**	0.3	0	4.7	0.3	0
Ceratocyrtis histricosus	0	0	0	0	0
Cladoscenium ancoratum	0	0	0	0	0
***Collosphaera* sp.**	0	0	0.8	0	0
Cornutella profunda	0	0	0	0.6	0
Cycladophora bicornis	0	0	0	0.3	1.2
Cycladophora cornutoides	0	0	3.9	6.0	2.4
Cycladophora davisiana	0	0	0	3.0	0
***Dictyophims* spp.**	0	0	0	0	0
Duppatratus variabilis	0	0	0.8	0	0
Eucecryphalus cervus	0	0	0	0	0
Hexapyle dodecantha	0	0	0	0	0
Larcopyle buetschlii	7.6	0	16.3	19.3	24.1
Larcopyle nebulum	0	0	0	0.3	0
Larcopyle pylomaticus	0	0	0	3.3	0
Larcopyle weddelium	0	0	0	1.8	0
Lithelius minor	0	0	0.8	0.9	1.2
Lithelius nautiloides	0.6	0	0	0.9	0
***Lithocampe* spp.**	0	0	0	2.1	1.2
Lophospyris pentagona	0	0	0	0	0
Lonchosphaera spicata	0	0	0	0	0
***Lithomelissa* sp. A**	0.9	0	0	4.2	2.4
***Peripyramis* sp.A**	0	0	0	0	1.2
Peripyramis circumtexta	0	0	0	1.8	0
Plectcantha oikiskos	5.7	0	0.8	1.2	3.6
Phormospyris stabilis antarctica	1.3	0	2.3	0.9	0
Phorticium clevei	0.3	0	0	0	0
Plectaniscus cortiniscus	0	0	0	0	0
Pseudodictyophimus bicornis	0	0	0	0.9	0
Pseudodictyophimus platycephalus	0	0	0	0	0
Pseudodictyophimus gracilipes	0	0	1.6	4.8	4.8
Rhizoplegma boreale	0	0	0	0	1.2
Saccospyris antarctica	0.3	0	2.3	0	1.2
Saccospyris conithorax	0	0	2.3	1.2	0
Siphocampe arachnea	0	0	0	0	0
Spongodiscus biconcavus	0	0	0.8	0.6	1.2
Spongodiscus resurgens	2.2	0	4.7	0	2.4
Spongopyle osculasa	0	0	0	0.3	0
Spongotrochus glacialis	0	0	0	2.4	0
Stylatractus neptunus	0	0	1.6	0	0
***Stylodictya* spp.**	0	0	0.8	2.4	0
Tetrapyle octacantha	0	0	0	0	0
Zygocircus archicircus	0.3	0	0.8	0.3	0
Others	0.9	0	0	3.0	1.2

Local Stations	G503	GC1004	GC1006	GC1301	GC1509
***Acanthosphaera* spp.**	0	0	0	0	0
Actinomma antarcticum	0	0	0	0	0
Actinomma delicatulum	0	0	0	0	0
Actinomma leptoderma	2.1	0	0	0	0
Antarctissa denticulata	61.7	0	0	0	0
***Antarctissa* juvenile**	0	0	0	0	0
Antarctissa strelkovi	0	0	0	0	0
***Cenosphaera* spp.**	0	0	0	0	0
Ceratocyrtis histricosus	0	0	0	0	0
Cladoscenium ancoratum	0	0	0	0	0
***Collosphaera* sp.**	0	0	0	0	0
Cornutella profunda	0	0	0	0	0
Cycladophora bicornis	0	0	0	0	0
Cycladophora cornutoides	6.4	0	0	0	0
Cycladophora davisiana	0	0	0	0	0
***Dictyophims* spp.**	0	0	0	0	0
Duppatratus variabilis	2.1	0	0	0	0
Eucecryphalus cervus	0	0	0	0	0
Hexapyle dodecantha	0	0	0	0	0
Larcopyle buetschlii	2.1	0	0	0	0
Larcopyle nebulum	0	0	0	0	0
Larcopyle pylomaticus	2.1	0	0	0	0
Larcopyle weddelium	0	0	0	0	0
Lithelius minor	0	0	0	0	0
Lithelius nautiloides	0	0	0	0	0
***Lithocampe* spp.**	0	0	0	0	0
Lophospyris pentagona	0	0	0	0	0
Lonchosphaera spicata	0	0	0	0	0
***Lithomelissa* sp. A**	2.1	0	0	0	0
***Peripyramis* sp.A**	0	0	0	0	0
Peripyramis circumtexta	0	0	0	0	0
Plectcantha oikiskos	4.3	0	0	0	0
Phormospyris stabilis antarctica	0	0	0	0	0
Phorticium clevei	0	0	0	0	0
Plectaniscus cortiniscus	0	0	0	0	0
Pseudodictyophimus bicornis	0	0	0	0	0
Pseudodictyophimus platycephalus	0	0	0	0	0
Pseudodictyophimus gracilipes	17.0	0	0	0	0
Rhizoplegma boreale	0	0	0	0	0
Saccospyris antarctica	0	0	0	0	0
Saccospyris conithorax	0	0	0	0	0
Siphocampe arachnea	0	0	0	0	0
Spongodiscus biconcavus	0	0	0	0	0
Spongodiscus resurgens	0	0	0	0	0
Spongopyle osculasa	0	0	0	0	0
Spongotrochus glacialis	0	0	0	0	0
Stylatractus neptunus	0	0	0	0	0
***Stylodictya* spp.**	0	0	0	0	0
Tetrapyle octacantha	0	0	0	0	0
Zygocircus archicircus	0	0	0	0	0
Others	4.3	0	0	0	0

Local Stations	GC1903	GC1904	GC1905	GC1906	GC2001
***Acanthosphaera* spp.**	0	0	0	1.2	0
Actinomma antarcticum	0	0	0	0	0
Actinomma delicatulum	0	0	0	1.2	0
Actinomma leptoderma	0	0.2	0	1.2	0
Antarctissa denticulata	0	52.7	78.0	36.6	0
***Antarctissa* juvenile**	0	8.3	0	7.9	0
Antarctissa strelkovi	0	15.5	11.0	3.2	0
***Cenosphaera* spp.**	0	0	0	1.7	0
Ceratocyrtis histricosus	0	0.2	0	0	0
Cladoscenium ancoratum	0	0	0	0.5	0
***Collosphaera* sp.**	0	0.2	0	0.2	0
Cornutella profunda	0	0	0	0.2	0
Cycladophora bicornis	0	0	0	0	0
Cycladophora cornutoides	0	0	0	9.9	0
Cycladophora davisiana	0	0	0	0	0
***Dictyophims* spp.**	0	0	0	0.5	0
Duppatratus variabilis	0	0	0	0.2	0
Eucecryphalus cervus	0	0	0	0	0
Hexapyle dodecantha	0	0	0	0	0
Larcopyle buetschlii	0	2.4	0	8.4	0
Larcopyle nebulum	0	0	0	0	0
Larcopyle pylomaticus	0	0	0	0.7	0
Larcopyle weddelium	0	0	0	1.5	0
Lithelius minor	0	0	0	0.7	0
Lithelius nautiloides	0	0	1.2	0.2	0
***Lithocampe* spp.**	0	0	0	2.7	0
Lophospyris pentagona	0	0	0	0	0
Lonchosphaera spicata	0	0	0	0	0
***Lithomelissa* sp. A**	0	0.7	4.9	1.5	0
***Peripyramis* sp.A**	0	0	0	1.2	0
Peripyramis circumtexta	0	0	0	0	0
Plectcantha oikiskos	0	18.4	4.9	3.0	0
Phormospyris stabilis antarctica	0	0	0	0.7	0
Phorticium clevei	0	0	0	0	0
Plectaniscus cortiniscus	0	0	0	0	0
Pseudodictyophimus bicornis	0	0	0	0.2	0
Pseudodictyophimus platycephalus	0	0	0	1.0	0
Pseudodictyophimus gracilipes	0	0	0	4.2	0
Rhizoplegma boreale	0	0.2	0	0	0
Saccospyris antarctica	0	0	0	1.0	0
Saccospyris conithorax	0	0	0	0	0
Siphocampe arachnea	0	0	0	0	0
Spongodiscus biconcavus	0	0	0	0.5	0
Spongodiscus resurgens	0	0.7	0	4.7	0
Spongopyle osculasa	0	0	0	0.2	0
Spongotrochus glacialis	0	0	0	0.5	0
Stylatractus neptunus	0	0	0	0.2	0
***Stylodictya* spp.**	0	0.2	0	1.0	0
Tetrapyle octacantha	0	0	0	0	0
Zygocircus archicircus	0	0	0	2.0	0
Others	0	1.7	0	0	0

Local Stations	GC2003	GC2005	GC2006	GC2009
***Acanthosphaera* spp.**	1.6	0	0	1.2
Actinomma antarcticum	0.3	0	0	3.4
Actinomma delicatulum	0.3	0	0	0.5
Actinomma leptoderma	1.0	0	0	0.5
Antarctissa denticulata	40.2	0	0	42.2
***Antarctissa* juvenile**	5.5	0	0	7.3
Antarctissa strelkovi	0.3	0	0	1.2
***Cenosphaera* spp.**	5.5	0	0	1.5
Ceratocyrtis histricosus	0	0	0	0
Cladoscenium ancoratum	0.3	0	0	1.2
***Collosphaera* sp.**	0.6	0	0	0
Cornutella profunda	0.6	0	0	0
Cycladophora bicornis	1.3	0	0	1.7
Cycladophora cornutoides	5.8	0	0	6.1
Cycladophora davisiana	0.6	0	0	0.5
***Dictyophims* spp.**	0.3	0	0	0.5
Duppatratus variabilis	0	0	0	0
Eucecryphalus cervus	0.3	0	0	0.2
Hexapyle dodecantha	0	0	0	0
Larcopyle buetschlii	15.1	0	0	4.6
Larcopyle nebulum	0	0	0	0
Larcopyle pylomaticus	0.6	0	0	0
Larcopyle weddelium	1.9	0	0	6.6
Lithelius minor	0.6	0	0	0.5
Lithelius nautiloides	0.3	0	0	0
***Lithocampe* spp.**	0	0	0	0.7
Lophospyris pentagona	0.3	0	0	0
Lonchosphaera spicata	0	0	0	0
***Lithomelissa* sp. A**	1.6	0	0	0.2
***Peripyramis* sp.A**	0	0	0	0.5
Peripyramis circumtexta	0	0	0	0.7
Plectcantha oikiskos	0	0	0	1.5
Phormospyris stabilis antarctica	0.6	0	0	1.5
Phorticium clevei	0	0	0	0.2
Plectaniscus cortiniscus	0	0	0	0
Pseudodictyophimus bicornis	0.3	0	0	0
Pseudodictyophimus platycephalus	0	0	0	0.2
Pseudodictyophimus gracilipes	1.6	0	0	1.7
Rhizoplegma boreale	0	0	0	0
Saccospyris antarctica	1.9	0	0	0.5
Saccospyris conithorax	0	0	0	0.2
Siphocampe arachnea	0	0	0	0
Spongodiscus biconcavus	0	0	0	0
Spongodiscus resurgens	6.4	0	0	5.9
Spongopyle osculasa	0.6	0	0	0.7
Spongotrochus glacialis	2.3	0	0	1.0
Stylatractus neptunus	0.3	0	0	0
***Stylodictya* spp.**	0.3	0	0	2.2
Tetrapyle octacantha	0	0	0	0
Zygocircus archicircus	1.9	0	0	3.7
Others	0.6	0	0	0

Supplementary data for Chapter 3

Supplementary Figure 1 | Radiolarian abundance (%) in the core GC1407

Age (kyr)	*Acanthosphaera* spp.	*Actinomma* sp. A	*Actinomma antarctica*	*Actinomma leptderma*
117.1	0.3	0	0.3	0
117.9	0	0	1.6	0
118.2	0	0	0.9	1.2
118.5	1.3	0	0.3	0
118.8	0	0	0.9	1.4
119.0	0	0	0	0
119.3	0.3	0	2.0	1.0
119.6	0.3	0	2.7	0.9
119.9	1.9	0	0	0.3
120.2	0	0	1.0	1.0
120.5	0	0	0	0
120.8	0	0	0.3	1.3
121.1	0	0	1.7	0
121.3	0	0	0	0.6
121.6	0.3	0	0	1.7
121.9	0.3	0	0	0
122.2	0	0	0.3	2.0
122.5	0	0	1.6	2.3
122.8	0	0	1.4	1.4
123.1	0	0	0.3	1.6
123.4	0	0	0.3	0
123.6	0.3	0	0	1.0
123.9	0.3	0.6	0	1.2
124.2	0	0	1.3	1.3
124.5	0.4	0	0.4	2.2
124.8	0	0	3.8	0
125.1	0	0	0	3.5
125.4	0	1.0	0	3.8
125.7	0	0	0.3	3.2
125.9	0.3	0.3	1.3	2.3
126.2	0.3	0	1.2	0
126.5	0.6	0	1.0	2.2
126.8	0.6	0	1.3	2.9
127.1	0.3	0	2.0	2.3
127.4	0	0	0.3	4.7
127.7	0.3	0	2.6	0
127.9	0	1.0	1.0	2.3
128.2	0	0	0.3	1.9
128.5	0	0	0	2.8
128.8	0.7	0	1.0	0
129.1	0.7	0	1.4	0
130.5	0.4	0	0.7	0

Age (kyr)	*Actinomma boreale*	*Actinommma delicatum*	*Antarctissa denticulata*	*Antarctissa cyrindrica*
117.1	0.3	0	42.6	0
117.9	0.3	0	49.4	0.3
118.2	0.9	0	50.2	0.6
118.5	0.3	0	50.6	0.9
118.8	0.3	0	59.4	1.4
119.0	2.7	0	63.5	0
119.3	1.0	0	49.7	0.7
119.6	0.6	0	52.6	0
119.9	0.3	0	57.0	0.9
120.2	0.3	0	53.7	2.9
120.5	0.6	0	53.1	0
120.8	0	0	45.5	1.0
121.1	4.0	0	53.3	0
121.3	0.3	0	46.6	0.3
121.6	0	0	54.3	1.0
121.9	1.6	0	62.6	0
122.2	0	0	63.2	0
122.5	1.0	0	63.4	1.0
122.8	1.4	0	69.4	1.0
123.1	1.3	1.0	51.6	0.3
123.4	3.2	0	49.0	0
123.6	1.0	0	49.3	1.0
123.9	0.3	0	63.3	0.6
124.2	1.0	1.3	64.3	1.3
124.5	0.7	0	61.1	0
124.8	3.5	0	53.5	0
125.1	0.3	1.9	63.5	0.3
125.4	1.3	0.3	48.9	0.3
125.7	0	0	56.3	0
125.9	0	0	54.9	0
126.2	3.7	0	54.4	0
126.5	0	1.0	48.7	0
126.8	0.3	0	47.0	0.6
127.1	0.7	0	45.6	0.7
127.4	0.3	0	47.7	0.7
127.7	4.2	0	47.2	0
127.9	0.6	0.3	51.0	0
128.2	0.3	0	49.8	0
128.5	0.6	0.6	45.6	0.9
128.8	0	0	47.5	0
129.1	0	0	45.1	0
130.5	0	0	54.6	0

Age (kyr)	*Antarctissa strelkovi*	*Antarctissa* juvenile	*Antarctissa* spp.	*Botryocampe antarctica*
117.1	1.5	20.1	181.3	0.3
117.9	0	13.8	181.3	0
118.2	0.3	8.8	178.1	0
118.5	0	7.5	177.6	0
118.8	0.6	8.0	188.2	0
119.0	0.6	6.0	189.1	2.1
119.3	0.7	8.3	178.7	0
119.6	0	9.3	181.5	0
119.9	0	10.3	188.1	0
120.2	0.7	9.1	186.6	0
120.5	3.2	8.0	184.8	1.9
120.8	0.3	11.0	178.5	0
121.1	1.3	6.3	182.1	0
121.3	1.0	12.3	181.5	0
121.6	0	14.6	191.5	0
121.9	2.0	8.5	195.0	0.3
122.2	0.7	4.9	190.9	0
122.5	0.7	5.2	192.8	0
122.8	0	4.1	197.3	0
123.1	1.6	7.9	184.6	0
123.4	1.9	15.7	190.0	0.3
123.6	1.6	9.5	185.2	0
123.9	1.8	3.6	193.2	0
124.2	0.6	3.2	193.7	0
124.5	2.6	2.2	190.4	0
124.8	3.2	6.7	188.3	0.3
125.1	1.6	7.7	198.2	0
125.4	0.3	6.7	181.6	0
125.7	1.0	6.8	189.6	0
125.9	0.3	1.9	183.1	0
126.2	1.2	8.3	190.1	0.9
126.5	1.6	6.7	183.5	0
126.8	0.3	8.3	183.0	0
127.1	0.7	7.2	181.2	0
127.4	3.4	8.1	187.1	0
127.7	2.6	8.7	186.2	0
127.9	2.9	7.1	189.0	0
128.2	1.3	6.5	185.8	0
128.5	1.6	4.7	181.4	0
128.8	0	6.1	182.4	0
129.1	1.1	4.6	179.8	0.7
130.5	1.1	5.2	191.5	1.9

Age (kyr)	*Botryocampe conithorax*	*Botryopyle cribrosa*	*Botryostrobus aquilonaria*	*Botryostrobus australis*
117.1	0.3	0.3	0	0
117.9	0	0	0	0.9
118.2	0	0	0	0
118.5	0	0	0	0.6
118.8	0	0	0	0
119.0	0.6	0	0	0
119.3	0	0	0	0.3
119.6	0	0	0	0
119.9	0	0	0	0
120.2	0	0	0	0
120.5	0	0	0.3	1.0
120.8	0	0	0.3	0
121.1	0.7	0	0	0
121.3	0	0	0.3	0
121.6	0	0	0.3	0
121.9	0	0	0.3	0
122.2	0	0	0	0
122.5	0	0	0	0
122.8	0	0	0	0
123.1	0	0	0.7	0
123.4	0	0	0	0
123.6	0	0	0	0
123.9	0	0	0	0
124.2	0	0	0	0
124.5	0	0	0.4	0
124.8	0.3	0	0.3	0
125.1	0	0	0.3	0
125.4	0	0	0	0
125.7	0	0	0.3	0
125.9	0	0	0	0
126.2	0	0	0.6	0
126.5	0	0	0.6	0
126.8	0	0	0	0
127.1	0	0	0	0
127.4	0	0	0.3	0
127.7	0.3	0	0.3	0.6
127.9	0	0	0.3	0
128.2	0	0	0	0
128.5	0	0	1.3	0
128.8	0	0	0	0
129.1	0	0	0.4	0.7
130.5	0	0	0.7	0

Age (kyr)	*Cenosphera* spp.	*Ceratocyrtis historicosus*	*Cornutella profunda*	*Cladoscenium ancoratum*
117.1	0	0	0	0
117.9	0.3	0	0.3	0
118.2	0.3	0	0.3	0
118.5	1.3	0	0	0
118.8	0.3	0	0.3	0
119.0	0	0	0	0
119.3	0.7	0	0	0
119.6	0	0	0	0
119.9	1.6	0	0.6	0
120.2	0	0	0	0
120.5	1.9	0	0	0
120.8	0	0	0	0
121.1	1.3	0	0.3	0
121.3	0	0	0	0
121.6	0	0	0	0
121.9	2.6	0	0	0
122.2	0.7	0	0.3	0
122.5	0.3	0	0.3	0
122.8	0	0	0	0
123.1	0	0	0.3	0
123.4	0	0	0	0
123.6	0.3	0	0	0
123.9	0	0	0	0
124.2	0	0	0	0
124.5	0	0	0	0
124.8	0	0	0.6	0
125.1	0	0	0	0
125.4	0	0	0.3	0
125.7	0	0	0.3	0
125.9	0	0	0	0
126.2	0	0	0	0.3
126.5	0	0	0	0
126.8	0.3	0	0.3	0
127.1	0	0	1.0	0
127.4	0.3	0	0	0
127.7	1.3	0.3	0.6	0.3
127.9	0	0	0	0
128.2	0	0	0.3	0
128.5	0	0	0.3	0
128.8	0	0	0.3	0
129.1	0.4	0.4	0	0
130.5	0	0	0.4	0.4

Age (kyr)	*Collosphaera* spp.	*Cycladophora bicornis*	*Cycladophora cornutoides*	*Cycladophora davisiana*
117.1	0	0.6	0	6.5
117.9	0.6	0	1.3	0.6
118.2	0.6	0	0	1.2
118.5	0	0	0.3	3.8
118.8	1.1	0	0	2.3
119.0	0	0.6	0	1.8
119.3	0	0	0	4.7
119.6	0	0	0	2.7
119.9	0.3	0	0.3	2.2
120.2	0	0.3	0.3	2.3
120.5	0	0.3	0	8.4
120.8	1.0	0	0.3	0.3
121.1	0	0.3	0	3.3
121.3	0	0.3	0	3.2
121.6	0.7	0.3	0	2.3
121.9	0	0	0	4.9
122.2	0	0	0.3	2.6
122.5	0.3	0.3	0.3	0.3
122.8	1.4	0	0	0.7
123.1	0	0.3	0.7	1.3
123.4	0	0	0.3	1.0
123.6	0.3	0.7	0.3	0.7
123.9	0.3	0	0.9	0.6
124.2	0	0.6	0.3	0
124.5	0	2.2	0	0.4
124.8	0	0.3	1.3	2.9
125.1	0	0.6	0.3	0.3
125.4	0.3	0.3	0.3	0
125.7	0.6	1.3	0	1.0
125.9	0	0.6	0.6	1.3
126.2	0	0.9	0.3	1.2
126.5	0.3	0.6	0	0.6
126.8	0	1.0	1.3	1.6
127.1	0.3	0.3	0	0
127.4	0	0	1.3	0.7
127.7	0	1.6	0.3	0
127.9	0	0.3	0.3	0.3
128.2	1.0	1.3	1.9	0.6
128.5	0.3	2.2	0.6	0
128.8	1.0	2.7	1.0	0
129.1	0	2.5	0.4	0.7
130.5	0.4	2.2	0.7	1.1

Age (kyr)	*Cromychinus antarctica*	*Cyrtopera aglaompa*	*Dictyophimus* spp.	*Druppatractus irregularis*
117.1	0	0	0	0.6
117.9	0	0	0.6	0
118.2	0	0	0.3	0
118.5	0	0	0	0
118.8	0	0	0	0
119.0	0	0	0	0
119.3	0	0	0	0
119.6	0	0	0	0
119.9	0	0	0	0
120.2	0	0	0	0
120.5	0	0	0	0
120.8	0	0	0	0
121.1	0	0	0	0
121.3	0	0	0.6	0
121.6	0	0	0.3	0
121.9	0	0	0.3	0
122.2	0	0	0.3	0
122.5	0	0	0	0
122.8	0	0	0	0
123.1	0	0	0.3	0
123.4	0	0	0	0
123.6	0	0	0.3	0
123.9	0	0	0.3	0
124.2	0	0	0	0
124.5	0	0	0	0
124.8	1.0	0.3	0.3	0
125.1	0	0	0	0
125.4	0	0	1.0	0
125.7	0	0	0	0
125.9	0	0	0	0
126.2	0	0	0	0
126.5	0	0	0	0
126.8	0	0	0	0
127.1	0	0	0	0
127.4	0	0	0	0
127.7	0	0.3	0	0.6
127.9	0	0	0	0
128.2	0	0	0	0
128.5	0	0	0	0
128.8	0	0	0	0
129.1	1.1	0	0.4	0
130.5	1.1	1.1	0	0.7

Age (kyr)	*Eucyrtidium teuscheri*	*Hexacontium* spp.	*Larcopyle* juvneil	*Larcopyle buetschii*
117.1	0	0	1.2	4.3
117.9	0	0	1.3	6.9
118.2	0	0	0	14.3
118.5	0	0	0.9	9.4
118.8	0	0	0	8.0
119.0	0	0	0	10.8
119.3	0	0	0	8.3
119.6	0	0	0	7.5
119.9	0	0	0	3.4
120.2	0	0	0	5.5
120.5	0	0	0	7.7
120.8	0	0	0	10.0
121.1	0	0	1.0	8.3
121.3	0	0	0.3	7.8
121.6	0	0	0.7	6.3
121.9	0	0	0	3.0
122.2	0	0	0.3	9.8
122.5	0	0	0	6.2
122.8	0	0	0	4.8
123.1	0	0	0	8.2
123.4	0	0	0	4.8
123.6	0	0	0	5.3
123.9	0	0	0	6.9
124.2	0	0	0	7.5
124.5	0	0	0	5.2
124.8	0	0	1.3	4.8
125.1	0	0	0	3.8
125.4	0	0	0	4.8
125.7	0	0	1.0	5.1
125.9	0	0	1.9	8.4
126.2	0	0	0.3	10.1
126.5	0	0	0	6.4
126.8	0	0	0.6	7.9
127.1	0	0	0	4.3
127.4	0	0	0.7	6.7
127.7	0	0.6	1.3	9.4
127.9	0	0	2.3	3.2
128.2	0	0	0.6	8.1
128.5	0	0	1.6	5.7
128.8	0	0	0	7.8
129.1	0.4	0	3.5	9.5
130.5	0.4	0	1.1	7.4

Age (kyr)	*Larcopyle pylomaticus*	*Larcopyle weddelium*	*Larcopyle neblum*	*Lithelius minor*
117.1	1.2	2.5	0.3	1.5
117.9	3.1	5.3	0	1.6
118.2	2.4	3.0	0	1.2
118.5	1.3	5.0	0	0.9
118.8	0.6	3.4	0	1.1
119.0	0	0.9	0	0.6
119.3	0.7	2.7	0	2.3
119.6	0.9	4.2	0	0.3
119.9	0.6	1.9	0	0.9
120.2	0.3	4.9	0	0.7
120.5	1.3	3.5	0	0.6
120.8	1.0	6.5	0	0
121.1	2.3	1.7	0	1.0
121.3	2.6	3.6	0	1.6
121.6	1.7	2.6	0	0.3
121.9	1.3	1.6	0	0.3
122.2	1.0	1.0	0	1.6
122.5	1.6	3.6	0	1.0
122.8	0.7	2.4	0	0.3
123.1	1.6	3.9	0	0
123.4	1.0	3.5	0	0.6
123.6	1.6	6.6	0	1.0
123.9	1.8	7.8	0	0.6
124.2	0.6	6.2	0	0
124.5	1.1	8.9	0	0.7
124.8	0.6	1.3	0	1.0
125.1	0.6	3.8	0	0.3
125.4	0.3	7.3	0	3.5
125.7	1.3	4.8	0	1.3
125.9	1.6	8.1	0	2.6
126.2	0.3	2.1	0	0
126.5	0.6	7.0	0	1.3
126.8	1.6	9.5	0	0.6
127.1	2.6	5.9	0.3	2.6
127.4	2.0	6.0	0	1.3
127.7	0.6	2.3	0	0.6
127.9	1.6	6.2	0	0
128.2	0.3	6.5	0	1.0
128.5	0	5.3	0	0
128.8	0.7	5.8	0	0.7
129.1	1.1	0.7	0.4	1.4
130.5	1.5	1.5	0	1.5

Age (kyr)	*Lithelius nautoloides*	*Lithocampe furcaspiculata*	*Lithocampe platycephala*	*Lithomelissa setosa*
117.1	1.2	0	1.9	0
117.9	0.9	0	0	0
118.2	0.6	1.5	0	0
118.5	0.9	0	0	0
118.8	0.9	0.3	0	0
119.0	1.2	0.3	1.2	0
119.3	0	0	0	0
119.6	0.3	0.9	0	0
119.9	0.3	0	0	0
120.2	0.3	0	0	0
120.5	1.0	0	0.3	0
120.8	1.3	0.3	0.3	0
121.1	0	0	0	0
121.3	1.0	0.3	0	0
121.6	1.0	0	0	0
121.9	1.3	0	0.7	0
122.2	0	1.6	0.3	0
122.5	1.0	0	0	0
122.8	0.3	0	0	0
123.1	1.0	1.3	0.7	0
123.4	1.0	0	1.3	0
123.6	1.6	1.6	1.0	0
123.9	0.3	0.9	0	0
124.2	0	0.6	1.3	0
124.5	0	0.4	0	0
124.8	0	0	1.3	0
125.1	1.0	0.3	0	0
125.4	1.0	1.0	0	0
125.7	0.3	1.0	0	0.3
125.9	0.3	1.0	0	0
126.2	0.3	0	0.9	0
126.5	1.3	0.3	0	0
126.8	1.0	1.0	0	0
127.1	0.7	0.3	0	0
127.4	0.3	0.3	0	0
127.7	0.3	0	1.0	0
127.9	0.3	2.9	0	0
128.2	0	1.0	0	0
128.5	0.6	2.5	1.3	0
128.8	0.7	2.0	0.3	0
129.1	0.4	0	1.1	0
130.5	0	0.7	1.1	0

Age (kyr)	*Lithomelissa* sp.A	*Peripyramis circumtexta*	*Phormospyris stabilis antarctica*	*Phorticium clevi*
117.1	0.9	0.9	0.3	0
117.9	0.9	0	0.6	0
118.2	0.9	0	0.3	0
118.5	0.9	0	0.3	0
118.8	0.3	0	0.9	0
119.0	0.6	0	0	0
119.3	2.3	0	1.0	0
119.6	0.9	0.6	0.9	0
119.9	1.9	0	0.9	0
120.2	1.0	0.7	1.0	0
120.5	1.6	0	1.0	0
120.8	2.9	0	0.3	0
121.1	0.3	0.3	0	0
121.3	1.3	0	1.0	0
121.6	1.3	0	1.0	0
121.9	0.3	1.0	1.0	0
122.2	0	0	0.7	0
122.5	0	0	0.3	0
122.8	0.3	0	0.7	0
123.1	1.0	0.3	1.0	0
123.4	1.9	0	0.6	0
123.6	3.0	0	0.7	0
123.9	1.2	0.3	0.6	0
124.2	1.3	0	0.3	0
124.5	0.7	0	1.1	0.4
124.8	1.3	0	1.3	0
125.1	0.3	0	1.3	0
125.4	0.3	0	1.0	0
125.7	0.3	0	1.9	0
125.9	0	0	0.3	0
126.2	1.5	0	0	0.3
126.5	0.3	0	0.6	0
126.8	0.6	0	1.0	0
127.1	0	0	0.3	0
127.4	0.7	0	0	0
127.7	1.9	0	1.0	0.3
127.9	0	0	1.0	0
128.2	0.3	0	1.3	0
128.5	0.3	0	1.3	0
128.8	0	0	0	0
129.1	1.1	0	1.4	0.4
130.5	1.1	0.4	0.7	0

Age (kyr)	*Pseudodictyophimus bicornis*	*Pseudodictyophimus gracilipes*	*Pseudodictyophimus histricosus*
117.1	0.3	0.3	0
117.9	0	0	0
118.2	0	0.3	0
118.5	0	0	0
118.8	0	0	0
119.0	0	0	0
119.3	0	1.3	0
119.6	0	0.3	0
119.9	0	0	0
120.2	0	0	0
120.5	0	0.3	0
120.8	0.3	0.3	0
121.1	0.3	0.3	0
121.3	1.0	1.0	0
121.6	0	0.7	0
121.9	0	0.7	0
122.2	0.7	0	0
122.5	0.3	0.3	0
122.8	0	0	0
123.1	0.3	1.3	0
123.4	1.3	2.2	0.3
123.6	0.3	0.3	0
123.9	0	0	0
124.2	0	0.3	0.3
124.5	0	0.7	0
124.8	0.6	2.2	0
125.1	0	1.0	0
125.4	0	0.6	0
125.7	1.9	1.9	0
125.9	0	0	0
126.2	0.6	1.2	0
126.5	1.3	0.3	0
126.8	0.3	0.3	0
127.1	0.7	1.3	0
127.4	1.7	0.3	0
127.7	0	1.9	0
127.9	1.0	1.0	0.3
128.2	1.0	0.6	1.0
128.5	0	1.3	1.6
128.8	0	0	0
129.1	0.7	1.1	0
130.5	2.6	1.5	0

Age (kyr)	*Pterocorys zancleus*	*Saccospyris antarctica*	*Saccospyris inflata*	*Sethoconus dogieli*
117.1	0.3	0	0	0
117.9	0	2.5	0.3	0
118.2	0	0.9	0.3	0
118.5	0	0.3	0	0
118.8	0	0.3	0	0
119.0	0	0	0	0
119.3	0	0.3	0.3	0
119.6	0	1.2	0	0
119.9	0	0.3	0	0
120.2	0	0	0.7	0
120.5	0	0	0	0
120.8	0	0	0	0
121.1	0	0	0	0
121.3	0	0.6	0	0
121.6	0	0.7	0	0
121.9	0	0	0	0
122.2	0	1.0	0	0
122.5	0	0	0	0
122.8	0	0.7	0	0
123.1	0	1.0	0	0
123.4	0	0	0	0
123.6	0	1.3	0	0
123.9	0	1.2	0	0
124.2	0	1.0	0	0
124.5	0	0.4	0	0
124.8	0.6	0	0	0.3
125.1	0	0	0	0
125.4	0	0.3	0	0
125.7	0	0.3	0	0
125.9	0	0.6	0	0
126.2	0.3	0	0	0
126.5	0	0	0	0
126.8	0	0.3	0.3	0
127.1	0	0.7	0	0
127.4	0	0	0	0
127.7	0	0	0	0
127.9	0	0.3	0	0
128.2	0	2.3	0	0
128.5	0	0.9	0	0
128.8	0	0	0	0
129.1	0.7	0	0	0
130.5	1.5	0	0	0

Age (kyr)	*Siphocampe arachnea*	*Spongodiscus resurgens*	*Spongopyle osculosa*	*Spongotrochus glacialis*
117.1	0	3.1	0.3	0.3
117.9	0	4.4	1.3	0
118.2	0	3.3	2.1	0.9
118.5	0	2.2	0.9	2.2
118.8	0	1.7	1.1	0.3
119.0	0	4.2	0.6	0.6
119.3	0	3.0	1.3	0.3
119.6	0	4.2	1.5	0.3
119.9	0	4.4	1.2	0.3
120.2	0	4.6	2.9	0.3
120.5	0	1.9	0.3	0
120.8	0.3	1.9	2.3	0
121.1	0	5.7	0	0.3
121.3	0	2.3	1.9	0.3
121.6	0	5.0	0	0
121.9	0	2.3	0.3	0
122.2	0	2.3	0.7	0.3
122.5	0	1.6	2.0	0.7
122.8	0	2.7	2.7	0
123.1	0	3.3	2.0	0
123.4	0	3.2	1.0	1.3
123.6	0	2.0	2.0	0
123.9	0	1.8	0.9	0.9
124.2	1.0	0	1.3	1.9
124.5	0	3.3	0.4	0.7
124.8	0.3	1.9	0.3	0.6
125.1	0	2.6	0	0.3
125.4	0	7.0	0.3	0.6
125.7	0	2.9	0	0.6
125.9	0	2.6	2.6	1.0
126.2	0.3	2.1	1.5	0.9
126.5	0.3	2.2	2.5	1.3
126.8	0	3.5	1.3	0.3
127.1	0	7.5	3.9	0.3
127.4	0	3.4	1.3	0.3
127.7	1.0	1.6	0.6	1.3
127.9	0	2.6	2.6	0.6
128.2	0	4.5	1.3	0.3
128.5	0	6.0	2.2	0
128.8	0.3	7.1	3.7	1.4
129.1	0.4	6.7	1.8	0
130.5	0	0	0.4	0

Age (kyr)	*Stylodictya acculeata*	*Stylodictya validspina*	*Stylatractus neptunus*
117.1	0.6	0	0.6
117.9	0.3	0.6	0
118.2	0	0.3	0.6
118.5	1.3	0	1.3
118.8	0.6	0	0.3
119.0	0.9	0	0
119.3	0	0	0.3
119.6	0.3	0	1.8
119.9	0	0	1.6
120.2	0	0	1.3
120.5	0.3	0	0
120.8	0.3	0	0
121.1	0	0.3	1.3
121.3	0	0	0.3
121.6	0	0	0
121.9	0.3	0	0
122.2	0	0	0
122.5	0	0	0.3
122.8	0.3	0	0.3
123.1	0.3	0	0.3
123.4	0.6	0	0
123.6	0.3	0	0.7
123.9	0	0	0
124.2	0.3	0	0
124.5	1.1	0	0
124.8	0	0	0.3
125.1	0	0	1.3
125.4	0.3	0	0.3
125.7	0.6	0	0.3
125.9	0	0	0
126.2	0	0.9	0
126.5	0.6	0	1.6
126.8	0	0	0
127.1	0.3	0	0.3
127.4	1.3	0	0.7
127.7	0	0	0.3
127.9	0	0	0.3
128.2	0.3	0.3	0.6
128.5	0.6	0.3	0
128.8	0.7	0	0
129.1	0	0	0.4
130.5	0.4	1.5	0.4

Age (kyr)	*Stylochlamidium venustum*	*Zygocircus productus*	Others
117.1	0	1.9	0
117.9	0	0	0
118.2	0	0	1.2
118.5	0	0	6.3
118.8	0	0	4.3
119.0	0.3	0	0
119.3	0	0.7	6.0
119.6	0	0.6	4.2
119.9	0	0.3	6.2
120.2	0	1.3	2.9
120.5	0	0	1.3
120.8	0	0.6	10.0
121.1	0	0.7	3.3
121.3	0	0	7.4
121.6	0	0	3.0
121.9	0	0	2.3
122.2	0	0	3.6
122.5	0	0	3.9
122.8	0	0	3.1
123.1	0	0	3.0
123.4	0	0	3.5
123.6	0	1.3	3.0
123.9	0	0	0.9
124.2	0	0	0.6
124.5	0	0	2.2
124.8	0	0	1.3
125.1	0	0	2.9
125.4	0	0	6.7
125.7	0	0.3	2.6
125.9	0	0	4.9
126.2	0	0	2.8
126.5	0	0.6	7.3
126.8	0	0	4.1
127.1	0	0.3	6.6
127.4	0	0	5.0
127.7	0	0	1.3
127.9	0	0	6.2
128.2	0	0	3.2
128.5	0.3	0.3	6.3
128.8	0	0	8.5
129.1	0.4	0	6.7
130.5	0	0	1.5

Supplementary Figure 2 | Radiolarian CDW index in the core GC1407

Age (ka)	AASW	CDW	CDW/AASW+CDW (Radiolarian CDW index)
0.0	56.6	13.5	0.19
0.6	72.7	10.6	0.13
1.2	74.7	16.1	0.18
1.8	62.2	18.9	0.23
2.5	57.4	13.6	0.19
3.1	55.5	10.1	0.15
3.7	58.3	15.2	0.21
4.3	66.8	16.9	0.20
4.9	54.7	16.0	0.23
9.2	65.2	16.7	0.20
13.0	59.3	22.5	0.28
17.6	59.3	18.6	0.24
117.1	46.0	17.9	0.28
117.9	53.8	17.5	0.25
118.2	53.8	23.7	0.31
118.5	55.3	21.7	0.28
118.8	63.7	15.7	0.20
119.0	65.9	14.1	0.18
119.3	52.7	20.3	0.28
119.6	55.3	18.3	0.25
119.9	59.8	11.2	0.16
120.2	59.0	17.9	0.23
120.5	58.2	23.5	0.29
120.8	48.4	21.0	0.30
121.1	55.0	18.3	0.25
121.3	50.8	20.1	0.28
121.6	57.9	13.6	0.19
121.9	66.9	15.4	0.19
122.2	65.8	15.6	0.19
122.5	67.0	14.4	0.18
122.8	72.1	11.2	0.13
123.1	56.6	18.8	0.25
123.4	53.8	13.5	0.20
123.6	55.6	18.1	0.25

123.9	68.7	18.4	0.21
124.2	69.5	15.9	0.19
124.5	65.9	16.7	0.20
124.8	58.7	12.2	0.17
125.1	67.9	9.6	0.12
125.4	52.4	13.3	0.20
125.7	60.5	14.5	0.19
125.9	57.5	22.1	0.28
126.2	56.9	16.5	0.23
126.5	53.5	18.2	0.25
126.8	50.5	22.5	0.31
127.1	48.9	18.4	0.27
127.4	52.3	17.4	0.25
127.7	52.4	16.2	0.24
127.9	56.2	14.9	0.21
128.2	55.0	17.5	0.24
128.5	50.9	14.8	0.22
128.8	49.5	18.0	0.27
129.1	47.9	15.1	0.24
130.5	56.5	13.8	0.20

References

Abelmann, A. & Gersonde, R. Biosiliceous particle flux in the Southern Ocean. *Mar. Chem.* **35**, 503–536 (1991).

Abelmann, A. Radiolarian flux in Antarctic waters (Drake Passage, Powell Basin, Bransfield Strait), *Polar Biol.***12,** 357–372 (1992).

Abelmann, A. & Gowing, M. M. Spatial distribution pattern of living polycystine radiolarian taxa—baseline study for paleoenvironmental reconstructions in the Southern Ocean (Atlantic sector), *Mar. Micropaleontol*. **30**, 3–28 (1997).

Abelmann, A., Brathauer, U., Gersonde, R., Sieger, R. & Zielinski, U. Radiolarian-based transfer function for the estimation of sea surface temperatures in the Southern Ocean (Atlantic Sector). *Paleoceanography* **14**, 410–421(1999).

Bamber, J. L., Riva, R. E. M., Vermeersen, B. L. A. & Lebrocq, A. M. Reassessment of the potential sea-level rise from a collapse of the West Antarctic Ice Sheet. *Science* **324,** 901–903 (2009).

Barlow, N. L. M. et al. Lack of evidence for a substantial sea-level fluctuation within the Last Interglacial. *Nat. Geosci.* **11,** 627–634 (2018).

Bayon, G. et al. An improved method for extracting marine sediment fractions and its application to Sr and Nd isotopic analysis. *Chem. Geol*. **187,** 179–199 (2002).

Bazin, L. et al. An optimized multi-proxy, multi-site Antarctic ice and gas orbital chronology (AICC2012): 120-800 ka. *Climate of the Past* **9,** 1715–1731 (2013).

Behrens, B., Miyairi, Y., Sproson, A. D., Yamane, M. & Yokoyama, Y. Meltwater discharge during the Holocene from the Wilkes subglacial basin revealed by beryllium isotope analysis of marine sediments. *J. Quat. Sci.* **34,** 603–608 (2019).

Bjørklund, K. R. Radiolaria from the Norwegian Sea, Leg 38 of the Deep Sea Drilling Project. *Initial reports of the deep sea drilling project* **38**, 1101–1168 (1976).

Blackburn, T. et al. Ice retreat in Wilkes Basin of East Antarctica during a warm interglacial. *Nature* **583,** 554–559 (2020).

Blanchon, P., Eisenhauer, A., Fietzke, J. & Liebetrau, V. Rapid sea-level rise and reef back-stepping at the close of the last interglacial highstand. *Nature* **458,** 881–884 (2009).

Boltovskoy, D. & Riedel, W. R. Polycystine Radiolaria from the southwestern Atlantic Ocean plankton. *Rev. Esp. Micropaleontol*. **12**, 99–146 (1980).

Boltovskoy, D. Vertical distribution patterns of Radiolaria Polycystina (Protista) in the World Ocean: living ranges, isothermal submersion and settling shells. *J. Plankton Res.* **39**, 330–349, (2017).

Bourlès, D. L., Raisbeck, G. M. & Yiou, F. ^{10}Be and ^{9}Be in marine sediments and their potential for dating. *Geochim. Cosmochim. Acta* **53,** 443–452 (1989).Capron, E. et al. Temporal and spatial structure of multi-millennial temperature changes at high latitudes during the Last Interglacial. *Quat. Sci. Rev.* **103,** 116–133 (2014).

Brathauer, U., Abelmann, A., Gersonde, R., Niebler, H. S. & Fütterer, D. K. Calibration of *Cycladophora davisiana* events versus oxygen isotope stratigraphy in the subantarctic Atlantic Ocean—A stratigraphic tool for carbonate-poor Quaternary sediments. *Mar. Geol.* **175,** 167–181 (2001).

Chadwick, M., Allen, C. S., Sime, L. C., Crosta, X. & Hillenbrand, C.D. How does the Southern Ocean palaeoenvironment during Marine Isotope Stage 5e compare to the modern? *Mar. Micropaleontol.* **170,** 102066 (2022).

Close, D. I., Stagg, H. M. J. & O'Brien, P. E. Seismic stratigraphy and sediment distribution on the Wilkes Land and Terre Adélie margins, East Antarctica. *Mar. Geol.* **239** 33–57, (2007).

Colville, E. J. et al. Sr-Nd-Pb isotope evidence for ice-sheet presence on Southern Greenland during the Last Interglacial. *Science* **333,** 620–623 (2011).

Cook, C. P. et al. Dynamic behavior of the East Antarctic ice sheet during Pliocene warmth. *Nat. Geosci*. **6,** 765–769 (2013).

Cortese, G. & Abelmann, A. Radiolarian-based paleotemperatures during the last 160 kyr at ODP Site 1089 (Southern Ocean, Atlantic Sector). *Palaeogeogr. Palaeoclimatol. Palaeoecol.* **182**, 259–286 (2002).

Cortese, G. & Prebble, J. A radiolarian-based modern analogue dataset for palaeoenvironmental reconstructions in the southwest Pacific, *Mar. Micropaleontol*. **118**, 34–49, (2015).

Chmeleff, J., von Blanckenburg, F., Kossert, K. & Jakob, D. Determination of the ^{10}Be half-life by multicollector ICP-MS and liquid scintillation counting. *Nucl. Instrum. Methods Phys. Res. B: Beam Interact. Mater. At.* **268,** 192–199 (2010).

Crotti, I. et al. Wilkes subglacial basin ice sheet response to Southern Ocean warming during late Pleistocene interglacials. *Nat. Commun*. **13,** 1–11 (2022).

Crosta, X., Sturm, A., Armand, L. & Pichon, J. J. Late Quaternary sea ice history in the Indian sector of the Southern Ocean as recorded by diatom assemblages. *Mar. Micropaleontol.* **50**, 209–223 (2004).

Crosta, X., Shukla, S. K., Ther, O., Ikehara, M., Yamane, M. & Yokoyama, Y. Last Abundant Appearance Datum of Hemidiscus karstenii driven by climate change. *Mar. Micropaleontol.* **157**, 101861 (2020).

DeConto, R. M. & Pollard, D. Contribution of Antarctica to past and future sea-level rise. *Nature* **531,** 591–597 (2016).

Donda, F., Brancolini, G., De Santis, L. & Trincardi, F. Seismic facies and sedimentary processes on the continental rise off Wilkes Land (East Antarctica): evidence of bottom current activity. *Deep Sea Res. Part II Top. Stud. Oceanogr*. **50,** 1509–1527 (2003).

Dutkiewicz, A., Müller, R. D., O'Callaghan, S. & Jónasson, H. Census of seafloor sediments in the world's ocean. *Geology*, **43**, 795–798 (2015).

Dutton, A. et al. Sea-level rise due to polar ice-sheet mass loss during past warm periods. *Science* **349,** aaa4019 (2015).

Dutton, A., Webster, J. M., Zwartz, D., Lambeck, K. & Wohlfarth, B. Tropical tales of polar ice: evidence of Last Interglacial polar ice-sheet retreat recorded by fossil reefs of the granitic Seychelles islands. *Quat. Sci. Rev.* **107,** 182–196 (2015).

Dow, R. L. Radiolarian distribution and the late Pleistocene history of the southeastern Indian Ocean. *Mar. Micropaleontol*., **3**, 203–227 (1978).

Elderfield, H. et al. A record of bottom water temperature and seawater $\delta^{18}O$ for the Southern Ocean over the past 440 kyr based on Mg/Ca of benthic foraminiferal Uvigerina spp. *Quat. Sci. Rev.* **29,** 160–169 (2010).

Escutia, C., Brinkhuis, H., Klaus, A. & the Expedition 318 Scientists Proc. IODP, 318 (Integrated Ocean Drilling Program Management International, Inc., Tokyo, 2011).Fretwell, P. et al. Bedmap2: improved ice bed, surface and thickness datasets for Antarctica. *Cryosphere* **7,** 375–393 (2013).

Ferraccioli, F., Armadillo, E., Jordan, T., Bozzo, E. & Corr, H. Aeromagnetic exploration over the East Antarctic Ice Sheet: A new view of the Wilkes Subglacial Basin. *Tectonophysics* **478,** 62–77 (2009).

Frezzotti, M. et al. Geophysical survey at Talos Dome, East Antarctica: The search for a new deep-drilling site. *Ann. Glaciol.* **39,** 423–432 (2004).

Fogwill, C. J. et al. Testing the sensitivity of the East Antarctic Ice Sheet to Southern Ocean dynamics: past changes and future implications. *J. Quat. Sci.* **29,** 91–98 (2014).

Fogwill, C. J. et al. Antarctic ice sheet discharge driven by atmosphere-ocean feedbacks at the Last Glacial Termination. *Sci. Rep.* **7,** 1–10 (2017).

Galaasen, E. V., Ninnemann, U. S., Irvalı, N., Kleiven, H. K. F., Rosenthal, Y., Kissel, C., & Hodell, D. A. Rapid reductions in North Atlantic Deep Water during the peak of the last interglacial period. *Science* **343**, 1129–1132 (2014).

Golledge, N. R., Levy, R. H., McKay, R. M. & Naish, T. R. East Antarctic ice sheet most vulnerable to Weddell Sea warming. *Geophys. Res. Lett.* **44,** 2343–2351 (2017).

Golledge, N. R. et al. Retreat of the Antarctic Ice Sheet during the Last Interglaciation and implications for future change. *Geophys. Res. Lett.* **48,** e2021GL094513 (2021).

Goursaud, S. et al. Antarctic Ice Sheet elevation impacts on water isotope records during the Last Interglacial. *Geophys. Res. Lett.* **48,** e2020GL091412 (2020).

Greene, C. A., Blankenship, D. D., Gwyther, D. E., Silvano, A. & van Wijk, E., Wind causes Totten Ice Shelf melt and acceleration. *Sci. Adv*. **3**, e1701681 (2017).

Guo, G., Shi, J., Gao, L., Tamura, T. & Williams, G. D. Reduced sea ice production due to upwelled oceanic heat flux in Prydz Bay, East Antarctica. *Geophys. Res. Lett*. **46**, 4782–4789, (2019).

Hammer, O., Harper, D. & Ryan P. D. PAST: Paleontological Statistic Software Package for Education and Data Analyses, *Paleontol. Electron.* 4–9 (2001).

Hay, C. et al. The sea-level fingerprints of ice-sheet collapse during interglacial periods. *Quat. Sci*. *Rev*. **87,** 60–69 (2014).

Hayes, C. T. et al. A stagnation event in the deep South Atlantic during the last interglacial period. *Science* **346,** 1514–1517 (2014).

Hays, J.D. Radiolaria and late Tertiary and Quaternary history of Antarctic seas. In: Llano, G.A. (ed.) Biology of the Antarctic Seas II. *Antarct. Res. Ser., b*, 125–184 (1965).

Hays, J. D., Lozano, J. A., Shackleton, N. & Irving, G. Reconstruction of the Atlantic and western Indian Ocean sectors of the 18,000 B.P. Antarctic Ocean. *Geological Society of America Memoir* **145,** 337–372 (1976).

Holloway, M. D. et al. The spatial structure of the 128 ka Antarctic sea ice minimum. *Geophys. Res. Lett.* **44,** 11–129 (2017).

Herraiz-Borreguero, L., Coleman, R., Allison, I., Rintoul, S. R., Craven, M., and Williams, G. D. Circulation of modified Circumpolar Deep Water and basal melt beneath the Amery Ice Shelf, East Antarctica. J. *Geophys. Res.*: Oceans, **120**, 3098–3112, (2015).

Herraiz-Borreguero, L. & Naveira Garabato, A. C. Poleward shift of Circumpolar Deep Water threatens the East Antarctic Ice Sheet. *Nat. Clim. Chang.* **12**, 728–734 (2022).

Howard, W. R. & Prell, W. L. Late Quaternary surface circulation of the Southern Indian Ocean and its relationship to orbital variations. *Paleoceanography* **7,** 79–117 (1992).

Hirano, D., Tamura, T., Kusahara, K., Ohshima, K. I., Nicholls, K. W., Ushio, S., Simizu. D., Ono. K., Fujii. M., Nogi, Y. & Aoki, S. Strong ice-ocean interaction beneath Shirase Glacier Tongue in East Antarctica. *Nat. Commun*. **11**, 1–12 (2020).

Hülsemann, K. Radiolaria in plankton from the Arctic Drifting Station T-3, including the description of three new species. *Arctic Institute of North America, Technical Paper* **13**, 1–52 (1963).

Ikenoue, T., Takahashi, K. & Tanaka, S. Fifteen year time- series of radiolarian fluxes and environmental conditions in the Bering Sea and the central subarctic Pacific, 1990–2005. *Deep-Sea Res*. 61–64,17–49 (2012).

Imbrie, J. A new micropaleontological method for quantitative paleoclimatology: application to a late Pleistocene Caribbean core. *The late Cenozoic glacial ages* 71–181 (1971).

Imbrie, J., van Donk, J. & Kipp, N. G. Paleoclimatic Investigation of a Late Pleistocene Caribbean Deep-Sea Core: Comparison of Isotopic and Faunal Methods1. *Quat. Res*. **3**, 10–38 (1973).

Itaki, T. Depth-related radiolarian assemblage in the water-column and surface sediments of the Japan Sea. *Mar. Micropaleontol.*, **47**, 253–270 (2003).

Itaki, T. Elutriation technique for extracting radiolarian skeletons from sandy sediments and its usefulness for faunal analysis. *Radiolaria* **24,** 14–18 (2006).

Itaki, T., Minoshima, K. & Kawahata, H. Radiolarian flux at an IMAGES site at the western margin of the subarctic Pacific and its seasonal relationship to the Oyashio Cold and Tsugaru Warm currents. *Mar. Geol.* **255**, 131–148 (2008).

Itaki, T., Kimoto, K. & Hasegawa, S. Polycystine radiolarians in the Tsushima Strait in autumn of 2006. *Paleontol. Res.* **14**, 19–32 (2010).

Itaki, T. Size and morphological variations of the radiolarian Larcopyle buetschlii Dreyer in the Japan Sea and its depth distribution in the water column. *News of Osaka Micropaleontologists*, *Spec*. **16**, 41–59 (2016).

Itaki, T., Sagawa, T. & Kubota, Y. Data report: Pleistocene radiolarian biostratigraphy, IODP Expedition 346 Site U1427. In Tada, R., Murray, R.W., Alvarez Zarikian, C.A., and the Expedition 346 Scientists, Proceedings of the Integrated Ocean Drilling Program, 346: College Station, TX (Integrated Ocean Drilling Program) (2018).

Jenkins, A., Shoosmith, D., Dutrieux, P., Jacobs, S., Kim, T. W., Lee, S. H. & Stammerjohn, S. West Antarctic Ice Sheet retreat in the Amundsen Sea driven by decadal oceanic variability. Nat. Geosci. 11, 733–738 (2018).

Jimenez-Espejo, F. J., et al. Late Pleistocene oceanographic and depositional variations along the Wilkes Land margin (East Antarctica) reconstructed with geochemical proxies in deep-sea sediments. *Glob. Planet Change* **184,** 103045 (2020).

Jørgensen, E. Protistenplankton aus dem Nordmeere in den Jahren 1897–1900. *Bergens Museums Aarbog*, 1899 **6**, 45–98 (1900).

Jørgensen, E. The protist plankton and the diatoms in bottom samples. In: Nordgaard, O. (Ed.), Hydrographical and biological investigations in Norwegian fiords. *Bergen Museum Skrifter* **1**, 59–151 (1905).

Jouzel, J., Delaygue, G., Landais, A., Masson-Delmotte, V., Risi, C. & Vimeux, F. Water isotopes as tools to document oceanic sources of precipitation. *Water Resources Research*, **49**, 7469–7486 (2013).

Kling, S. A. Vertical distribution of polycystine radiolarians in the central North Pacific, *Mar. Micropaleontol.* **4**, 295–318 (1979).

Kling, S. A. & Boltovskoy, D. Radiolarian vertical distribution patterns across the southern California Current. Deep Sea Research Part I: *Oceanogr. Res. Pap.* **42**, 191–231 (1995).

Kopp, R. E., Simons, F. J., Mitrovica, J. X., Maloof, A. C. & Oppenheimer, M. Probabilistic assessment of sea level during the last interglacial stage. *Nature* **462,** 863–867 (2009).

Korschinek, G. et al. A new value for the half-life of ^{10}Be by Heavy-Ion Elastic Recoil Detection and liquid scintillation counting. *Nucl. Instrum. Methods Phys. Res. B: Beam Interact. Mater. At.* **268,** 187–191 (2010).

Lawler, K. A., et al. The Southern Ocean Radiolarian (SO-RAD) dataset: a new compilation of modern radiolarian census data. *Earth System Science Data* **13**, 5441–5453 (2021).

Li, Q., Marshall, J., Rye, C. D., Romanou, A., Rind, D. & Kelley, M. Global Climate Impacts of Greenland and Antarctic Meltwater: A Comparative Study. *Journal of Climate* **36**, 3571–3590 (2023).

Licht, K. J. & Hemming, S. R. Analysis of Antarctic glacigenic sediment provenance through geochemical and petrologic applications. *Quat. Sci. Rev.* **164,** 1–24 (2017).

Martinson, D. G., Pisias, N. G., Hays, J. D., Imbrie, J., Moore, T. C. & Shackleton, N. J. Age Dating and the Orbital Theory of the Ice Ages: Development of a High-Resolution 0 to 300,000-Year Chronostratigraphy1. *Quat. Res*. **27,** 1–29 (1987).

Marshall, J., and Speer, K. Closure of the meridional overturning circulation through Southern Ocean upwelling. *Nat. Geosci*. **5**, 171–180 (2012).

Masson-Delmotte, V. et al. A comparison of the present and last interglacial periods in six Antarctic ice cores. *Climate of the Past* **7,** 397–423 (2011).

Matsuoka, K. et al. Quantarctica, an integrated mapping environment for Antarctica, the Southern Ocean, and sub-Antarctic islands. *Environ. Model. Softw.* **140**, 105015 (2021).

Matsuzaki, H. et al. Current status and future direction of MALT, the University of Tokyo. *Nucl. Instrum. Methods Phys. Res. B: Beam Interact. Mater. At*. **223,** 92–99 (2004).

Matsuzaki, H., Ohkura, M. A., Ishige, Y., Nogami, Y. & Okamoto, H. Photoinduced switching to metallic states in the two-dimensional organic Mott insulator dimethylphenazine-

tetrafluorotetracyanoquinodimethane with anisotropic molecular stacks. *P Phys. Rev. B Condens. Matter* **91,** 1–10 (2015).

Matsuzaki, K. M., Itaki, T. & Kimoto, K., Vertical distribution of polycystine radiolarians in the northern East China Sea, *Mar. Micropaleontol.* **125**, 66–84 (2016).

Mengel, M. & Levermann, A. Ice plug prevents irreversible discharge from East Antarctica. *Nat. Clim. Change* **4,** 451–455 (2014).

Mercer, J. H., West Antarctic ice sheet and CO2 greenhouse effect: a threat of disaster. *Nature* **271**, 321–325 (1978).

McCave, I. N. & Hall, I. R. Size sorting in marine muds: Processes, pitfalls, and prospects for paleoflow-speed proxies. *Geochem. Geophys. Geosyst*. **7,** Q10N05 (2006).

McKay, N. P., Overpeck, J. T. & Otto-Bliesner, B. L. The role of ocean thermal expansion in Last Interglacial sea level rise. *Geophys. Res. Lett.* **38,** 4–9 (2011).

McCave, I. N. & Hall, I. R. Size sorting in marine muds: Processes, pitfalls, and prospects for paleoflow-speed proxies. *Geochem. Geophys. Geosyst*. **7,** Q10N05 (2006).

Morley, J. J., and Stepien, J. C. Antarctic Radiolaria in late winter/early spring Weddell Sea waters. *Micropaleontology* 365–371 (1985).

NEEM community members Eemian interglacial reconstructed from a Greenland folded ice core. *Nature* **493,** 489–494 (2013).

Nishimura, A., Nakaseko, K. & Yoshihisa O. A new coastal water radiolarian assemblage recovered from sediment samples from the Antarctic Ocean. *Mar. Micropaleontol*. **30**, 29–44 (1997).

Nishimura, A., and Nakaseko, K. Characterization of radiolarian assemblages in the surface sediments of the Antarctic Ocean. *Palaeoworld* **20**, 232–251 (2011).

Nishiizumi, K., Imamura, M., Caffee, M. W., Southon, J. R., Finkel, R. C. & McAninch, J. Absolute calibration of ^{10}Be AMS standards. *Nucl. Instrum. Methods Phys. Res. B: Beam Interact. Mater*. **258,** 403–413 (2007).

Okazaki, Y., Takahashi, K., Itaki, T. & Kawasaki, Y. Comparison of radiolarian vertical distributions in the Okhotsk Sea near the Kuril Islands and in the northwestern North Pacific off Hokkaido Island. *Mar. Micropaleontol.* **51**, 257–284, (2004).

O'Leary, M. J. et al. Ice sheet collapse following a prolonged period of stable sea level during the last interglacial. *Nat. Geosci.* **6,** 796–800 (2013).

Orsi, A. H., and Wiederwohl, C. L., A recount of Ross Sea waters. Deep Sea Research Part II: *Topical Studies in Oceanography* **56**, 778–795 (2009).

Petrushevskaya, M.G. Radiolarians of orders Spumellaria and Nassellaria of the Antarctic region. In: Andriyashev, A.P., Ushakov, P.V. (Eds.), Studies of Marine Fauna IV (XII): Biological Reports of the Soviet Antarctic Expedition (1955–1958) 3, Academy of Sciences of the USSR, Leningrad, 2–186 (1967).

Petrushevskaya, M. G. Distribution of radiolarian skeletons in the sediments of the North Atlantic. Fossil and recent radiolarians (0. S. Vyalov ed.), *Univ. Press, Lvov*, 123–132 (1969).

Petrushevskaya, M. G. Radiolaria in the plankton and recent sediments from the Indian Ocean and Antarctic. *The Micropalaeontology of Oceans.* 319–329 (1971).

Polyak, V. J. et al. A highly resolved record of relative sea level in the western Mediterranean Sea during the last interglacial period. *Nat. Geosci*. **11,** 860–864 (2018).

Presti, M. et al. Sediment delivery and depositional patterns off Adelie Land (East Antarctica) in relation to late Quaternary climatic cycles. *Mar. Geol*. **284,** 96–113 (2011).

Pierce, E. L. et al. Evidence for a dynamic East Antarctic ice sheet during the mid-Miocene climate transition. *Earth Planet. Sci. Lett.* **478,** 1–13 (2017).

Pritchard, H. D. et al. Antarctic ice-sheet loss driven by basal melting of ice shelves. *Nature* **484,** 502–505 (2012).

Renz, G. W. The distribution and ecology of Radiolaria in the central Pacific: plankton and surface sediments. *Bull. Scripps Inst. Oceanogr.* **22**, 267 (1976).

Rohling, E. J. et al. Asynchronous Antarctic and Greenland ice-volume contributions to the last interglacial sea-level highstand. *Nat. Commun.* **10,** 1–9 (2019).

Roy, M., van de Flierdt, T., Hemming, S. R. & Goldstein, S. L. $^{40}Ar/^{39}Ar$ ages of hornblende grains and bulk Sm/Nd isotopes of circum-Antarctic glacio-marine sediments: Implications for sediment provenance in the southern ocean. *Chem. Geol.* **244,** 507–519 (2007).

Ross, N. et al. Steep reverse bed slope at the grounding line of the Weddell Sea sector in West Antarctica. *Nat. Geosci*. **5,** 393–396 (2012).

Rignot, E., Jacobs, S., Mouginot, J. & Scheuchl, B. Ice-shelf melting around Antarctica. *Science* **341**, 266–270 (2013).

Rignot, E. et al. Four decades of Antarctic Ice Sheet mass balance from 1979–2017. *Proc. Natl. Acad. Sci. U.S.A.* **116,** 1095–1103 (2019).

Rintoul, S. R., Silvano, A., Pena-Molino, B., van Wijk, E., Rosenberg, M., Greenbaum, J. S. & Blankenship, D. D. Ocean heat drives rapid basal melt of the Totten Ice Shelf. *Sci. Ad.* **2**, e1601610 (2016).

Sakamoto, T., Kuroki K., Sugawara T., Aoike, K., Iijima, K. & Sugisaki, S. Non-destructive X-ray fluorescence (XRF) core-imaging scanner, TATSCAN-F2. *Sci Drill* **2,** 37–39 (2006).

Shackleton, S. et al. Global ocean heat content in the Last Interglacial. *Nat. Geosci.* **13,** 77–81 (2020).

Schneider-Mor, A., Yam, R., Bianchi, C., Kunz-Pirrung, M., Gersonde, R. & Shemesh, A. Nutrient regime at the siliceous belt of the Atlantic sector of the Southern Ocean during the past 660 ka. *Paleoceanography* **23,** PA3217 (2008).

Silvano. A., Rintoul. S. R., Peña-Molino. B., Hobbs. W. R., van Wijk, E., Aoki. S., Tamura. T. & Williams G. D. Freshening by glacial meltwater enhances melting of ice shelves and reduces formation of Antarctic Bottom Water. *Sci. adv.* **4**, eaap9467 (2018).

Simon, Q. et al. Authigenic $^{10}Be/^{9}Be$ ratios and ^{10}Be-fluxes ($^{230Th}_{xs}$-normalized) in central Baffin Bay sediments during the last glacial cycle: Paleoenvironmental implications. *Quat. Sci Rev*. **140,** 142–162 (2016).

Sun, S. et al. Antarctic ice sheet response to sudden and sustained ice-shelf collapse (ABUMIP). *Journal of Glaciology* **66,** 891–904 (2020).

Sutter, J. et al. Modelling the Antarctic Ice Sheet across the mid-Pleistocene transition – Implications for Oldest Ice. *Cryosphere* **13,** 2023–2041 (2019).

Sutter, J. et al. Limited retreat of the Wilkes Basin ice sheet during the Last Interglacial. *Geophys. Res. Lett.* **47,** e2020GL088131 (2020).

Swanberg, N. R. & Eide, L. K., The radiolarian fauna at the ice edge in the Greenland Sea during summer, 1988. *Journal of marine research* **50**, 297–320 (1992).

Swingedouw, D., Fichefet, T., Goosse, H. & Loutre, M. F. Impact of transient freshwater releases in the Southern Ocean on the AMOC and climate. *Climate dynamics* **33**, 365–381 (2009).

Tamura, T., Ohshima, K. I. & Nihashi, S. Mapping of sea ice production for Antarctic coastal polynyas. *Geophys. Res. Lett.* **35** (2008).

Tanaka, T. et al. Jndi-1: A neodymium isotopic reference in consistency with LaJolla neodymium. *Chem. Geol*. **168,** 279–281 (2000).

Thompson, W. G., Curran, A. H., Wilson, M. A. & White, B. Sea-level oscillations during the last interglacial highstand recorded by Bahamas corals. *Nat. Geosci.* **4,** 684–687 (2011).

Tibbs, J. F. On some planktonic Protozoa taken from the track of drift station ARLIS I, 1960-61. *Arctic* 247–254 (1967).

Turney, C. S. M. et al. Early Last Interglacial ocean warming drove substantial ice mass loss from Antarctica. *Proc. Natl Acad. Sci. USA* **117,** 3996–4006 (2020).

Uemura, R. et al. Ranges of moisture-source temperature estimated from Antarctic ice cores stable isotope records over glacial-interglacial cycles. *Climate of the Past* **8,** 1109–1125 (2012).

Valletta, R. D., Willenbring, J. K., Passchier, S. & Elmi, C. $^{10}Be/^{9}Be$ ratios reflect Antarctic Ice Sheet freshwater discharge during Pliocene warming. *Paleoceanogr. Paleoclimatol.* **33,** 934–944 (2018).

Veres, D. et al. The Antarctic ice core chronology (AICC2012): An optimized multi-parameter and multi-site dating approach for the last 120 thousand years. *Climate of the Past* **9,** 1733–1748 (2013).

Weber, M. E., Golledge, N. R., Fogwill, C. J., Turney, C. S. M. & Thomas, Z. A. Decadal-scale onset and termination of Antarctic ice-mass loss during the last deglaciation. *Nat.Commun.* **12,** 1–13 (2021).

Werner, M., Jouzel, J., Masson-Delmotte, V. & Lohmann, G. Reconciling glacial Antarctic water stable isotopes with ice sheet topography and the isotopic paleothermometer. *Nat. Commun.* **9,** 1–10 (2018).

Weis, D. et al. High-precision isotopic characterization of USGS reference materials by TIMS and MC-ICP-MS. *Geochem. Geophys. Geosyst*. **7,** (2006).

White, D. A. et al. Beryllium isotope signatures of ice shelves and sub-ice shelf circulation. *Earth Planet. Sci. Lett.* **505,** 86–95 (2019).

Willenbring, J. K. & von Blanckenburg, F. Meteoric cosmogenic Beryllium-10 adsorbed to river sediment and soil: Applications for Earth-surface dynamics. Earth *Sci. Rev*. **98,** 105–122 (2010).

Wilson, D. J. et al. Ice loss from the East Antarctic Ice Sheet during late Pleistocene interglacials. *Nature* **561,** 383–386 (2018).

Wu, L. et al. Productivity-climate coupling recorded in Pleistocene sediments off Prydz Bay (East Antarctica). *Palaeogeogr. Palaeoclimatol. Palaeoecol*. **485,** 260–270 (2017).

Wu, L. et al. Late Quaternary deep stratification-climate coupling in the Southern Ocean: Implications for changes in abyssal carbon storage. *Geochem. Geophys. Geosyst.* **19,** 379–395 (2018).

Yamazaki, K., Aoki, S., Katsumata, K., Hirano, D. & Nakayama, Y. Multidecadal poleward shift of the southern boundary of the Antarctic Circumpolar Current off East Antarctica. *Sci. ad*. **7**, eabf8755 (2021).

Yokoyama, Y. et al. Widespread collapse of the Ross Ice Shelf during the late Holocene. *Proc. Natl. Acad. Sci.* **113,** 2354–2359 (2016).

Acknowledgments

I would like to express my heartfelt appreciation to my supervisor, Dr. Osamu Seki, for his meticulous guidance, unwavering encouragement, and invaluable discussions that have significantly contributed to the success of my research and have made my academic journey unforgettable.

I extend my sincere thanks to Dr. Masanobu Yamamoto, Tomohisa Irino, Jun Nishioka, and Yusuke Okazaki for their valuable reviews and insightful comments.

I am also indebted to Dr. Takuya Itaki, Tina van de Fleirdt, Wilson J. David, Yusuke Suganuma, Keiji Horikawa, and Minoru Ikehara for their assistance in data collection and analysis. Their support, shared ideas, and stimulating discussions have played a pivotal role in shaping my understanding of the subject matter and have inspired me to pursue excellence.

To all the individuals mentioned above and to everyone else who has supported me in various capacities throughout the development of this thesis, I offer my heartfelt gratitude. Your contributions have been pivotal to my academic growth and the successful completion of this endeavor.

Lastly, I would like to express profound appreciation to my family and friends for their unwavering support, understanding, and motivation throughout my academic pursuit. Their love, faith in my abilities, and constant encouragement have been my enduring source of strength."